Applications of Quasi-Geostrophic Analysis Methods to Investigation of a Case of Rapid Cyclogenesis

---

by

Patrick T. Beaty

A thesis submitted in partial fulfillment of
the requirements for the degree of

Master of Science
Department of Atmospheric and Oceanic Sciences

at the
University of Wisconsin – Madison
2021

ABSTRACT

Quasi-geostrophic (QG) diagnostic techniques are employed in the analysis of a case of rapid cyclogenesis over the northeast Pacific Ocean which occurred in late November 2019. The exceptional nature of this storm in regard to its storm track, deepening rate, and location of maximum deepening is examined, along with comparing and contrasting the November 2019 storm to the strongest extratropical cyclone to ever occur. Considering lower troposphere height perturbations from the inversion of quasi-geostrophic potential vorticity (QGPV), a comprehensive picture of the development of the storm is constructed. The results suggest that the middle and especially the lower levels of the atmosphere accounted for more than 95% of the total development of this storm, which stands in apparent contradiction to expectations for a Type B cyclogenesis event as described by Petterssen and Smebye (1971). Utilizing results from a QG-omega inversion, the integrated QG mass divergence is considered using the same vertical column partitioning as in the QGPV inversion to analyze cyclogenesis from a comparable perspective. In this analysis, the vertical partitioning of QG forcing for ascent is related to near-surface pressure tendencies throughout the progression of the November 2019 storm. This analysis also concludes that forcings within the lower levels of the atmosphere completely dominated surface cyclogenesis, with the middle- and upper-levels having meager contributions. It is proven that this single storm exhibits elements of all three types of cyclogenesis (Type A, B, and C) as described in both Petterssen and Smebye (1971) and Plant et al. (2003), while being entirely driven by forcings in the lowest 150 hPa.

Thesis Declaration and Approval

I, Patrick T. Beaty, declare that this thesis entitled “Applications of Quasi-Geostrophic Analysis Methods to Investigation of a Case of Rapid Cyclogenesis” and the work presented in it are my own.

Patrick T. Beaty ________ ________________ ________
Author **Signature** **Date**

I hereby approve and recommend for acceptance this work in partial fulfillment of the requirements for the degree of Master of Science:

Jonathan E. Martin ________ ________________ ________
Committee Chair **Signature** **Date**

Michael C. Morgan ________ ________________ ________
Faculty Member **Signature** **Date**

Stephanie A. Henderson ________ ________________ ________
Committee Member **Signature** **Date**

ACKNOWLEDGEMENTS

To my wife, Jessica: I would not have dreamt of completing a master's degree at UW-Madison without you in my life (literally, I used to despise all things UW when I first moved here from Nebraska). Thank you for all of the campus tours, Wisconsin trivia, helping me with sports chants, telling me about the AOS program and showing me the best places to eat in between classes. And thank you for sticking by my side while I attempted to progress through a graduate degree in such a demanding field from such a prestigious university. I know it has not been easy and your patience and nodding along as I complain about having to derive equations and fix code which make no sense to you is much appreciated!

To Jon Martin, Michael Morgan, and Steph Henderson: You have all been invaluable in enhancing my graduate school experience. Whether we are holding professional conversations about a given topic in meteorology or we are casually discussing favorite restaurants or hobbies, I have thoroughly enjoyed every chance I have had to talk to you all. To Jon, especially, thank you for this opportunity. I could not have imagined a better research position than my current one with you as my advisor. I am looking forward to continuing to grow as a scientist under all of your unrivaled guidance!

To my dad, John, mom, Mary, and sister, Liz: Your continued love and support throughout my entire life and especially during my master's program is the reason I am able to do incredible things like completing a master's degree. A college degree, let alone a master's degree, is something I am very privileged to have and am proud of and either would not have been possible without you all. Thank you for providing such a loving environment for me to flourish and chase my dreams!

To everyone not listed by name: The list of crucial people in helping me through my master's degree would take 15 pages to single everyone out. So, if you are a past professor of mine, a friend I met in graduate school (Jerrold, Meri, Colleen, Angelica, Nuo, Andi, Jongjin, Maria, Kate, Ian, Poush), a friend I met in my undergraduate program, anyone in the AOS building who says hi, anyone who has helped me with all of my incessant questions (Pete, Dee, Sue, Christi), any of my wonderful friends and family, or any other person who I owe a portion of my success to, thank you from the bottom of my heart.

Praise to thee our Alma Mater. U-rah-rah, Wisconsin!

TABLE OF CONTENTS

i. List of Figures and Tables

Figure 2.1. (a.) Sea-level pressure and 950 hPa equivalent potential temperature from the GFS analysis valid at 1200 UTC 25 November 2019. Solid, black lines are isobars contoured every 4 hPa starting at 1000 hPa with the leading “9” or “10” omitted. Dashed, green lines are 950 hPa moist isentropes contoured every 5 Kelvin. “H” denotes areas of localized high pressure whereas “L” denotes areas of localized low pressure. Cold and warm fronts are also analyzed. (b.) Potential temperature and positive frontogenesis at 850 hPa from the GFS analysis valid at 1200 UTC 25 November 2019. Dashed, red contours are isentropes contoured every 3 Kelvin. Shading indicates positive frontogenesis function values shaded every $9.26\ x\ 10^{-10}$ K m^{-1} s^{-1}, or every $\frac{1\,K}{100\,km}\,\frac{1}{3\,hr}$. c.) Geopotential heights, potential temperature, and vorticity at 500 hPa from the GFS analysis valid at 1200 UTC 25 November 2019. Solid, black contours are geopotential heights contoured every 6 dm starting at 540 dm. Red, dashed contours are isentropes contoured every 3 Kelvin starting at 290 Kelvin. Shading indicates positive relative vorticity shaded every $4\ x\ 10^{-5}$ s^{-1} starting at $16\ x\ 10^{-5}$ s^{-1}. d.) Geopotential heights and wind speed at 300 hPa from the GFS analysis valid at 1200 UTC 25 November 2019. Solid, black contours are geopotential heights contoured every 12 dm starting at 1020 dm. Shading indicates wind speed shaded every 10 m s^{-1} starting at 30 m s^{-1}.

Figure 2.2. (a.) As for Fig. 2.1a except GFS analysis valid at 0000 UTC 26 November 2019. (b.) As for Fig. 2.1b except GFS analysis valid at 0000 UTC 26 November 2019. (c.) As for Fig. 2.1c except GFS analysis valid at 0000 UTC 26 November 2019. (d.) As for Fig. 2.1d except GFS analysis valid at 0000 UTC 26 November 2019.

Figure 2.3. (a.) As for Fig. 2.2a except GFS analysis valid at 1200 UTC 26 November 2019. (b.) As for Fig. 2.2b except GFS analysis valid at 1200 UTC 26 November 2019. (c.) As for Fig. 2.2c except GFS

hour forecast valid 0600 UTC 26 November 2019 of EPV at 500 hPa. Gray contours are EPV in potential vorticity units (PVU) contoured every 0.5 PVU. Black "L" denotes location of 1000-hPa central sea-level pressure minimum and EPV at the location of the 1000-hPa central sea-level pressure minimum is plotted in PVU. (b.) 18-hour forecast valid 0600 UTC 26 November 2019 of quasi-geostrophic potential vorticity (QGPV) at 500 hPa, scaled by $-g\frac{\partial\theta}{\partial p}\ x\ 10^6$ to convert from units of s^{-1} to units of PVU, as in Hakim et al. (1996). Gray contours are QGPV in PVU contoured every 0.5 PVU. Black "L" denotes location of 1000-hPa central sea-level pressure minimum and QGPV at the location of the 1000-hPa central sea-level pressure minimum is plotted in PVU. (c.) 30-hour forecast valid 1800 UTC 26 November 2019 of EPV at 500 hPa. Gray contours are EPV in potential vorticity units (PVU) contoured every 0.5 PVU. Black "L" denotes location of 1000-hPa central sea-level pressure minimum and EPV at the location of the 1000-hPa central sea-level pressure minimum is plotted in PVU. (d.) 30-hour forecast valid 1800 UTC 26 November 2019 of quasi-geostrophic potential vorticity (QGPV) at 500 hPa, scaled by $-g\frac{\partial\theta}{\partial p}\ x\ 10^6$ to convert from units of s^{-1} to units of PVU, as in Hakim et al. (1996). Gray contours are QGPV in PVU contoured every 0.5 PVU. Black "L" denotes location of 1000-hPa central sea-level pressure minimum and QGPV at the location of the 1000-hPa central sea-level pressure minimum is plotted in PVU.

Figure 4.1. Cross-section of a representative distribution of QGPV perturbations and their associated inverted height anomaly field at 1800 UTC 26 November 2019 (left). QGPV perturbations are shown by the color fill and filled every $10 \times 10^{-5}\ s^{-1}$. The inverted height anomaly field is contoured every 20 m, with negative height anomalies depicted as dashed contours and positive height anomalies depicted as full contours. 500 hPa QGPV perturbation at 1800 UTC 26 November 2019 with cross section shown from A to A' (right). QGPV perturbations are contoured every $10 \times 10^{-5}\ s^{-1}$ with dashed contours representing negative QGPV perturbation values and full contours representing positive QGPV perturbation values.

Figure 6.3. Adopted from Hoskins et al. (1985). Schematic of an upper-level potential vorticity (PV) anomaly interacting with a low-level baroclinic zone, demonstrating the mutual amplification that occurs upon superposition of upper- and lower-level PV anomalies. (a). An upper-level positive PV anomaly, indicated by the solid plus sign, and its associated circulation as shown by the solid arrows interacting with a low-level baroclinic zone. The strength of the PV-anomaly-associated circulation is indicated by arrow width. (b). A low-level positive potential temperature anomaly, indicated by the open plus sign, and its associated circulation shown by the open arrows interacting with the upper-level PV anomaly. The strength of the potential-temperature-anomaly-associated circulation is indicated by arrow width. As the two anomalies become phase locked, as is shown in depicted in (b.), the associated cyclonic circulations act to amplify each other.

Figure 6.4. Schematic of mutual amplification as in Hoskins et al. (1985) valid at 0000 UTC 26 November 2019. (a). 300 hPa QGPVP contoured in black and scaled by $-g\frac{\partial\theta}{\partial p}\ x\ 10^6$ to convert from units of s^{-1} to units of PVU, as in Hakim et al. (1996). Black contours are in PVU and plotted every 0.5 PVU. Geostrophic winds are derived from the inverted height anomalies associated with the QGPV anomalies in the SPERT layer and are plotted as barbs in knots. Black “L” denotes location of 950-hPa central sea-level pressure minimum and the 300 hPa QGPVP at the location of the 950-hPa central sea-level pressure minimum is plotted underneath the “L” in PVU. (b). 550 hPa QGPVP contoured in black and scaled by $-g\frac{\partial\theta}{\partial p}\ x\ 10^6$ to convert from units of s^{-1} to units of PVU, as in Hakim et al. (1996). Black contours are in PVU and plotted every 0.5 PVU. Geostrophic winds are derived from the inverted height anomalies associated with the QGPV anomalies in the SPERT layer and are plotted as barbs in knots. Black “L” denotes location of 950-hPa central sea-level pressure minimum and the 550 hPa QGPVP at the location of the 950-hPa central sea-level pressure minimum is plotted underneath the “L” in PVU. (c). 950 hPa geostrophic winds derived from the inverted height anomalies associated with the QGPV anomalies in the UPERT layer and plotted as barbs in knots. Boundary-level potential temperature

anomaly depicted by the color fill and plotted in Kelvin. Black “L” denotes location of 950-hPa central sea-level pressure minimum and boundary-level potential temperature anomaly at the location of the 950-hPa central sea-level pressure minimum is plotted underneath the “L” in PVU.

Figure 6.5. As in Fig. 6.3 but for 1200 UTC 26 November 2019.

Figure 6.6. As in Fig. 6.4 but for 0000 UTC 27 November 2019.

ii. List of Equations

$$\frac{d\zeta_g}{dt} = f_0 \frac{\partial \omega}{\partial p} \tag{1}$$

$$q = -g(\zeta_\theta + f)\left(\frac{\partial \theta}{\partial p}\right) \tag{2}$$

$$\eta = \nabla^2 \psi \tag{3}$$

$$\frac{\partial \zeta_g}{\partial t} = -\vec{V}_g \cdot \nabla\left(\zeta_g + f\right) + f_0 \frac{\partial \omega}{\partial p} \tag{4}$$

$$\left(\frac{\partial}{\partial t} + \vec{V}_g \cdot \nabla\right)\left(-\frac{\partial \phi}{\partial p}\right) - \sigma\omega = \frac{R\dot{Q}}{pc_p}. \tag{5}$$

$$\frac{f_0}{\sigma}\left(\frac{\partial}{\partial t} + \vec{V}_g \cdot \nabla\right)\left(-\frac{\partial \phi}{\partial p}\right) - f_0\omega = \frac{f_0 R\dot{Q}}{\sigma pc_p}. \tag{6}$$

$$\frac{\partial}{\partial p}\left[-\frac{f_0}{\sigma}\frac{\partial}{\partial p}\left(\frac{\partial \phi}{\partial t}\right) + \frac{f_0}{\sigma}\vec{V}_g \cdot \nabla\left(-\frac{\partial \phi}{\partial p}\right)\right] - f_0\frac{\partial \omega}{\partial p} = \frac{\partial}{\partial p}\left[\frac{f_0 R\dot{Q}}{\sigma pc_p}\right] \tag{7}$$

$$\frac{\partial}{\partial p}\left(\frac{f_0}{\sigma}\frac{\partial \chi}{\partial p}\right) = -\frac{\partial}{\partial p}\left[\frac{f_0}{\sigma}\vec{V}_g \cdot \nabla\left(\frac{\partial \phi}{\partial p}\right)\right] - f_0\frac{\partial \omega}{\partial p} - f_0\frac{\partial}{\partial p}\left[\frac{R\dot{Q}}{\sigma pc_p}\right]. \tag{8}$$

$$f_0\frac{\partial \omega}{\partial p} = \frac{\partial}{\partial p}\left(\frac{f_0}{\sigma}\frac{\partial \chi}{\partial p}\right) + \frac{\partial}{\partial p}\left[\frac{f_0}{\sigma}\vec{V}_g \cdot \nabla\left(\frac{\partial \phi}{\partial p}\right)\right]. \tag{9}$$

$$\zeta_g = \frac{1}{f_0}\nabla^2\phi \tag{10}$$

$$\frac{\partial}{\partial t}\left(\frac{1}{f_0}\nabla^2\phi\right) = -\vec{V}_g \cdot \nabla\left(\frac{1}{f_0}\nabla^2\phi + f\right) + f_0\frac{\partial \omega}{\partial p}. \tag{11}$$

$$\left(\frac{1}{f_0}\nabla^2\chi\right) = -\vec{V}_g \cdot \nabla\left(\frac{1}{f_0}\nabla^2\phi + f\right) - \frac{\partial}{\partial p}\left[\frac{f_0}{\sigma}\vec{V}_g \cdot \nabla\left(-\frac{\partial \phi}{\partial p}\right)\right] + \frac{\partial}{\partial p}\left(\frac{f_0}{\sigma}\frac{\partial \chi}{\partial p}\right). \tag{12}$$

$$\left[\frac{1}{f_0}\nabla^2 + \frac{\partial}{\partial p}\left(\frac{f_0}{\sigma}\frac{\partial}{\partial p}\right)\right]\chi = -\vec{V}_g \cdot \nabla\left(\frac{1}{f_0}\nabla^2\phi + f\right) - \frac{\partial}{\partial p}\left[\frac{f_0}{\sigma}\vec{V}_g \cdot \nabla\left(-\frac{\partial \phi}{\partial p}\right)\right]. \tag{13}$$

$$-\frac{\partial}{\partial p}\left[\frac{-f_0}{\sigma}\vec{V}_g \cdot \nabla\left(-\frac{\partial \phi}{\partial p}\right)\right] = -\vec{V}_g \cdot \nabla\frac{\partial}{\partial p}\left(\frac{f_0}{\sigma}\frac{\partial \phi}{\partial p}\right) - \frac{{f_0}^2}{\sigma}\frac{\partial \vec{V}_g}{\partial p} \cdot \nabla\frac{\partial \phi}{\partial p}. \tag{14}$$

$$\frac{\partial}{\partial t}\left[\nabla^2\phi + \frac{\partial}{\partial p}\left(\frac{f_0}{\sigma}\frac{\partial \phi}{\partial p}\right)\right] = -\vec{V}_g \cdot \nabla\left(\frac{1}{f_0}\nabla^2\phi + f + f_0\frac{\partial}{\partial p}\left(\frac{1}{\sigma}\frac{\partial \phi}{\partial p}\right)\right). \tag{15}$$

$$\frac{\partial}{\partial t}\left(\frac{1}{f_0}\nabla^2\phi + f + f_0\frac{\partial}{\partial p}\left(\frac{1}{\sigma}\frac{\partial\phi}{\partial p}\right)\right) = -\vec{V}_g\cdot\nabla\left(\frac{1}{f_0}\nabla^2\phi + f + f_0\frac{\partial}{\partial p}\left(\frac{1}{\sigma}\frac{\partial\phi}{\partial p}\right)\right) \tag{16}$$

$$q_g = \frac{1}{f_0}\nabla^2\phi + f + f_0\frac{\partial}{\partial p}\left(\frac{1}{\sigma}\frac{\partial\phi}{\partial p}\right) \tag{17}$$

$$1\ Bergeron = \frac{24\ hPa}{24\ hours} * \frac{sin(60°)}{sin(\varphi)}, \tag{18}$$

$$\frac{d\zeta}{dt} \approx -f\left(\nabla\cdot\vec{V}\right) \tag{19}$$

$$q_* = \frac{1}{f_0}\nabla^2\phi' + f_0\frac{\partial}{\partial p}\left(\frac{1}{\sigma}\frac{\partial\phi'}{\partial p}\right), \tag{20}$$

$$\frac{RT'}{p} = -\frac{\partial\phi'}{\partial p} \tag{21}$$

$$T' = -\frac{p}{R}\frac{\partial\phi'}{\partial p} \tag{22}$$

$$\theta' = -\frac{p}{R}\left(\frac{p_0}{p}\right)^{\frac{R}{c_p}}\frac{\partial\phi'}{\partial p} \tag{23}$$

$$q_* = \mathcal{L}(\phi'), \tag{24}$$

$$\mathcal{L} = \frac{1}{f_0}\nabla^2 + f_0\frac{\partial}{\partial p}\left(\frac{1}{\sigma}\frac{\partial}{\partial p}\right). \tag{25}$$

$$\phi_i{}' = \mathcal{L}^{-1}(q_{*i}). \tag{26}$$

$$f_0\frac{\partial\omega}{\partial p} = -\frac{\partial}{\partial p}\left[\frac{f_0}{\sigma}\vec{V}_g\cdot\nabla\left(-\frac{\partial\phi}{\partial p}\right)\right] - \frac{\partial}{\partial t}\left(-\frac{\partial\phi}{\partial p}\right) - f_0\frac{\partial}{\partial p}\left(\frac{R\dot{Q}}{pc_p\sigma}\right) \tag{27}$$

$$\left(\frac{1}{f_0}\nabla^2\chi\right) = -\vec{V}_g\cdot\nabla\left(\frac{1}{f_0}\nabla^2\phi + f\right) - \frac{\partial}{\partial p}\left[\frac{f_0}{\sigma}\vec{V}_g\cdot\nabla\left(-\frac{\partial\phi}{\partial p}\right)\right] - \frac{\partial}{\partial p}(\chi) - f_0\frac{\partial}{\partial p}\left(\frac{R\dot{Q}}{pc_p\sigma}\right) \tag{28}$$

$$\left(\frac{1}{f_0}\nabla^2 + \frac{\partial}{\partial p}\right)\chi = -\vec{V}_g\cdot\nabla\left(\frac{1}{f_0}\nabla^2\phi + f\right) - \frac{\partial}{\partial p}\left[\frac{f_0}{\sigma}\vec{V}_g\cdot\nabla\left(-\frac{\partial\phi}{\partial p}\right)\right] - f_0\frac{\partial}{\partial p}\left(\frac{R\dot{Q}}{pc_p\sigma}\right). \tag{29}$$

$$\frac{\partial}{\partial t}\left(\nabla^2\phi + \frac{\partial\phi}{\partial p}\right) = -\vec{V}_g\cdot\nabla\left(\frac{1}{f_0}\nabla^2\phi + f + f_0\frac{\partial}{\partial p}\left(\frac{1}{\sigma}\frac{\partial\phi}{\partial p}\right)\right) - f_0\frac{\partial}{\partial p}\left(\frac{R\dot{Q}}{pc_p\sigma}\right) \tag{30}$$

$$\frac{\partial}{\partial t}\left(\frac{1}{f_0}\nabla^2\phi + f + f_0\frac{\partial}{\partial p}\left(\frac{1}{\sigma}\frac{\partial\phi}{\partial p}\right)\right) = -\vec{V}_g\cdot\nabla\left(\frac{1}{f_0}\nabla^2\phi + f + f_0\frac{\partial}{\partial p}\left(\frac{1}{\sigma}\frac{\partial\phi}{\partial p}\right)\right) - f_0\frac{\partial}{\partial p}\left(\frac{R\dot{Q}}{pc_p\sigma}\right). \tag{31}$$

$$\frac{\partial u}{\partial x}+\frac{\partial v}{\partial y}+\frac{\partial \omega}{\partial p}=0 \tag{32}$$

$$\omega=\frac{dp}{dt}. \tag{33}$$

$$\nabla\cdot V+\frac{\partial \omega}{\partial p}=0. \tag{34}$$

$$\omega_{p_{sfc}}=-\int_{0}^{p_{sfc}}(\nabla\cdot V)\,\partial p= \frac{dp_{sfc}}{dt} \tag{35}$$

$$\frac{dp_{sfc}}{dt}= \frac{\partial p_{sfc}}{\partial t}+V_{as}\cdot\nabla p_{sfc}+w_s\frac{\partial p}{\partial z} \tag{36}$$

$$\frac{\partial p_{sfc}}{\partial t}=-\int_{0}^{p_{sfc}}(\nabla\cdot V)\,\partial p\,. \tag{37}$$

$$\frac{\partial p_{sfc}}{\partial t}=-\int_{50}^{950}(\nabla\cdot V)\,\partial p=\int_{50}^{950}\frac{\partial \omega}{\partial p}\partial p \tag{38}$$

$$\left(\nabla_p^2\;+\;\frac{f_0^2}{\sigma}\frac{\partial^2}{\partial p^2}\right)\omega=-2\nabla_p\cdot\vec{\boldsymbol{Q}} \tag{39}$$

$$\omega_{full}=\omega_{UPERT}+\omega_{MPERT}+\omega_{SPERT}\,. \tag{40}$$

$$\frac{\partial p_{sfc_{UPERT}}}{\partial t}\approx\int_{100}^{950}\frac{\partial \omega_{UPERT}}{\partial p}\partial p\,. \tag{41}$$

$$\frac{\partial p_{sfc_{MPERT}}}{\partial t}\approx\int_{100}^{950}\frac{\partial \omega_{MPERT}}{\partial p}\partial p \tag{42}$$

$$\frac{\partial p_{sfc_{SPERT}}}{\partial t}\approx\int_{100}^{950}\frac{\partial \omega_{SPERT}}{\partial p}\partial p \tag{43}$$

$$\int_{100}^{950}\frac{\partial \omega_{full}}{\partial p}\partial p\;=\int_{100}^{950}\frac{\partial \omega_{UPERT}}{\partial p}\partial p+\int_{100}^{950}\frac{\partial \omega_{MPERT}}{\partial p}\partial p+\int_{100}^{950}\frac{\partial \omega_{SPERT}}{\partial p}\partial p \tag{43}$$

$$\frac{\partial p_{sfc_{full}}}{\partial t}=\frac{\partial p_{sfc_{UPERT}}}{\partial t}+\frac{\partial p_{sfc_{MPERT}}}{\partial t}+\frac{\partial p_{sfc_{SPERT}}}{\partial t}. \tag{44}$$

$$\tfrac{d}{dt}(PV)\approx-g(\zeta+f)\tfrac{\partial\dot{\theta}}{\partial p} \tag{45}$$

iii. List of Abbreviations

EC	**E**xplosive **c**yclogenesis
EPV	**E**rtel **p**otential **v**orticity
HA	**H**eight **a**nomalies
GMT	**G**reenwich **M**ean **T**ime
hPa	**H**ecto**pa**scals
hr	**H**ou**r**
m	**M**eters
MPERT	**M**id-level **pert**urbation
NCEP GFS	**N**ational **C**enters for **E**nvironmental **P**rediction **G**lobal **F**orecast **S**ystem
nm	**N**autical **m**iles
NV19	**N**o**v**ember 20**19**
PV	**P**otential **v**orticity
PVA	**P**ositive **v**orticity **a**dvection
PVU	**P**otential **v**orticity **u**nits
QG	**Q**uasi**-g**eostrophic
QGPV	**Q**uasi**-g**eostrophic **p**otential **v**orticity
QGPVP	**Q**uasi**-g**eostrophic **p**otential **v**orticity **p**erturbations
R84	**R**oebber 19**84**
s	**S**econds
SPERT	**S**urface-level **pert**urbation
UPERT	**U**pper-level **pert**urbation
UTC	**U**niversal **T**ime **C**oordinated
WRF	**W**eather **R**esearch and **F**orecasting
ZH17	**Zh**ang et al. 20**17**

1. INTRODUCTION

One of the most compelling concepts in all of meteorology is the process of cyclogenesis. Cyclogenesis is defined in the Glossary of Meteorology as, “any development or strengthening of cyclonic circulation in the atmosphere”. At any given time in a single hemisphere, there are typically 10 unique low pressure systems, each with varying intensity and spatial extent. Of this handful of low pressure systems, a portion of them will be experiencing cyclogenesis and, if this cyclogenesis occurs in proximity to land or maritime commerce, the associated low pressure systems produce substantial socioeconomic impacts (e.g., Lynott and Cramer 1966; Bosart 1981; Gyakum 1983a; Revell and Gorman 2003; Hultquist et al. 2006; Odell et al. 2013). Low pressure systems focus precipitation, wind, and cloud growth within a small portion of the overall cyclone structure, making the conditions experienced in the vicinity of these systems extremely variable. Organized low pressure systems can occur in a variety of environments: in the low-latitude, convectively buoyant tropics, in the mid-latitude, baroclinic, and temperate extratropics, and in the high-latitude, baroclinic, and frigid polar regions. Although there are a plethora of dynamical processes which can individually or collectively force cyclogenesis, the same basic principle is accomplished by any combination of them: concentrated vertical motion that accomplishes net evacuation of mass, which can be forced by vertical couplets of divergence that, in turn, can be related to the rearrangement of vorticity in the vertical (Sutcliffe 1939; 1947). This rearrangement of vorticity in the vertical can lead to extreme vertical motion and rapid cyclogenesis, deemed “explosive” cyclogenesis, which continues to captivate atmospheric scientists to this day.

Explosive cyclogenesis (EC) events have enjoyed renewed interest among atmospheric scientists since the beginning of the 1980s. These EC events, or “bombs”, are defined as cyclones that experience a central pressure fall of at least 24 hPa over a 24-hour period at an equivalent latitude of 60°N (Sanders and Gyakum 1980). Early studies regarding the geographical distribution of rapid cyclogenesis have concluded that northern hemispheric EC events are most likely to occur off of the east coast of continents during the cold season, as this is where and when the baroclinicity between the land and ocean surface is maximized (Sanders and Gyakum 1980; Roebber 1984). Aside from the east coasts of continents, another maximum in climatological EC events exists a few hundred miles south of Alaska in the northeastern Pacific Ocean as noted by Roebber 1984 (hereafter R84). In that paper, it was first theorized that this particular maximum exists as a result of Arctic air masses moving southward over the relatively warm Alaska current, which results in intense low-level baroclinicity. Decaying upstream cyclones over the Gulf of Alaska were also thought to aid in the location of the climatological maximum south of Alaska, although these were thought to be of secondary importance.

More recent studies found similar preferred regions as those described in R84 (Wang and Rogers 2001; Allen et al. 2010; Zhang et al. 2017). In both the northern and southern hemisphere, a high degree of interannual variability was observed in an analysis of cyclone events from 1979 to 2008 (Allen et al. 2010). As noted in Wang and Rogers (2001) and Zhang et al. (2017) (hereafter ZH17), the occurrence and distribution of explosive development events are highly correlated with the position and strength of two primary variables: 1) upper-level forcing in the form of the jet stream and/or a vorticity maximum, and 2) low-level baroclinicity. Understanding the physical nature of the interaction between these two primary forcings and the potential for explosive development is essential in the quest to enhance predictability of EC events, especially since EC events are becoming increasingly common in both the Northern and Southern Hemisphere (Lim and Simmonds 2002).

The reason why these EC events were initially puzzling to atmospheric scientists is that it was originally theorized that EC was forced by different dynamical processes than more modest cyclogenesis events (R84). This theory was quickly disputed in an exhaustive number of studies in the 1980's and 1990's, and it was discovered that EC events are driven by the same two fundamental forcings: substantial low-level baroclinic instability supported by distinct upper-level features (Sanders 1986a; Manobianco 1989b; Wash et al. 1992). Along with the fundamental forcings, particularly robust versions of the auxiliary cyclogenetic forcings are characteristic of EC events, namely: 1) strong upper-level forcing (Sanders 1986a; Elsberry and Kirchoffer 1988; Pang and Fu 2017; Heo et al. 2019), 2) abundant diabatic influences in the form of sea-surface heat fluxes (Davis and Emanuel 1988; Roebber 1989; Kuo et al. 1991a; Gyakum and Danielson 2000), 3) differential diabatic heating (Bosart 1981; Mullen and Baumhefner 1988; Boettcher and Wernli 2011), and 4) latent heat release (Gyakum 1983b; Reed et al. 1988; Kuo et al. 1991b; Kuwano-Yoshida and Enomoto 2013). It is currently accepted that EC events differ from "average" cyclogenesis events in that the interactions and collaboration of ordinary cyclogenetic forcings are robustly enhanced in EC events as a result of the distribution and intensity of diabatic processes. Latent heat release is particularly important to EC events, as it increases the column average temperature in its vicinity and is thereby responsible for decreasing the wavelength between the downstream ridge and upstream trough and increasing vorticity advection in the region of the cyclone prior to the onset of rapid deepening (Roebber 1993). By decreasing this wavelength, more dramatic positive vorticity advection (PVA) ahead of the cyclone allows for net column divergence and rising motion, enhancing the potential for development. Latent heat release initiates this vorticity advection, net column divergence, and rising motion, but this is quickly amplified when an upper-level trough further enhances vorticity advection in proximity to the cyclone. Despite latent heat release being a significant forcing for EC events (e.g., Kuo and Reed 1988; Reed et al. 1988; Manobianco 1989), any cyclogenetic forcing could contribute a substantial amount to the process of explosive development. The relative contribution of these forcings can be compared using the basic state variable approach, which casts the analysis of the cyclone lifecycle and development in terms of variables such as temperature, geopotential height, and mixing ratio in a balance framework. This allows for the analysis of vertical motion, divergence, and surface pressure falls, often theoretically based on the vorticity equation. One direct relation between basic state variables and the vorticity equation is given by the quasi-geostrophic vorticity equation

$$\frac{d\zeta_g}{dt} = f_0 \frac{\partial \omega}{\partial p} \tag{1}$$

where ω is the isobaric vertical velocity and $\frac{d\zeta_g}{dt}$ is the Lagrangian time tendency of the geostrophic relative vorticity. From equation (1), it is trivial to relate vertical gradients of ω to regions of increasing (decreasing) geostrophic relative vorticity, thus physically linking rising motion (sinking motion) and surface pressure falls (surface pressure rises). Thus, regions that are favorable for cyclogenesis are readily identified given a vertical distribution of ω.

Another equally accepted and well-developed method of diagnosing development is the consideration of a single variable: the quasi-geostrophic potential vorticity (QGPV). By following the evolution of a conserved variable that incorporates circulation and stability, the QGPV, one can consider changes in circulation as related to attendant changes in stability by carefully following the QGPV through time and space. The consideration of this comprehensive variable to assess cyclogenesis and synoptic-scale motion is the basis of what is known as "PV thinking", which was first introduced by Hoskins et al. (1985) and has been described and utilized in numerous subsequent studies (i.e., Reed et al. 1992; Stoelinga 1996; Brennan et al. 2008; Berry and Thorncroft 2012). The tracking of this one flavor of the total PV offers an equally insightful perspective on the forcings for development and will be used in concert in this thesis with the basic state variable relation shown in equation (1).

In the late 1970's and early-middle 1980's, the notion of PV thinking was resurrected by the work of Hoskins et al. (1985) and has since enhanced our understanding of cyclogenesis. PV, or more formally isentropic PV, is a product of the absolute vorticity and the static stability in isentropic coordinates and can be written as

$$q = -g(\zeta_\theta + f)\left(\frac{\partial\theta}{\partial p}\right) \tag{2}$$

where q is the isentropic PV, g is the acceleration due to gravity, ζ_θ is the isentropic relative vorticity, f is the Coriolis parameter, and $-\frac{\partial\theta}{\partial p}$ is the static stability. In the absence of diabatic heating and friction, the PV is conserved. Thus, the vorticity can be altered by either changing the latitude or by adiabatically changing the stratification between two isentropic levels. Therefore, for adiabatic and frictionless flow, the value of the PV for a parcel remains constant; however, the relative magnitude between the circulation of the parcel, $\zeta_\theta + f$, and the stratification of the parcel, $\frac{\partial\theta}{\partial p}$, can change. The PV thinking view offers a succinct approach to the underlying dynamics of cyclogenesis while offering trivial methods to derive the cloud and precipitation-producing vertical motions.

There are two key aspects of the PV that present it as a useful tool in understanding EC events: the principle of conservation and the principle of invertibility (Hoskins et al. 1985; Davis and Emanuel 1991; Stoelinga 1996; Morgan and Nielsen-Gammon 1998). The notion of PV conservation was first developed by Rossby (1940) and applies strictly to adiabatic, frictionless flow. Under such constraints, any change to PV anomalies[1] in the atmosphere can be directly attributed to frictional dissipation and/or diabatic erosion or generation.

Ernst Kleinschmidt was a pioneer in diagnosing cyclogenesis using PV anomalies in the upper-troposphere, along with emphasizing the usefulness of the invertibility principle of PV (Kleinschmidt 1950a, b; 1951; 1955; 1957). The reader is directed to Hoskins et al. (1985) for a more complete overview of Kleinschmidt's early work. Kleinschmidt reasoned that one can also diagnose the structure of the flow from the spatial distribution of PV. His ideas were revolutionary in the quest to understand cyclogenesis for the time but were unfortunately overshadowed by the emergence of the revolutionary theory of baroclinic instability. Hoskins et al. (1985) resurrected the idea of PV inversion some three and a half decades later, which has resulted in a proliferation of PV inversion studies in the literature since. As meticulously outlined in Hoskins et al. (1985) and Davis and Emmanuel (1991), the invertibility principle applied to PV states that from the absolute vorticity and static stability which multiply to produce a distribution of PV, one should be able to solve for the zonal and meridional winds (from the absolute vorticity) and the geopotential height distribution (from the vertical derivative of temperature captured in the static stability) using a second-order inverse Laplacian operator. So, if one has a 3D distribution of PV anomalies in the atmosphere, it is possible to determine the winds and the geopotential height distributions associated with said anomalies. This result of the invertibility principle applied to a

---

[1] In this thesis, any anomaly discussed will be attributed to an anomaly in time, rather than an anomaly in space. Quasi-geostrophic potential vorticity (QGPV) anomalies will be calculated by taking the time-mean of a distribution of QGPV and subtracting the instantaneous QGPV at each preferred time-step over the model domain.

distribution of PV is the essence of what Kleinschmidt (1950a, b; 1951; 1955; 1957) first theorized and what this thesis will aim to exploit.

A quasi-geostrophic (QG) approach to PV thinking will be utilized in this thesis. Under the QG approximation, ageostrophic motions are assumed to be small in comparison to geostrophic motions such that the Coriolis force is nearly balanced by the pressure gradient force (Eliassen 1984). The errors involved in making the QG approximation in the middle latitudes are relatively small, especially when compared to the errors involved in analyses of current conditions and forecasting (Eliassen 1984). One can use the QG approximation to simplify the five primitive equations of motions into one equation which incorporates knowledge of the basic state variables such as temperature, geopotential height, and vertical motion. Since geostrophic motions are assumed to dominate in a QG-framework, we can relate the absolute vorticity to the mass field using

$$\eta = \nabla^2 \psi \tag{3}$$

where η is the absolute vorticity and ψ is a non-divergent streamfunction following the flow. The relationship in equation (3) is crucial in that it specifies the relationship between a distribution of vorticity and a streamfunction field, which is one piece of the knowledge of the basic state variables as described in QG-framework.

Utilizing the QG assumptions, we begin the derivation of the QGPV with the QG vorticity equation given by

$$\frac{\partial \zeta_g}{\partial t} = -\vec{V}_g \cdot \nabla(\zeta_g + f) + f_0 \frac{\partial \omega}{\partial p} \tag{4}$$

and the QG thermodynamic energy equation given by

$$\left(\frac{\partial}{\partial t} + \vec{V}_g \cdot \nabla\right)\left(-\frac{\partial \phi}{\partial p}\right) - \sigma\omega = \frac{R\dot{Q}}{pc_p}. \tag{5}$$

If we multiply equation (5) by $\frac{f_0}{\sigma}$, we get

$$\frac{f_0}{\sigma}\left(\frac{\partial}{\partial t} + \vec{V}_g \cdot \nabla\right)\left(-\frac{\partial \phi}{\partial p}\right) - f_0\omega = \frac{f_0 R\dot{Q}}{\sigma pc_p}. \tag{6}$$

Then, if we differentiate with respect to pressure, equation (6) becomes

$$\frac{\partial}{\partial p}\left[-\frac{f_0}{\sigma}\frac{\partial}{\partial p}\left(\frac{\partial\phi}{\partial t}\right)+\frac{f_0}{\sigma}\vec{V}_g\cdot\nabla\left(-\frac{\partial\phi}{\partial p}\right)\right]-f_0\frac{\partial\omega}{\partial p}=\frac{\partial}{\partial p}\left[\frac{f_0R\dot{Q}}{\sigma p c_p}\right] \tag{7}$$

which, along with defining $\chi=\frac{\partial\phi}{\partial t}$, can be rearranged into

$$\frac{\partial}{\partial p}\left(\frac{f_0}{\sigma}\frac{\partial\chi}{\partial p}\right)=-\frac{\partial}{\partial p}\left[\frac{f_0}{\sigma}\vec{V}_g\cdot\nabla\left(\frac{\partial\phi}{\partial p}\right)\right]-f_0\frac{\partial\omega}{\partial p}-f_0\frac{\partial}{\partial p}\left[\frac{R\dot{Q}}{\sigma p c_p}\right]. \tag{8}$$

Equation (8) can then be solved for the vertical stretching term, the second term on the right hand side of the equation (8), while neglecting diabatic heating:

$$f_0\frac{\partial\omega}{\partial p}=\frac{\partial}{\partial p}\left(\frac{f_0}{\sigma}\frac{\partial\chi}{\partial p}\right)+\frac{\partial}{\partial p}\left[\frac{f_0}{\sigma}\vec{V}_g\cdot\nabla\left(\frac{\partial\phi}{\partial p}\right)\right]. \tag{9}$$

If we now utilize equation (4), the geostrophic relative vorticity can be expressed as

$$\zeta_g=\frac{1}{f_0}\nabla^2\phi \tag{10}$$

and equation (4) can be rewritten as

$$\frac{\partial}{\partial t}\left(\frac{1}{f_0}\nabla^2\phi\right)=-\vec{V}_g\cdot\nabla\left(\frac{1}{f_0}\nabla^2\phi+f\right)+f_0\frac{\partial\omega}{\partial p}. \tag{11}$$

We can then combine equation (9) and equation (11) using the vertical stretching term:

$$\left(\frac{1}{f_0}\nabla^2\chi\right)=-\vec{V}_g\cdot\nabla\left(\frac{1}{f_0}\nabla^2\phi+f\right)-\frac{\partial}{\partial p}\left[\frac{f_0}{\sigma}\vec{V}_g\cdot\nabla\left(-\frac{\partial\phi}{\partial p}\right)\right]+\frac{\partial}{\partial p}\left(\frac{f_0}{\sigma}\frac{\partial\chi}{\partial p}\right). \tag{12}$$

The geopotential tendency terms can also be moved to the left hand side of the equation:

$$\left[\frac{1}{f_0}\nabla^2+\frac{\partial}{\partial p}\left(\frac{f_0}{\sigma}\frac{\partial}{\partial p}\right)\right]\chi=-\vec{V}_g\cdot\nabla\left(\frac{1}{f_0}\nabla^2\phi+f\right)-\frac{\partial}{\partial p}\left[\frac{f_0}{\sigma}\vec{V}_g\cdot\nabla\left(-\frac{\partial\phi}{\partial p}\right)\right]. \tag{13}$$

Using the chain rule on the second term on the right hand side of equation (13) yields

$$-\frac{\partial}{\partial p}\left[\frac{-f_0}{\sigma}\vec{V}_g\cdot\nabla\left(-\frac{\partial\phi}{\partial p}\right)\right]=-\vec{V}_g\cdot\nabla\frac{\partial}{\partial p}\left(\frac{f_0}{\sigma}\frac{\partial\phi}{\partial p}\right)-\frac{{f_0}^2}{\sigma}\frac{\partial\vec{V}_g}{\partial p}\cdot\nabla\frac{\partial\phi}{\partial p}. \tag{14}$$

The second term on the right hand side of equation (14) is identically zero since the thermal wind $\left(-\frac{\partial \vec{V}_g}{\partial p}\right)$ is parallel to the isotherms $\left(\frac{\partial \phi}{\partial p} = \frac{-RT}{p}\right)$. Since $\chi = \frac{\partial \phi}{\partial t}$ and both terms on the right-hand side of equation (13) involve a geostrophic advection term, it can be rewritten as

$$\frac{\partial}{\partial t}\left[\nabla^2 \phi + \frac{\partial}{\partial p}\left(\frac{f_0}{\sigma}\frac{\partial \phi}{\partial p}\right)\right] = -\vec{V}_g \cdot \nabla\left(\frac{1}{f_0}\nabla^2 \phi + f + f_0 \frac{\partial}{\partial p}\left(\frac{1}{\sigma}\frac{\partial \phi}{\partial p}\right)\right). \qquad (15)$$

We thus reach a conservation expression for the QGPV:

$$\frac{\partial}{\partial t}\left(\frac{1}{f_0}\nabla^2 \phi + f + f_0 \frac{\partial}{\partial p}\left(\frac{1}{\sigma}\frac{\partial \phi}{\partial p}\right)\right) = -\vec{V}_g \cdot \nabla\left(\frac{1}{f_0}\nabla^2 \phi + f + f_0 \frac{\partial}{\partial p}\left(\frac{1}{\sigma}\frac{\partial \phi}{\partial p}\right)\right) \qquad (16)$$

where the QGPV is given as

$$q_g = \frac{1}{f_0}\nabla^2 \phi + f + f_0 \frac{\partial}{\partial p}\left(\frac{1}{\sigma}\frac{\partial \phi}{\partial p}\right) \qquad (17)$$

and $\frac{1}{f_0}\nabla^2 \phi$ is the geostrophic relative vorticity, f is the planetary vorticity, and $f_0 \frac{\partial}{\partial p}\left(\frac{1}{\sigma}\frac{\partial \phi}{\partial p}\right)$ is a lapse rate term related to the vertical derivative of temperature and static stability. The lapse rate term will hereafter be referred to as the "stretching vorticity" for convenience.

Beyond simply inverting a distribution of QGPV, it is possible to invert the different flavors of the QGPV as the QGPV arises from a linear operator acting on a distribution of geopotential, ϕ. This means that, as the QGPV is the sum of the relative vorticity, planetary vorticity, and the "stretching" vorticity, all three of these pieces of the total QGPV can be separately isolated and inverted. We will define QGPV perturbations as the difference between the instantaneous QGPV and the time-mean QGPV over a specified analysis interval. An additional partition results from the fact that the relative vorticity can be split into curvature and shear vorticity, allowing for further isolation of terms within a total QGPV anomaly. The usefulness of splitting the QGPV does not cease at separating and isolating the individual terms of a single QGPV anomaly. For example, Davis and Emanuel (1991) made use of partitioning their PV inversion into different layers of the atmosphere to see how PV anomalies located at 500 hPa and above interact with PV anomalies located between 850 hPa and 700 hPa. The versatility of the QGPV inversion in terms of potential for customization is quickly realized in that many different isobaric levels can be partitioned and compared to see how the QGPV associated with different levels and processes is interacting with itself and how that interaction is affecting development at the surface.

This thesis will employ the partitioned invertibility principle on a distribution of QGPV associated with a rather interesting case of explosive cyclogenesis that occurred over the northeastern Pacific Ocean in late November 2019. Chapter 2 will explain the motivation for choosing the object case of cyclogenesis and will also provide a synoptic overview of the event at six-hourly intervals beginning just prior to rapid development and ending six hours after landfall on the west coast of the United States. Chapter 3 will highlight the data and methods used to employ QGPV inversion, including a detailed description of the Weather Research and Forecasting (WRF) model which served as the backbone of the analysis presented. Chapter 4 will show that the object cyclone, from the PV-thinking, QGPV inversion perspective, was primarily driven by lower tropospheric forcings. Chapter 5 will show that the object cyclone, from the basic state variable, QG-omega perspective, was almost equally driven by upper and lower tropospheric forcings. Chapter 6 will include some discussion about the contradictory diagnoses that arise from consideration of the two different analysis methods as well as offering concluding thoughts on the comparison of QGPV inversion and QG-omega analysis techniques and, briefly, theoretical applications of these methods in real-time diagnoses of cyclogenesis.

2. OVERVIEW

The second chapter in this thesis highlights the synoptic environment in which the November 2019 (NV19) storm explosively deepened in the northeast Pacific Ocean. The anomalous nature of this explosive development is put in context of the storm track, intensification rate, and development location compared to prior studies of EC events. It follows that the 20 hPa of deepening accomplished by the NV19 storm in the 6 hours preceding landfall is comparable to the maximum deepening rate accomplished by the strongest extratropical cyclone in recorded history.

2.1 Synoptic Overview

This overview will utilize data from the National Centers for Environmental Prediction Global Forecast System (NCEP GFS) analysis of the NV19 storm and will focus on twelve hour increments from 1200 UTC 25 November 2019, near the nascent stage of development, to 1200 UTC 27 November 2019, slightly past the period of its most rapid development and about nine hours after the storm made landfall on the west coast of the United States.

2.1.1 <u>1200 UTC 25 November 2019</u>

Twelve hours before the NV19 storm formed its own closed circulation at sea-level, a predominantly zonally-oriented surface baroclinic zone, indicated by the tight gradient of 950 hPa equivalent potential temperature (θ_e) contours, was draped southeastward from an almost cutoff low pressure system to the west through the center of a fairly strong surface anti-cyclone to the east (Fig. 2.1a). At the intersection of this baroclinic zone with a more meridionally oriented cold frontal baroclinic zone, the yellow-highlighted “X” indicates the 950 hPa vorticity maximum within a broad, bowing pressure trough (Fig. 2.1a). The same baroclinic zones were reflected in the isentropes at 850 hPa, with positive frontogenesis being indicated along the surface cold and warm fronts (Fig. 2.1a; Fig. 2.1b). The strongest positive frontogenesis was located along the warm front near and to the east of the surface development region (Fig. 2.1b). At 500 hPa, the surface development region was ahead of the nearly cutoff low pressure center to the southwest and a shortwave feature to the north-northwest (Fig. 2.1c).

The surface development region was also centered in the right entrance region of a downstream, anticyclonically-curved jet streak at 300 hPa (Fig. 2.1d).

2.1.2 <u>0000 UTC 26 November 2019</u>

At 0000 UTC 26 November 2019, a weak surface cyclone had just begun to develop along the baroclinic zone stretching zonally through the anticyclone (Fig. 2.2a). The 850 hPa baroclinic zone and positive frontogenesis maintained a similar spatial relationship with the developing surface cyclone (Fig. 2.2b). The frontogenesis located to the east and southeast of the surface cyclone was occurring along the developing warm front. The shortwave feature at 500 hPa began to strengthen to the surface cyclone's northwest, indicated by the increase in positive relative vorticity at the shortwave axis (Fig. 2.2c). The presence of this shortwave forced PVA by the thermal wind in the vicinity of the surface cyclone, which was strongest due north of the surface cyclone center. At 300 hPa, the surface cyclone continued to be located in the right entrance region of the downstream, anticyclonically-curved jetstreak (Fig. 2.2d). The shortwave feature analyzed at 500 hPa is also visible at 300 hPa at this time, with the axis of the 300 hPa shortwave being centered slightly to the northwest of the axis of the 500 hPa shortwave.

2.1.3 <u>1200 UTC 26 November 2019</u>

Twelve hours after the initial development of the cyclone, the NV19 storm had completely bisected the anticyclone near which it initially developed (Fig. 2.3a). Well-defined cold and warm fronts now characterized the cyclone, as shown by the 950 hPa θ_e, with pressure troughs clearly associated with both fronts. At this time, the storm was beginning its twelve-hour period of most rapid deepening as it approached to the California-Oregon border. The primary band of positive frontogenesis at 850 hPa continued to be associated with the surface warm front, but a band of weaker, positive frontogenesis was analyzed well behind the storm along the surface cold front (Fig. 2.3b). The surface cyclone center was located at the apex of a thermal ridge as seen in the 850 hPa isentropes. Over the twelve hours after initial development, rapid intensification and elongation of the 500 hPa positive vorticity occurred to the west-northwest of the surface cyclone, coincident with a sharp temperature gradient, which suggests that active upper frontogenesis was ongoing at this time (Fig. 2.3c). This intensification focused vigorous PVA by the thermal wind directly above the surface cyclone, an indication of greater divergence aloft than near the surface and synoptic-scale upward motion as described in Sutcliffe (1947). In a direct response to this forcing, the central pressure of the NV19 storm dropped at least 20 hPa from the analysis twelve hours prior (Figs. 2.2a; 2.3a). The thermal trough at 500 hPa lagged behind the geopotential height trough with a thermal ridge slightly downstream of it, but the thermal gradient directly northwest of the cyclone tightened compared to twelve hours prior. This same region of isentropic gradient intensification experienced a wind speed increase at 300 hPa, at the base of the shortwave feature (Fig. 2.3d). This wind intensification situated the NV19 storm in the left exit region of the newly formed jet streak, the third successive analysis time in which upper-level divergence was aiding in mass evacuation and rising motion above the surface cyclone.

2.1.4 0000 UTC 27 November 2019

Twenty-four hours after initial development, the storm had deepened an additional 43 hPa to a central pressure of less than 980 hPa, well exceeding the definition of explosive cyclogenesis defined in Sanders and Gyakum 1980 (Fig. 2.4a). The storm was just making landfall on the west coast of the United States, with occlusion beginning as indicated by the locations of the fronts. Once again, the primary positive frontogenesis at 850 hPa was associated with the warm front, undoubtedly reinforced by steep topography (Fig. 2.4b). The isentropes lost their tight gradient near the surface cyclone while the storm remained located in a now weaker thermal ridge. A well-developed trough with substantial PVA by the thermal wind and an elongated streamer of vorticity at 500 hPa were still affecting the surface cyclone and now regions to its northeast (Fig. 2.4c). The strongest of this PVA by the thermal wind was located to the northeast of the cyclone. The isentropes became even more tightly packed upstream of the cyclone, indicating the continued presence and development of the upper front, while the wavelength between the upstream thermal trough and downstream thermal ridge decreased. The jetstreak behind the surface cyclone increased in spatial coverage and decreased in magnitude as it raced southeastward on the upstream side of a newly carved out upper trough (Fig. 2.4d). The strongest winds were situated upstream of the trough axis as the trough became more meridional oriented.

2.1.5 <u>1200 UTC 27 November 2019</u>

About nine hours after making landfall, the NV19 storm began to fill as occlusion continued to occur and the storm moved inland (Fig. 2.5a). A broad occluded-cold front dominated the storm domain, as the positive frontogenesis at 850 hPa previously occurring along the warm front was no longer active (Fig. 2.5b). The lack of well-defined frontal regions is indicated by the relatively disorganized distribution of the 850 hPa isentropes. At 500 hPa, a circular geopotential height minimum characterized by strong PVA on its southern side was located directly over the surface cyclone (Fig. 2.5c). The isentropes at this level were strongly packed on the western and southern side of the upper trough, coincident with a linear shear vorticity feature, indicative of the strong upper-front. An increase in wind speed associated with the jetstreak on the upstream side of the trough at 300 hPa offered similar testimony (Fig. 2.5d).

2.2 Comparison to Climatology

Northwesterly flow cyclogenesis events off the northwest coast of the United States have been well-documented in a number of previous studies (e.g., Reed and Albright 1986; Yoshiike and Kawamura 2009; Lang and Martin 2012; Iwao et al. 2012; Iizuka et al. 2013). From a synoptic-scale perspective, the NV19 case was very similar to those described in Stoelinga (1996), Lang and Martin (2012), and Martin (2014) in which an upper-level frontal system in northwesterly flow spawned the development of a mid-tropospheric shortwave. The development of the upper-level frontal system was mobilized by the "Shapiro effect" (i.e., Rotunno et al. 1994) with cold air advection along the jet axis, which resulted in downward advection of high PV air through the jet core into the troposphere. The phasing of the middle- and upper-tropospheric high PV air coupled with a positive low-level potential temperature anomaly set the stage for a significant surface cyclogenesis event (Bretherton 1966; Hoskins et al. 1985).

The storm brought heavy liquid and frozen precipitation and isolated pockets of winds in excess of 100 mph to the states of Washington, Oregon, and portions of Northern California, wreaking havoc on late-November holiday travel. In addition to these impacts, the storm also set November low pressure records in Medford, OR (981.4 hPa) and Eureka, CA (984.4 hPa) and the all-time low pressure record for the state of California (973.4 hPa in Crescent City). At 0333 UTC 27 November 2019, the Scripps

Institution of Oceanography's *94 Cape Mendocino* buoy off of Cape Mendocino, CA registered record significant wave heights of 43.1 feet, which included a remarkable measured wave height of 75 feet, while the neighboring *No. 168 Humboldt Bay North Spit* buoy was recording significant wave heights of 37.6 feet (Duginski 2019). The storm accomplished a remarkable 24-hour maximum central pressure deepening rate of 43 hPa between 0000 UTC 26 November 2019 and 0000 UTC 27 November 2019 and an astounding 3-hour deepening rate of 12 hPa from 1500 - 1800 UTC 26 November 2019. Both of these deepening periods occurred just before the storm made landfall at the California-Oregon border between 0000 UTC and 0300 UTC 27 November 2019. Though this storm did not approach the intensification rate of some other extraordinary cyclones from the Northern hemispheric record (i.e., Sanders 1986a; Lim and Simmonds 2002; Kuwano-Yoshida and Asuma 2008; Odell et al. 2013; ZH17), it was among the most intense ever (and with a rare storm track) for the northeast Pacific region.

The anomalous nature of the November 2019 storm will be assessed using three different primary characteristics: storm track, deepening rate, and location of maximum deepening. First, this storm took an unusual path when considering climatologies of EC events in the north Pacific Ocean. R84 compiled a climatology of daily EC events occurring in the Northern Hemisphere over a seven year period from 1976 to 1982. Wang and Rogers (2001) compiled a similar climatology for the period from 1985 to 1996 while ZH17 focused exclusively on north Pacific Ocean storms from 2000 to 2015. All three studies concluded that Northern Hemisphere EC is most common in three regions: off the east coast of Japan, off the east coast of the United States and southeast Canada, and in the central Gulf of Alaska. The analysis of individual tracks from ZH17 suggests that there is a clear preference for these storms to propagate from southwest to northeast as they rapidly deepen into substantial midlatitude cyclones (Fig. 2.6). ZH17 further separated their explosive deepening events into five geographic regions: the Japan–Okhotsk Sea (JOS), the northwestern Pacific Ocean (NWP), the west-central Pacific Ocean (WCP), the east-central Pacific Ocean (ECP), and the northeastern Pacific Ocean (NEP) in order for individual storm tracks from storms developing over the same geographic conditions to be separately visualized. The NEP storm tracks exhibit largely southwest-to-northeast tracks, with some instances of purely meridional motion (Fig.

2.6e). In the case of the NV19 (November 2019) storm, the cyclone track from the GFS analysis over the northeastern Pacific Ocean was oriented northwest-to-southeast as the storm developed near 48°N, 147.5°W and made landfall in the United States at 42.5°N, 125.5°W (Fig. 2.6.1e). In fact, from 1800 UTC 25 November to 0300 UTC 26 November, the GFS analysis cyclone track travelled nearly due east before taking a gradual northwest-to-southeast path towards the United States west coast in the subsequent hours (Figs. 2.1a-2.3a; Fig. 2.6.1e). This storm track was oriented roughly 90° out of phase from almost all the tracks of the 12 cases of rapidly deepening NEP storms identified in ZH17 (Fig. 2.6.1e).

In an effort to quantify deepening rate, Sanders and Gyakum (1980) defined a measurement to classify an EC event. This measurement is known as the “Bergeron" and is defined as

$$1\,Bergeron = \frac{24\,hPa}{24\,hours} * \frac{sin(60°)}{sin(\varphi)}, \tag{18}$$

where φ is the latitude of the cyclone’s center and 60 °N is the adjusted latitude of geographic development. Any storm that accomplishes a deepening rate equal to or greater than one Bergeron meets the criteria for an EC event as defined by Sanders and Gyakum (1980), and more recent studies have specified thresholds for EC events to further their quantification. ZH17 defined four different classifications of EC events: “weak” cyclogenesis as defined by a maximum deepening rate of 1.00 to 1.29 Bergerons, “moderate” cyclogenesis as defined by a maximum deepening rate of 1.30 to 1.69 Bergerons, “strong” cyclogenesis as defined by a maximum deepening rate of 1.70 to 2.29 Bergerons, and “super” cyclogenesis as defined by a maximum deepening rate of greater than 2.30 Bergerons. ZH17 also used an adjusted latitude for development of 45°N, as this was more representative of the mean latitude of development within the northern Pacific Ocean. The NV19 storm began cyclogenesis at a latitude of 48 °N and began cyclolysis at a latitude of 42.5°N, resulting in a mean latitude of development of 45.25°N to be used in calculating the storm’s deepening rate in Bergerons. The maximum 24 hour central pressure fall experienced by the storm was 43 hPa from 0000 UTC 26 November 2019 to 0000 UTC 27 November 2019. Regardless of choice of the Sanders and Gyakum (1980) Bergeron value or the ZH17 Bergeron value and using the value of 43 hPa of deepening in 24 hours, the NV19 storm fell within the “strong” category as defined by ZH17, accomplishing a maximum deepening rate of 2.18 Bergerons using the definition in Sanders and Gyakum (1980) and 1.78 Bergerons using the definition in ZH17. The deepening rate of 1.78 Bergerons can be compared to other EC events within the NEP from the analysis in ZH17. After doing so, the deepening rate of the NV19 storm is within the 91st percentile of the 120 cases of EC in the NEP analyzed by ZH17, further testifying to the anomalous nature of the storm.

It is of interest to compare the NV19 storm to the strongest midlatitude cyclone ever recorded: the *Braer* storm of 1993. This storm achieved its record minimum central sea level pressure of 914 hPa on 10 January 1993 at 1800 UTC (Odell et al. 2013) and the maximum 24-hour deepening rate (78 hPa) of any extratropical cyclone (Lim and Simmonds 2002). The *Braer* storm, named for the oil tanker it sank, was a classic Petterssen and Smebye (1971) Type B cyclogenesis event, in which a robust maximum of upper-level PV superimposed with the lower-level, northern extension of the Gulf Stream and forced intense mutual amplification between the upper-level positive PV anomaly and the lower-level potential temperature anomaly as the storm tracked to the northeast. An EC deepening value of 3.25 Bergerons is calculated employing an adjusted latitude of 60°N as in Sanders and Gyakum (1980) consistent with the *Braer* storm undergoing EC between 55°N and 65°N. The *Braer* storm underwent its maximum 6-hour deepening rate of 26 hPa, dropping from a minimum central pressure of 962 hPa to 936 hPa in the interval from 0000 UTC to 0600 UTC on 10 January 1993 (Odell et al. 2013; Fig. 2.10). The NV19 storm underwent its maximum 6-hour deepening rate of 20 hPa, dropping from 1004 hPa to 984 hPa, from 1200 UTC to 1800 UTC on 26 November (Fig. 2.10). Indeed, a majority of this 6-hour deepening rate was accomplished in just 3 hours, as the minimum central pressure of the NV19 storm fell an astonishing 12 hPa from 1500 UTC to 1800 UTC on 26 November. Thus, the period of most rapid development was comparable between the two storms.

As noted in Odell et al. (2013), a majority of the *Braer* storm's EC occurred between Iceland and Scotland, in the open waters of the northern Atlantic Ocean. Thus, the *Braer* storm developed in a low friction environment, with no topography to create low-level flow barriers. The NV19 storm, in contrast, underwent its most rapid development in close proximity to the west coast of the United States, moving from 460 nm to within 160 nm from the coast between 1500 UTC and 1800 UTC 26 November, the better half of its maximum 6-hour deepening period. As the US west coast is extremely mountainous, frictional forces are large and so conspire to reduce the intensity of cyclogenesis by directing low-level flow away from geostrophy and towards the center of the low. The proximity of the NV19 storm to land is certainly not the only factor which would hinder the potential strength of the storm. The NV19 storm underwent EC at an average latitude which was 15° lower than that of the *Braer* storm. One can assess these latitudinal effects using the Lagrangian rate of change of absolute vorticity, expressed as

$$\frac{d\zeta}{dt} \approx -f(\nabla \cdot \vec{V}) \tag{19}$$

where ζ is the relative vorticity, f represents the planetary vorticity, and $\nabla \cdot \vec{V}$ is the divergence of the horizontal wind. A larger value of f combined with convergence in the vicinity of a low pressure, $\nabla \cdot \vec{V} < 0$, would have the tendency to increase the relative vorticity associated with the storm. The planetary vorticity associated with the NV19 storm ranged from $9.8\ x\ 10^{-5}\ s^{-1}$ to $1.1\ x\ 10^{-4}\ s^{-1}$, while the planetary vorticity associated with the Braer storm ranged from $1.2\ x\ 10^{-4}\ s^{-1}$ to $1.3\ x\ 10^{-4}\ s^{-1}$. Since the planetary vorticity associated with the NV19 storm was, on average, 18% lower than that of the *Braer* storm throughout its lifecycle, the overall time tendency of the absolute vorticity during its lifecycle was substantially reduced. Therefore, even after considering the influence of proximity to land and the reduced planetary vorticity effects, the NV19 storm still managed to achieve about 80% of the EC achieved by the strongest extratropical cyclone ever recorded achieved.

Lastly, the location of maximum deepening of this storm occurred outside of all three of the climatologies examined in R84, Wang and Rogers (2001), and ZH17, which includes data of every EC event over the north Pacific Ocean in a combined 30-year period (Fig. 2.7; Fig. 2.7.1; Fig. 2.8; Fig. 2.8.1; Fig. 2.9). As previously stated, the NV19 storm experienced its most rapid period of deepening during a 3-hour period from 1500 UTC to 1800 UTC on 26 November, in which the storm travelled from 44.5°N, 130.5°W to 43.2°N, 128°W (Figs. 2.1a-2.3a; Fig. 2.10). Both of these locations are located outside of the frequency contours of maximum deepening positions of every EC event analyzed in R84, Wang and Rogers (2001), and ZH17, with 43.2°N, 128°W being even further away from the frequency contours (Fig. 2.7.1; Fig. 2.8.1; Fig. 2.9). Thus, out of the more than 30 years of EC events analyzed in all three studies, no maximum deepening position of any EC event in the north Pacific Ocean has occurred in the location of the NV19 storm. The maximum deepening position of the NV19 storm becomes even more intriguing when one considers where this location is in reference to global ocean currents. The NV19 initially developed and rapidly intensified directly over the California current, which is the eastern component of the Central Pacific Gyre. The California current produces upwelling and cold sea surface temperatures due to Ekman suction along the west coast of the United States (Ekman 1905). This area of cold sea surface temperatures certainly would not support the type of low-level latent heat flux adjacent to the western boundary current, meaning that upward vertical motion and consequent EC events would be somewhat discouraged compared to such regions. A reduction in low-level heat flux would also suppress convection due to increased low-level stratification. Such an increase acts to lower the effects of the self-development process in which convection associated with the warm sector of a cyclone diabatically increases heights ahead of the cyclone and decreases the wavelength associated with the mid-tropospheric trough-ridge couplet associated with the cyclone (Sutcliffe and Forsdyke 1950). The NV19 storm underwent maximum deepening in a nearly unprecedented location, most likely because this is also a highly-unfavorable location, outside of all known events in studies covering a combined more than 30 years of EC events.

It is clear that the storm track, deepening rate, and location of maximum deepening of the NV19 storm were all highly unusual. The storm track was oriented roughly 90° out of phase from almost all of the tracks presented in the 12 cases of EC in the NEP identified in ZH17. Despite being situated in a region that had significantly greater friction, smaller sensible heat fluxes, and an almost 20% weaker planetary vorticity forcing, the NV19 storm managed to achieve about 80% of the maximum 6-hour EC that was achieved by the *Braer* storm. The location of maximum deepening of the NV19 storm was also outside of the R84, Wang and Rogers (2001), and ZH17 climatologies, which when combined cover a more than 30-year period of EC events, and also occurred within 500 nm of the west coast of the North American continent. In conjunction with all of the oddities of the NV19 storm, a remarkable central pressure fall of 43 hPa in 24 hours was recorded just before landfall on the California-Oregon coastline. This study aims to explain how the NV19 storm was able to set the all-time California low pressure record while developing in a rare and historically unfavorable region for EC, through the use of a QGPV inversion and QG-omega analysis. In the remainder of this thesis, any reference to intensity of location of the NV19 storm will be based on a WRF model simulation of the storm, ***not*** the GFS reanalysis of the storm.

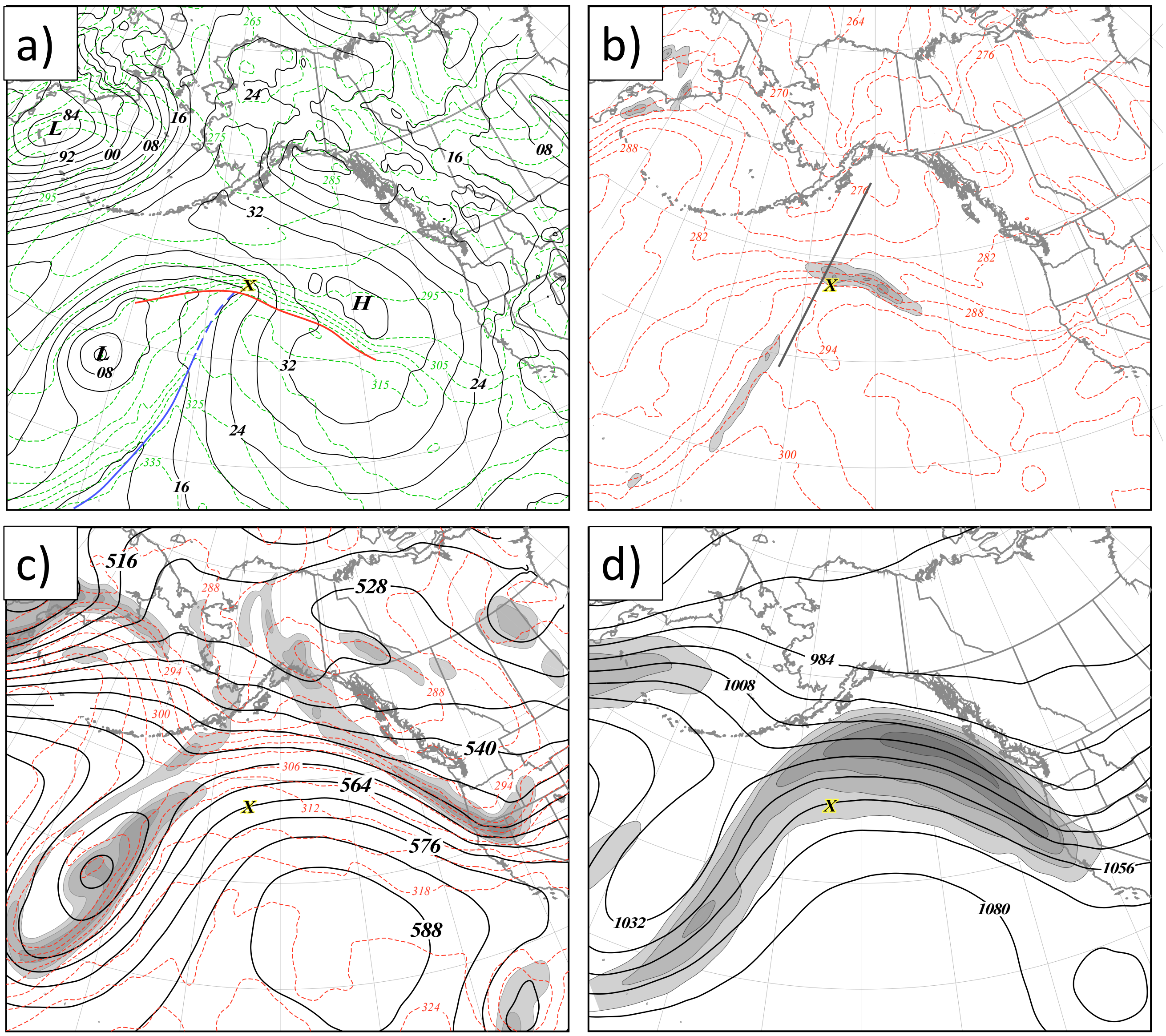

Figure 2.1. (a.) Sea-level pressure and 950 hPa equivalent potential temperature from the GFS analysis valid at 1200 UTC 25 November 2019. Solid, black lines are isobars contoured every 4 hPa starting at 1000 hPa with the leading "9" or "10" omitted. Dashed, green lines are 950 hPa moist isentropes contoured every 5 Kelvin. "H" denotes areas of localized high pressure whereas "L" denotes areas of localized low pressure. Cold and warm fronts are also analyzed. (b.) Potential temperature and positive frontogenesis at 850 hPa from the GFS analysis valid at 1200 UTC 25 November 2019. Dashed, red contours are isentropes contoured every 3 Kelvin. Shading indicates

positive frontogenesis function values shaded every $9.26\ x\ 10^{-10}$ K m^{-1} s^{-1}, or every $\frac{1\ K}{100\ km}\ \frac{1}{3\ hr}$. c.) Geopotential heights, potential temperature, and vorticity at 500 hPa from the GFS analysis valid at 1200 UTC 25 November 2019. Solid, black contours are geopotential heights contoured every 6 dm starting at 540 dm. Red, dashed contours are isentropes contoured every 3 Kelvin starting at 290 Kelvin. Shading indicates positive relative vorticity shaded every $4\ x\ 10^{-5}$ s^{-1} starting at $16\ x\ 10^{-5}$ s^{-1}. d.) Geopotential heights and wind speed at 300 hPa from the GFS analysis valid at 1200 UTC 25 November 2019. Solid, black contours are geopotential heights contoured every 12 dm starting at 1020 dm. Shading indicates wind speed shaded every 10 m s^{-1} starting at 30 m s^{-1}.

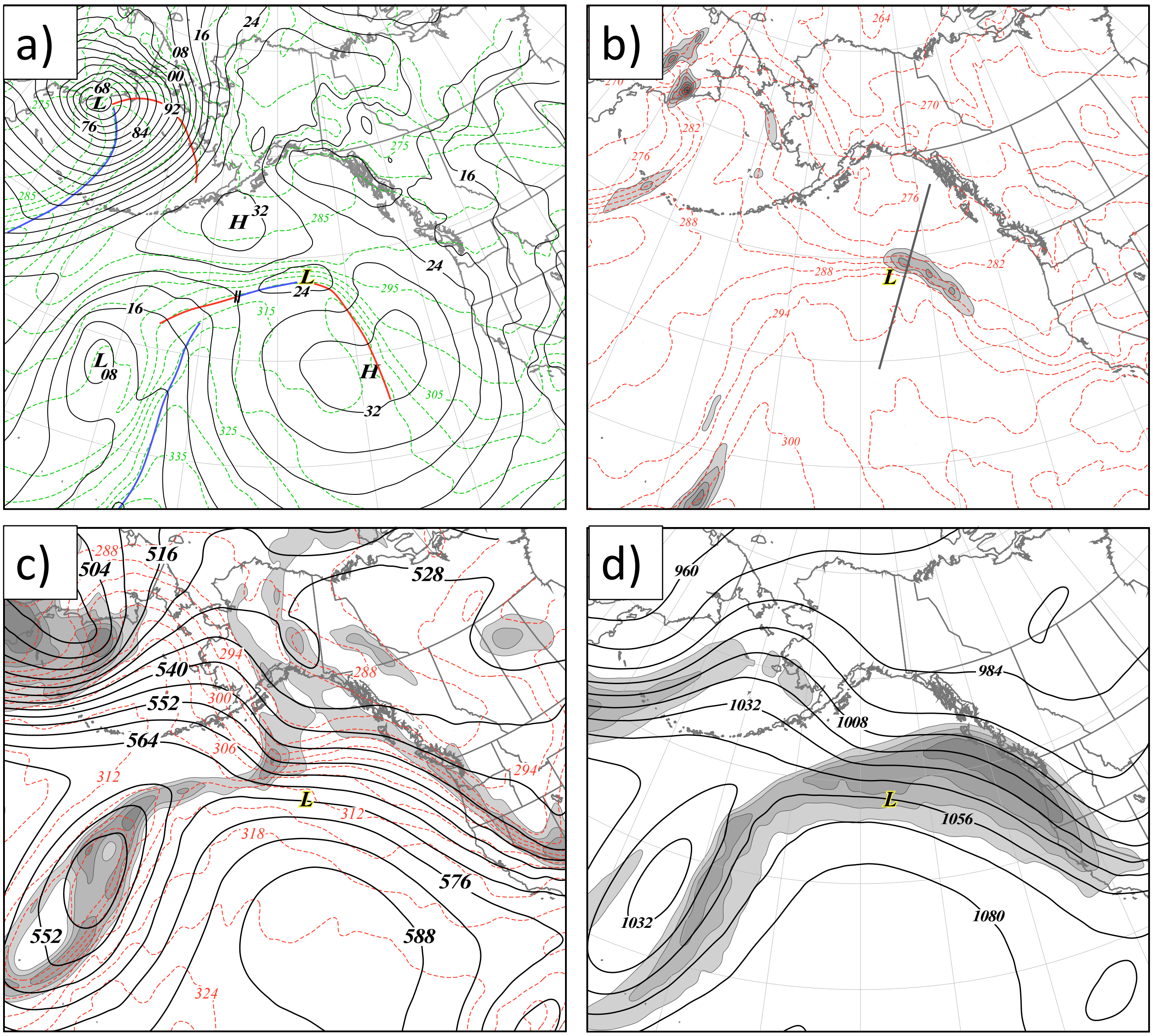

Figure 2.2. (a.) As for Fig. 2.1a except GFS analysis valid at 0000 UTC 26 November 2019. (b.) As for Fig. 2.1b except GFS analysis valid at 0000 UTC 26 November 2019. (c.) As for Fig. 2.1c except GFS analysis valid at 0000 UTC 26 November 2019. (d.) As for Fig. 2.1d except GFS analysis valid at 0000 UTC 26 November 2019.

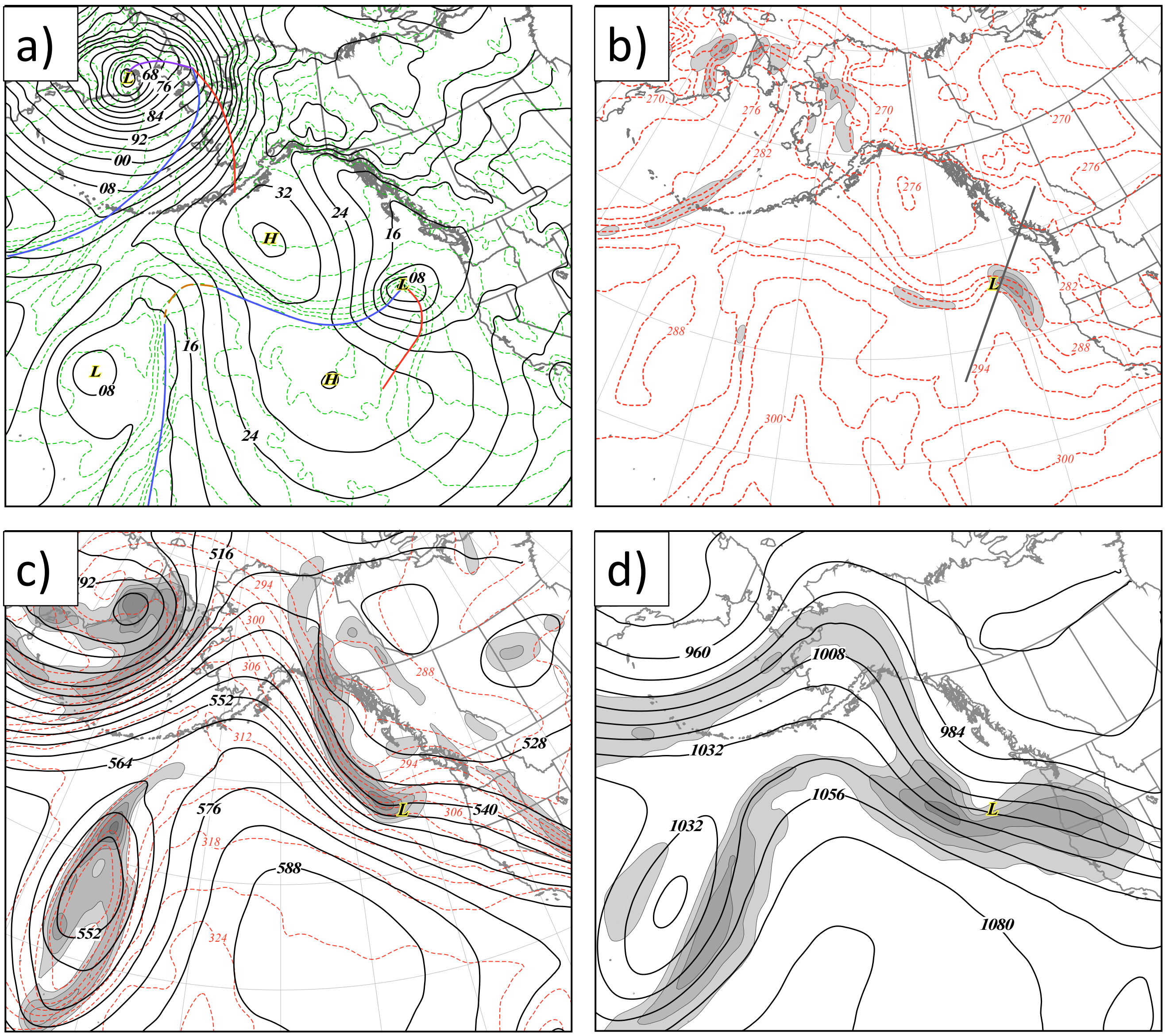

Figure 2.3. (a.) As for Fig. 2.2a except GFS analysis valid at 1200 UTC 26 November 2019. (b.) As for Fig. 2.2b except GFS analysis valid at 1200 UTC 26 November 2019. (c.) As for Fig. 2.2c except GFS analysis valid at 1200 UTC 26 November 2019. (d.) As for Fig. 2.2d except GFS analysis valid at 1200 UTC 26 November 2019.

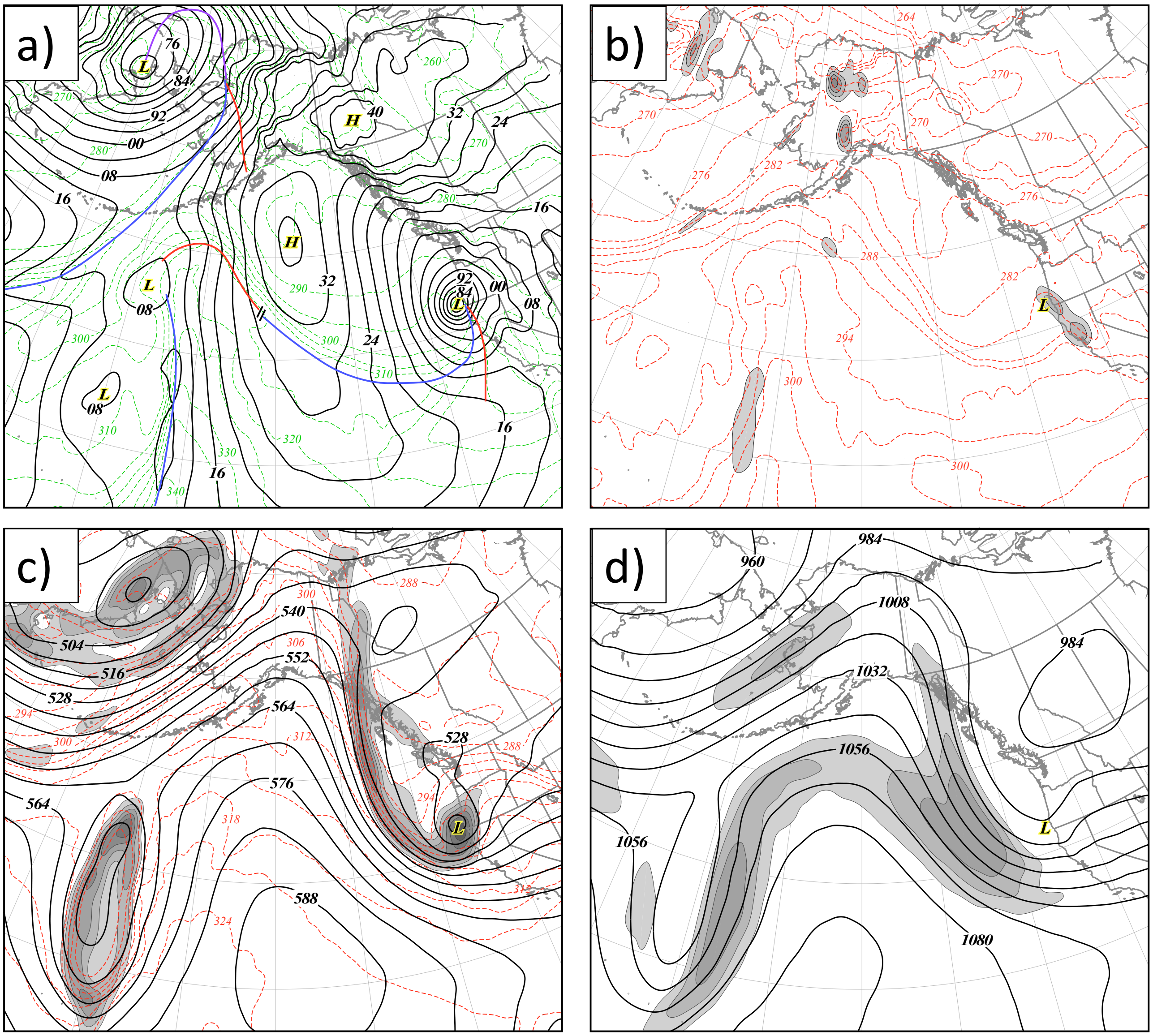

Figure 2.4. (a.) As for Fig. 2.3a except GFS analysis valid at 0000 UTC 27 November 2019. (b.) As for Fig. 2.3b except GFS analysis valid at 0000 UTC 27 November 2019. (c.) As for Fig. 2.3c except GFS analysis valid at 0000 UTC 27 November 2019. (d.) As for Fig. 2.3d except GFS analysis valid at 0000 UTC 27 November 2019.

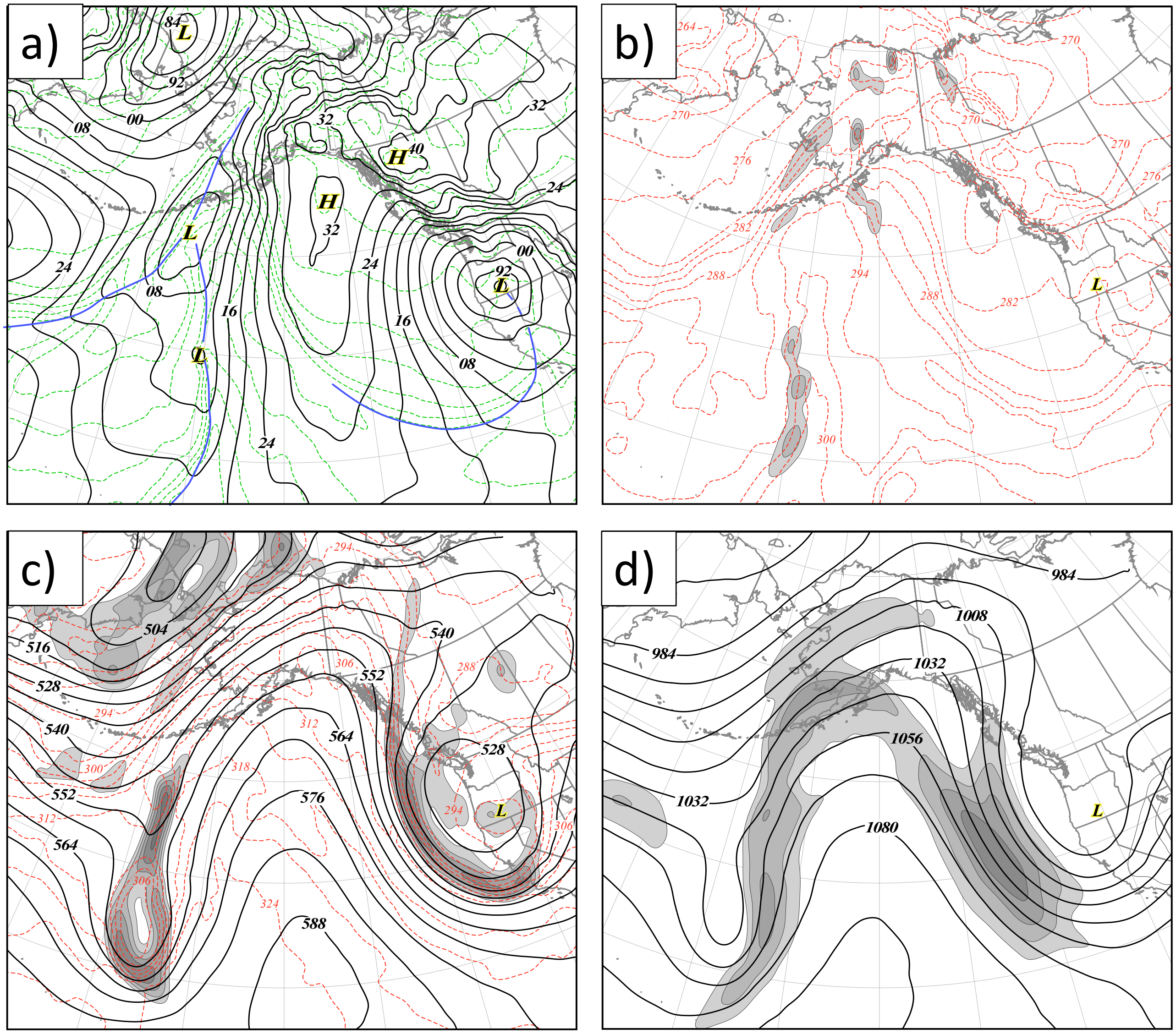

Figure 2.5. (a.) As for Fig. 2.4a except GFS analysis valid at 1200 UTC 27 November 2019. (b.) As for Fig. 2.4b except GFS analysis valid at 1200 UTC 27 November 2019. (c.) As for Fig. 2.4c except GFS analysis valid at 1200 UTC 27 November 2019. (d.) As for Fig. 2.4d except GFS analysis valid at 1200 UTC 27 November 2019.

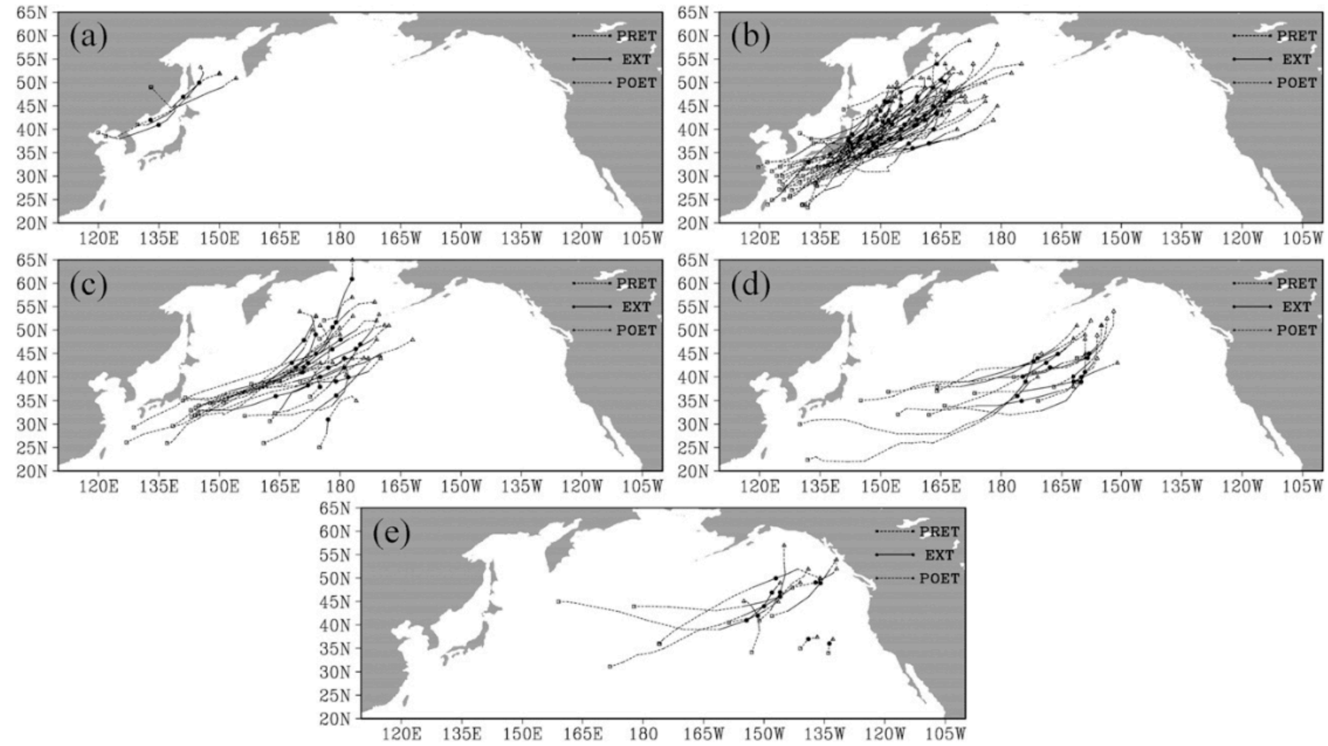

Figure 2.6. Adopted from Zhang et al. (2017). The storm tracks of strong (1.70 to 2.29 Bergerons) cyclones for the a) Japan-Okhotsk Sea, b) the northwestern Pacific Ocean, c) the west-central Pacific Ocean, d) the east-central Pacific Ocean, and e) the northeastern Pacific Ocean. Dashed lines with open squares indicate the pre-explosive deepening lifetime phase (PRET), solid lines with filled circles indicate the explosive deepening lifetime phase (EXT), and dashed lines with open triangles indicate the post-explosive deepening lifetime phase (POET).

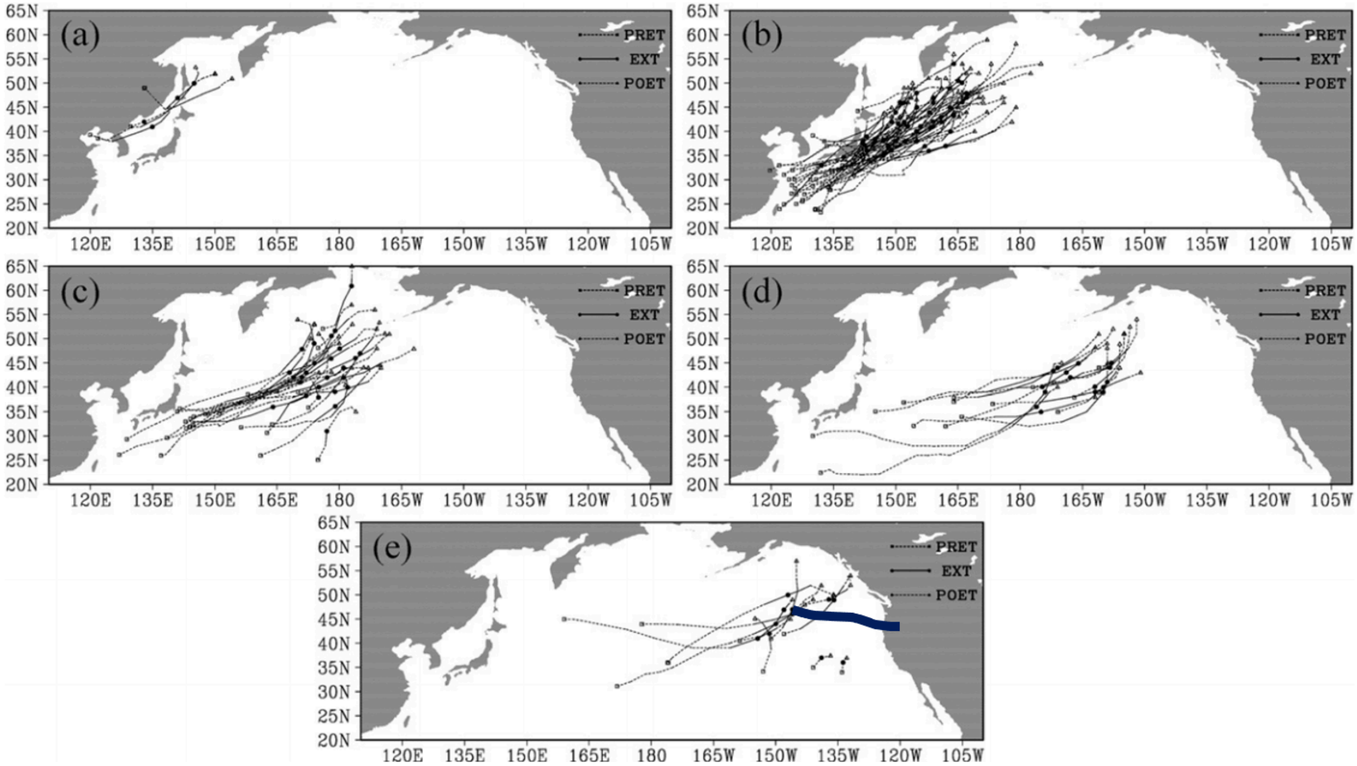

Figure 2.6.1. Adopted from Zhang et al. (2017). a) – d) as in Fig. 2.6. e) As in Fig. 2.6 but with a solid, navy blue line which indicates approximate track of the November 2019 storm based on GFS analysis data.

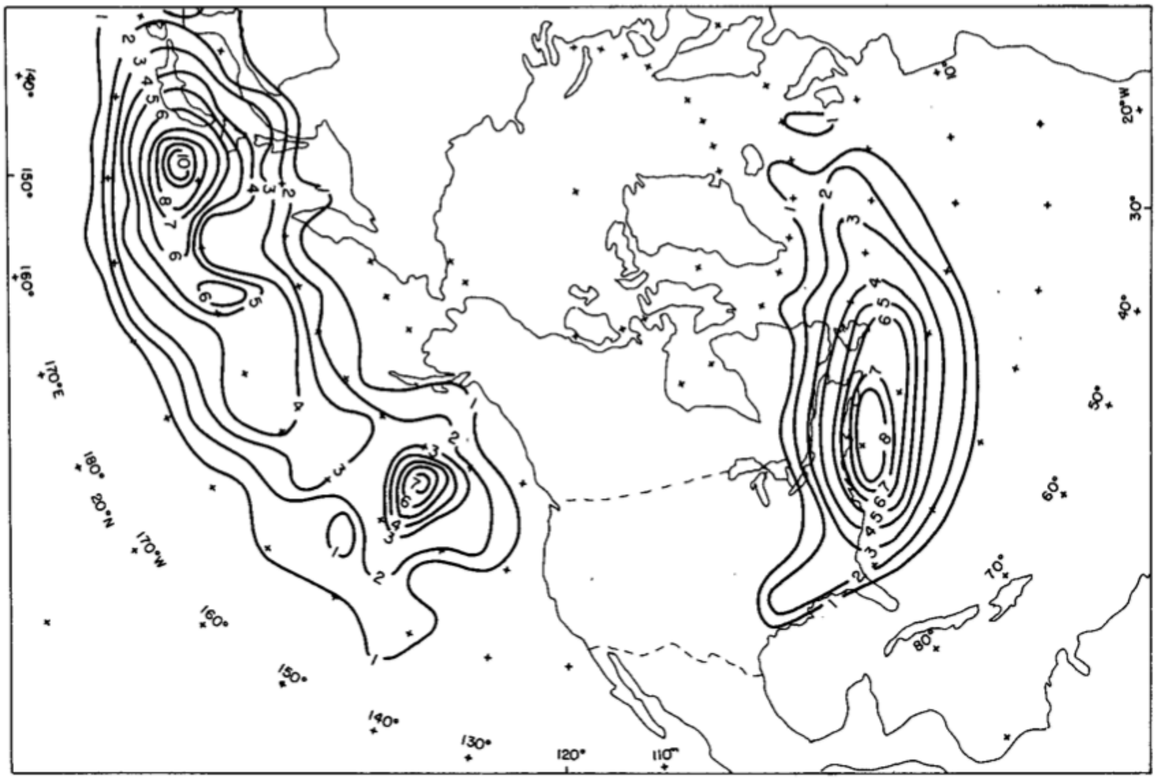

Figure 2.7. Adopted from Roebber (1984). Geographical distribution of maximum deepening positions for 1976 - 1982 1200 GMT – 1200 GMT bomb cyclones.

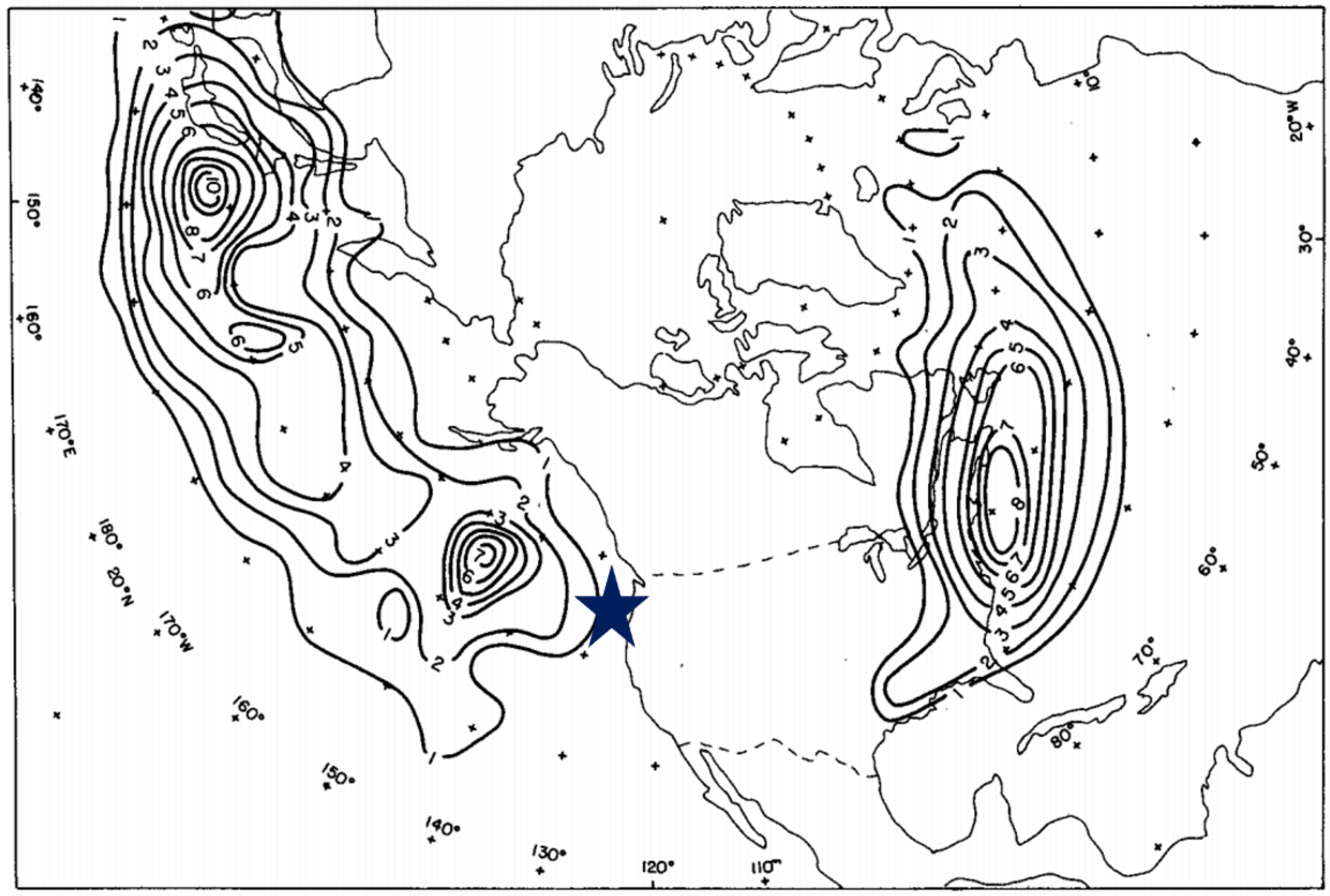

Figure 2.7.1. Adopted from Roebber (1984). As in Fig. 2.7 but with a navy blue star which indicates maximum deepening position of the November 2019 storm based on GFS analysis data

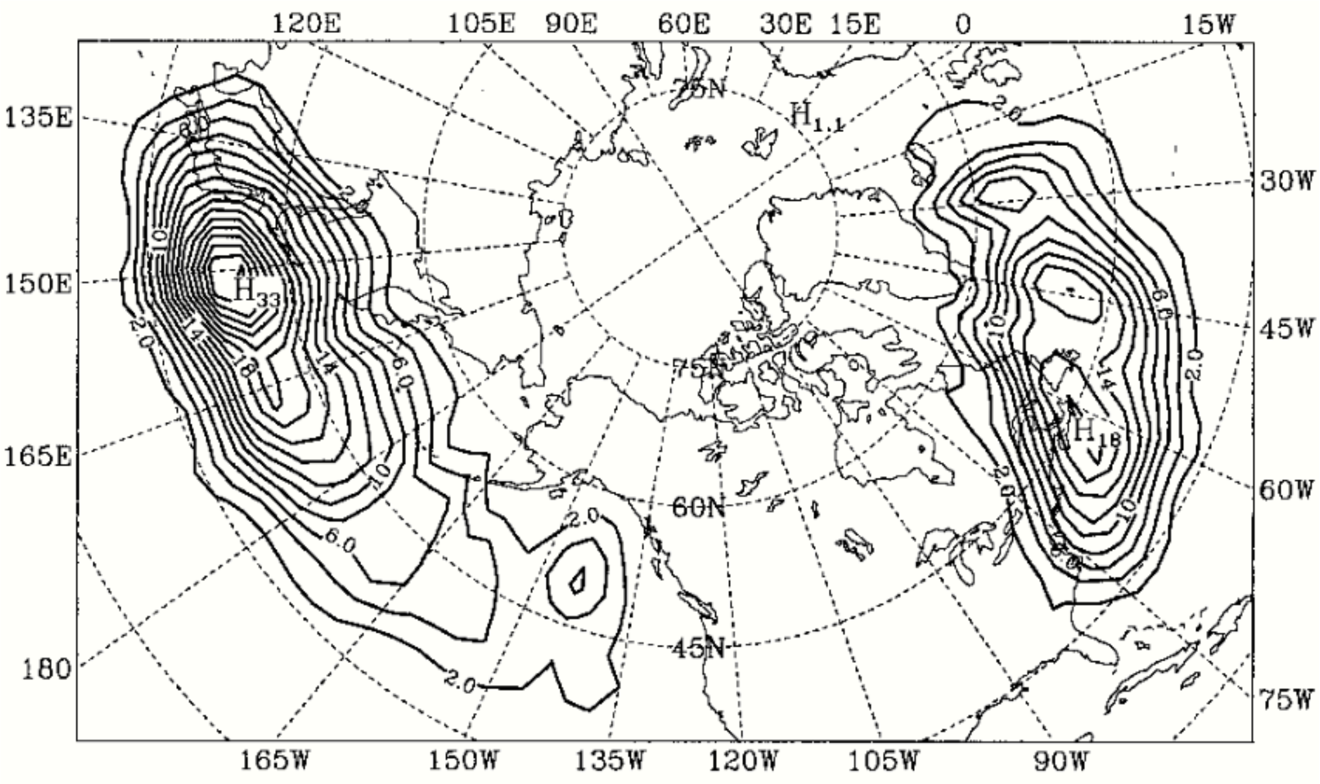

Figure 2.8. Adopted from Wang and Rogers (2001). Geographic distribution of 24-hour explosive cyclogenesis in the Northern Hemisphere derived from ECMWF MSLP data from January 1985 to March 1996. Numbers are first counted at 2.5º resolution and aggregated into 5º × 5º quadrilaterals by adding them together. Then, a smoothing method of 0.5 times the frequency at the central point plus 0.125 times the sum of the frequencies at four adjacent points is applied.

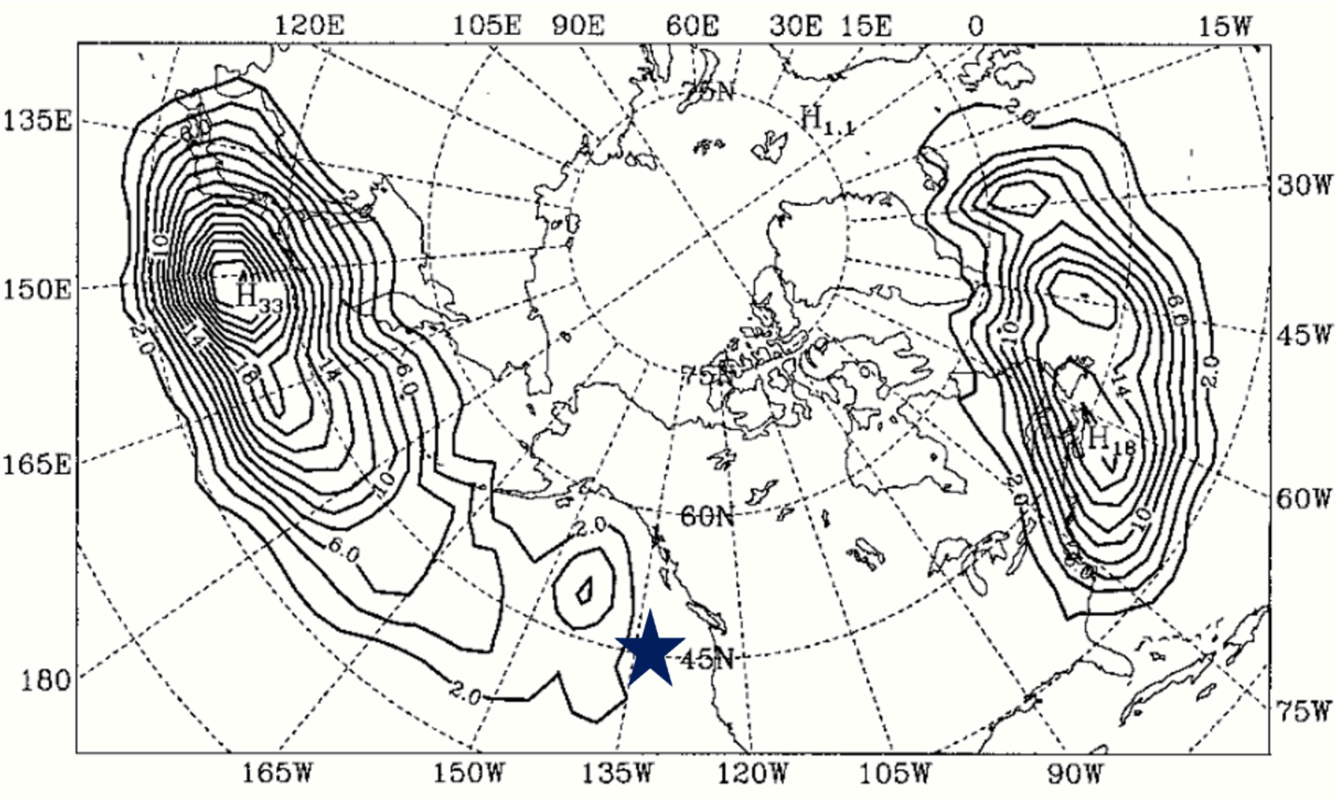

Figure 2.8.1. Adopted from Wang and Rogers (2001). As in Fig. 2.8 but with a navy blue star which indicates average location of the November 2019 storm based on GFS analysis data

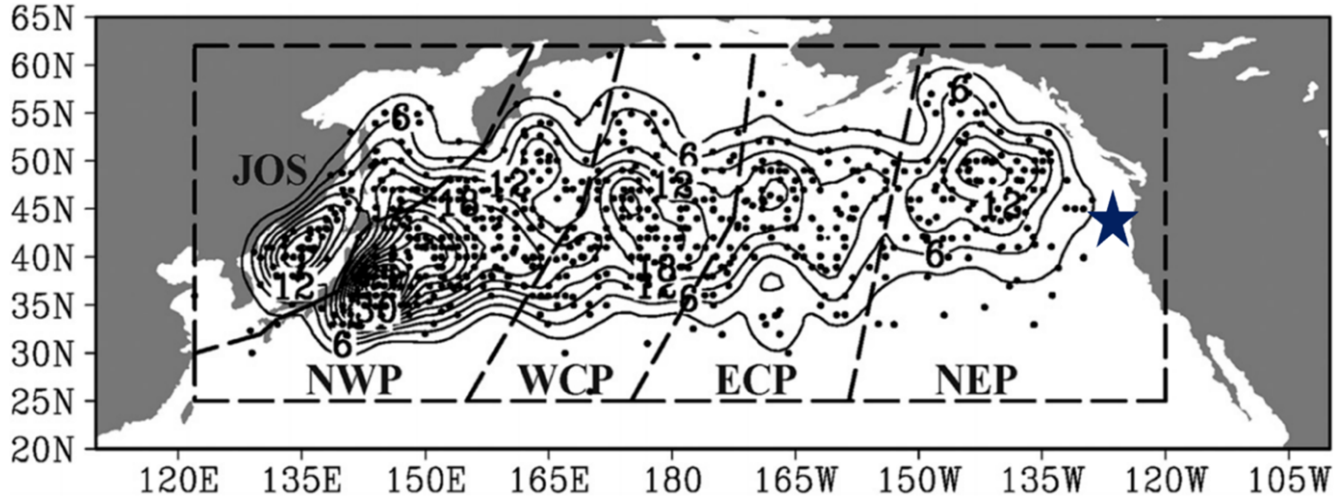

Figure 2.9. Adopted from Zhang et al. (2017). The smoothed frequency (thin contours, contour interval = 3) of maximum deepening positions (MDPs) (dots) for all explosive cyclogenesis (EC) events. The boundaries of ECs for distinguishing the various regions are drawn with a thick dashed line. Navy blue star indicates location of MDP for the November 2019 storm.

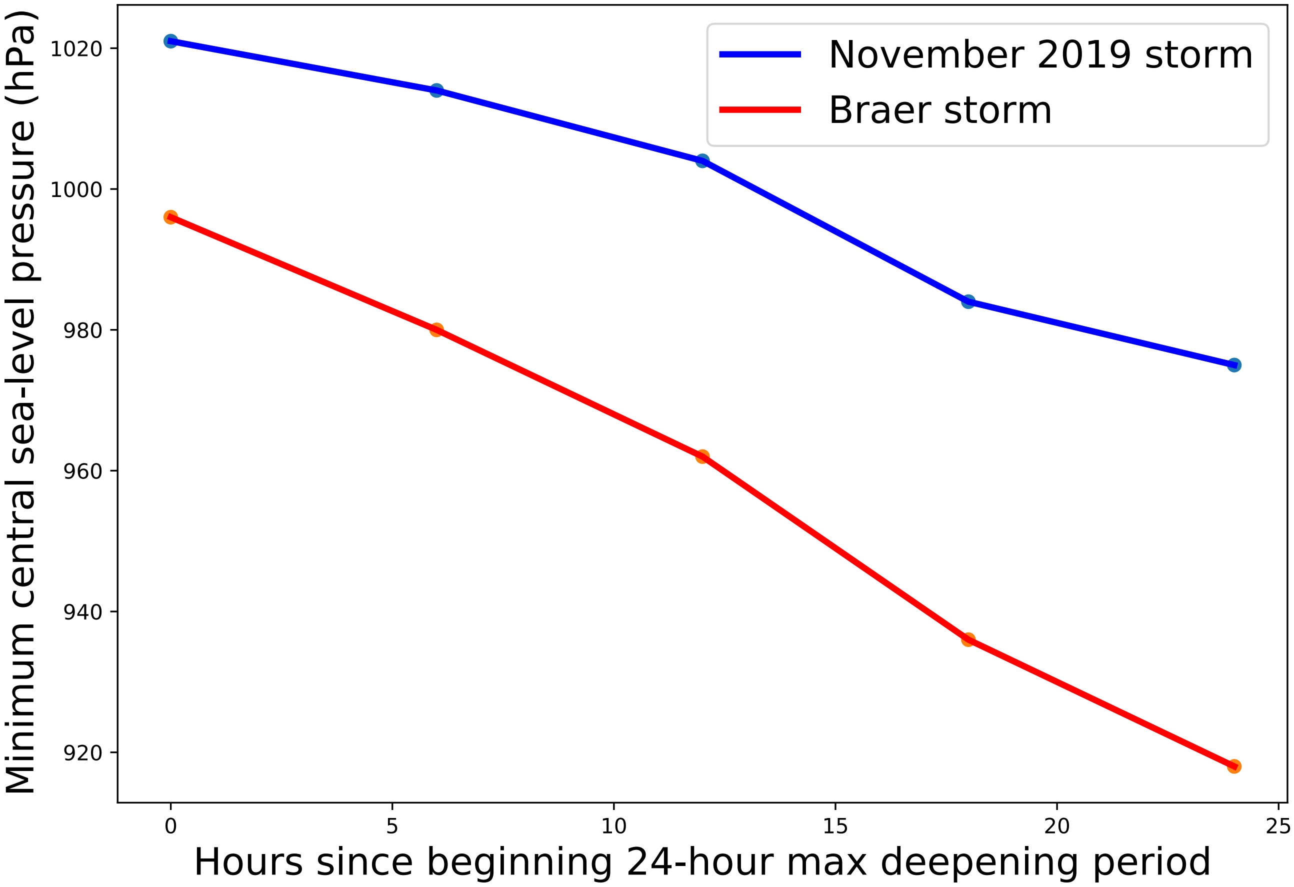

Figure 2.10. 6-hourly sea-level pressure deepening rates from the November 2019 storm compared to the *Braer* storm at the location of the central sea-level pressure minimum from the 24-hour period of most rapid deepening. 6-hourly deepening rates are plotted in hectopascals with the blue contour representing the November 2019 storm and the red contour representing the *Braer* storm.

3. METHODOLOGY

3.1 Weather Research and Forecasting (WRF) Model

The WRF Model Version 4.1.4 is used to simulate the lifecycle of the NV19 storm (http://www.wrf-model.org; Skamarock et al. 2019). The WRF simulation covers a 60-hour period beginning at 1200 UTC 25 November 2019 and ending at 0000 UTC 28 November 2019, with a horizontal grid spacing of 30 km and output available every three hours. The model domain is composed of 30 km grid spacing with 198 grid boxes in the south-north direction, 218 grid boxes in the west-east direction, and 33 vertical terrain-following eta levels (Fig. 3.1). Initial and boundary conditions were provided by the six-hourly Global Forecast System (GFS) reanalysis data at 0.25° latitude-longitude resolution. As was noted in Chapter 2, the true NV19 storm, along with the simulation of the NV19 storm, started on an initially completely eastward track and then began to track southeastward as it approached the United States west coast (Fig. 3.2; Fig. 3.3). The simulated storm track agreed with the observed storm track while capturing the extreme 40+ hPa in 24 hours deepening rate from 0000 UTC 26 November to 0000 UTC 27 November (Fig. 3.2).

The following physical parameterizations were chosen for the WRF simulation: (i) the Thompson Scheme for microphysics parameterization (Thompson et al. 2008), (ii) the Tiedtke Scheme for cumulus parameterization (Tiedtke 1989), (iii) the Mellor-Yamada-Janjic Scheme for planetary boundary layer physics (Janjic 1994), (iv) the Noah Land Surface Model for land-surface physics, which is based off of the OSU Land Surface Model (Chen and Dudhia 2001), (v) the Monin-Obukhov Similarity scheme for surface-layer physics (Monin and Obukhov 1954), and (vi) the Rapid Radiative Transfer Model for shortwave and longwave radiation physics (Iacono et al. 2008). These parameterizations are encompassed in the “CONUS” physics suite which is included in a string of updates to the WRF model version 3 (Skamarock et all. 2008). As noted by the WRF-model developer, the “CONUS” physics suite consists of a combination of highly-tested and reasonable options which are applicable to surface, near-surface, and upper air conditions anywhere across, and adjacent to, the contiguous United States, which is applicable to the majority of the simulation analysis period (http://www.wrf-model.org; Skamarock et al. 2019).

3.2 Data Processing

Data from the WRF model simulation of the NV19 is outputted into NetCDF format (Rew et al. 1990), which allows for manipulation of the NetCDF file using a Python package called “wrf-python” (Ladwig 2017). Such manipulations include extracting variables with specified units from the NetCDF file, interpolation to defined isobaric or isentropic levels, and defining a vertical plane in which cross sections can be drawn. The atmospheric static stability is a crucial variable to both cyclogenesis events and successful QGPV inversion and must, therefore, be calculated from the WRF model simulation output. After extracting the necessary variables and interpolating them to 19 isobaric levels ranging from 1000 hPa to 100 hPa at 50 hPa increments the spatial and temporally-averaged static stability is calculated and shown to be close to, but not exactly, equal to the US standard atmosphere static stability (Minzner 1977; Fig. 3.4). The US standard atmosphere is a static model of the atmosphere extending from the lower troposphere into the upper thermosphere. This model provides an international standard for how variables such as temperature and density vary throughout the extent of Earth’s atmosphere, if Earth’s atmosphere were to follow this idealized state. It is then trivial for the atmospheric conditions included in studies using the US standard atmosphere to be recreated, making studies more universally applicable. Since the WRF stability is specific to the simulation itself and because it bears a close resemblance to the US standard atmosphere, it will be used in the PV diagnostics in this study. Notable differences in the two static stabilities occur from 800 hPa to 700 hPa and from 300 hPa to 200 hPa (Fig. 3.4), however, these differences do not significantly impact the QGPV inversion results (not shown).

3.3 QGPV Inversion

The QGPV is defined as in equation (17) by

$$q_g = \frac{1}{f_0}\nabla^2\phi + f + f_0\frac{\partial}{\partial p}\left(\frac{1}{\sigma}\frac{\partial \phi}{\partial p}\right).$$

It can be shown that the geostrophic time rate of change of QGPV is equal to zero, meaning that the QGPV is conserved following adiabatic, geostrophic flow (Charney and Stern 1962). This conservation statement represents the first of two key characteristics which make the (QG)PV an important tool for diagnosing EC events, with the second being that the QGPV is invertible given specific criteria.

The QGPV is calculated term by term based on the expression above. From this distribution of QGPV, the time mean over a 60-hour interval is taken and anomalies from the QGPV time mean, deemed QGPV perturbations (QGPVP), are computed at 3-hour intervals across the WRF model simulation domain (Fig. 3.1). As there are no anomalies to the Coriolis parameter, f, which is dependent on latitude and rotation rate only, the QGPVP are only dependent on the strength of the geostrophic relative vorticity and vertical adiabatic stretching. Equation (17) now becomes

$$q_* = \frac{1}{f_0}\nabla^2\phi' + f_0\frac{\partial}{\partial p}\left(\frac{1}{\sigma}\frac{\partial\phi'}{\partial p}\right), \tag{20}$$

where $q_* = {q_g}' - f$, q_* is the perturbation QGPV, $\frac{1}{f_0}\nabla^2\phi'$ is the perturbation geostrophic relative vorticity, and $f_0\frac{\partial}{\partial p}\left(\frac{1}{\sigma}\frac{\partial\phi\prime}{\partial p}\right)$ is the vorticity attributed to the vertical derivative of the perturbation temperature and static stability. Along with the QGPVP, the bottom and top isobaric-level perturbation potential temperatures are calculated using the hydrostatic assumption and Ideal Gas Law in order to account for boundary-level potential temperature anomalies in the inversion of the QGPVP:

$$\frac{RT'}{p} = -\frac{\partial\phi'}{\partial p} \tag{21}$$

$$T' = -\frac{p}{R}\frac{\partial\phi'}{\partial p} \tag{22}$$

$$\theta' = -\frac{p}{R}\left(\frac{p_0}{p}\right)^{\frac{R}{c_p}}\frac{\partial\phi'}{\partial p} \tag{23}$$

where R is the dry gas constant, ϕ' is the perturbation geopotential, T' is the perturbation boundary temperature and p_0 is a reference pressure, typically taken as 1000 hPa.

Following methods outlined in Hoskins et al. (1985) and Hakim et al. (1996), as noted earlier, the expression for the QGPV in isobaric coordinates can be expressed as in equation (17). If we define a linear operator to be applied to a distribution of geopotential as explained in Morgan and Nielsen-Gammon (1998), equation (20) can be rewritten as

$$q_* = \mathcal{L}(\phi'), \tag{24}$$

where the operator $\mathcal{L}$ is defined as

$$\mathcal{L} = \frac{1}{f_0}\nabla^2 + f_0\frac{\partial}{\partial p}\left(\frac{1}{\sigma}\frac{\partial}{\partial p}\right). \tag{25}$$

For any flavor of partitioning of the QGPV field, q_{*i}, the partition-constrained perturbation geopotential, ${\phi_i}'$, associated with the distribution of QGPV can be determined by applying the inverse of the linear operator to equation (24), which yields

$${\phi_i}' = \mathcal{L}^{-1}(q_{*i}). \tag{26}$$

As emphasized in Hakim et al. (1996), equation (26) is only valid if the sum of the partitioned perturbation QGPV and geopotential fields is equal to the total partitioned perturbation QGPV and geopotential fields. Equation (26) is solved using successive over-relaxation techniques to obtain the partitioned perturbation geopotential field with a residual error that is less than an arbitrarily-chosen value of 10^{-2} (Engeli et al. 1959; Carré 1961; Hoskins et al. 1985; Hakim et al. 1996; Morgan 1999; Martin and Marsili 2002). It is the geopotential height distribution associated with the anomalies which is of interest to this thesis, as it is presumed that certain PV anomalies in the upper troposphere will be of sufficient magnitude that their associated geopotential height field will extend well below the level of the anomaly and affect a cyclogenesis event in the lower troposphere (Fig. 3.5). Upon solving for a distribution of the partitioned perturbation geopotential field, the geostrophic winds (at any level) associated with that QGPVP can be determined using fundamental relationships and, from those winds, it is possible to determine how each partitioned layer is acting to advect QGPV throughout the domain of interest. This determination allows for the otherwise diagnostic technique of piecewise (QG)PV inversion to become a prognostic technique using the advection of (QG)PV from the static piecewise inversion of (QG)PV (Hakim et al. 1996). Also, hitherto, any mention of QGPV inversion is referring to the inversion of *perturbations* of the QGPV, not the full QGPV. Therefore, the inversion process is being applied to a distribution of QGPV perturbations but will be referred to as QGPV inversion.

An important aspect of the derivation from equation (4) to equation (17) is that the diabatic heating term in the QG thermodynamic energy equation is neglected. If one were to carry out a similar derivation while keeping the diabatic heating term, equation (9) would become

$$f_0\frac{\partial \omega}{\partial p}=\frac{\partial}{\partial p}\left(\frac{f_0}{\sigma}\frac{\partial \chi}{\partial p}\right)+\frac{\partial}{\partial p}\left[\frac{f_0}{\sigma}\vec{V}_g\cdot\nabla\left(\frac{\partial \phi}{\partial p}\right)\right]+f_0\frac{\partial}{\partial p}\left[\frac{R\dot{Q}}{\sigma p c_p}\right] \tag{27}$$

where the term in red represents the influences of diabatic heating. If we carry this diabatic heating term through the derivation of the QGPV as presented in Chapter 1, equation (12) becomes

$$\left(\frac{1}{f_0}\nabla^2\chi\right)=-\vec{V}_g\cdot\nabla\left(\frac{1}{f_0}\nabla^2\phi+f\right)-\frac{\partial}{\partial p}\left[\frac{f_0}{\sigma}\vec{V}_g\cdot\nabla\left(-\frac{\partial \phi}{\partial p}\right)\right]+\frac{\partial}{\partial p}\left(\frac{f_0}{\sigma}\frac{\partial \chi}{\partial p}\right)+f_0\frac{\partial}{\partial p}\left[\frac{R\dot{Q}}{\sigma p c_p}\right] \tag{28}$$

and equation (13) becomes

$$\left[\frac{1}{f_0}\nabla^2+\frac{\partial}{\partial p}\left(\frac{f_0}{\sigma}\frac{\partial}{\partial p}\right)\right]\chi=-\vec{V}_g\cdot\nabla\left(\frac{1}{f_0}\nabla^2\phi+f\right)-\frac{\partial}{\partial p}\left[\frac{f_0}{\sigma}\vec{V}_g\cdot\nabla\left(-\frac{\partial \phi}{\partial p}\right)\right]+f_0\frac{\partial}{\partial p}\left[\frac{R\dot{Q}}{\sigma p c_p}\right]. \tag{29}$$

Using equation (8) to rewrite the second term on the right hand side of the equation and again noting that the thermal wind is parallel to isotherms, equation (29) becomes

$$\frac{\partial}{\partial t}\left[\nabla^2\phi+\frac{\partial}{\partial p}\left(\frac{f_0}{\sigma}\frac{\partial \phi}{\partial p}\right)\right]=-\vec{V}_g\cdot\nabla\left(\frac{1}{f_0}\nabla^2\phi+f+f_0\frac{\partial}{\partial p}\left(\frac{1}{\sigma}\frac{\partial \phi}{\partial p}\right)\right)+f_0\frac{\partial}{\partial p}\left[\frac{R\dot{Q}}{\sigma p c_p}\right]. \tag{30}$$

and we reach the final solution for the QGPV with an added diabatic term

$$\frac{\partial}{\partial t}\left(\frac{1}{f_0}\nabla^2\phi+f+f_0\frac{\partial}{\partial p}\left(\frac{1}{\sigma}\frac{\partial \phi}{\partial p}\right)\right)=-\vec{V}_g\cdot\nabla\left(\frac{1}{f_0}\nabla^2\phi+f+f_0\frac{\partial}{\partial p}\left(\frac{1}{\sigma}\frac{\partial \phi}{\partial p}\right)\right)+f_0\frac{\partial}{\partial p}\left[\frac{R\dot{Q}}{\sigma p c_p}\right]. \tag{31}$$

By isolating the first and last terms in equation (31), the effects of vertical gradients in diabatic heating can be related to the Laplacian of height tendency. After converting from this height tendency to heights by multiplying by the specified time step, the inversion of this QGPV with diabatic heating included can be compared to the inversion of pure QGPV to assess the effects that the diabatic heating is having on near-surface development. Thus, the final term in equation (31) will be calculated for all times and levels in the WRF-model domain and inverted, and the inverted heights from this diabatic heating term will be compared to the inverted heights from the distribution of pure QGPV.

Reiterating the overview of QGPV and its inversion as mentioned in Chapter 1, the wealth of information gained from inverting a distribution of QGPV directly relates how the QGPV associated with structures and processes in the lower- to upper-troposphere affect cyclogenesis at the surface. Information regarding basic state variables such as potential temperature, static stability, and geopotential are all by-products of inverting QGPV, which owe their existence to the invertibility principle of QGPV. This invertibility principle provides the QGPV inversion a means of associating cyclogenetic processes to user-constrained layers of the atmosphere (Hakim et al. 1996). There is no one unique way to partition the distribution of QGPV as of the publication of this thesis. Davis (1992a) provides a detailed evaluation of different partitioning methods and their limitations to a distribution of Ertel PV, but the same partitioning techniques can be extended to a distribution of QGPV. Three different partitioned layers are used in this thesis: “SPERT”, which includes QGPV from 1000 hPa to 850 hPa and includes the bottom potential temperature anomaly, “MPERT”, which includes QGPV from 800 hPa to 500 hPa and “UPERT”, which includes QGPV from 450 hPa to 100 hPa. The partitioning is such that SPERT isolates boundary-layer QGPV and potential temperature anomalies, with the potential temperature anomalies being equivalent to QGPV anomalies just above the surface (Hakim et al. 1996), MPERT isolates mid-tropospheric QGPV anomalies, and UPERT isolates QGPV anomalies associated with tropopause undulations. Through this partition, it is possible to ascertain how each layer contributes to the lower tropospheric development of the NV19 storm.

Along with vertical partitioning of the QGPV, the user must also prescribe boundary conditions during QGPV inversion which either permit or prohibit the effects of boundary-level thermal anomalies to influence the solution within the domain. The traditional boundary conditions for the inversion of a partitioned QGPV distribution consist of potential temperature on the top and bottom boundaries, which derive themselves from the Eady problem of baroclinic development where (QG)PV anomalies at the dynamical tropopause and the surface mutually amplify upon becoming phase locked (Hoskins et al.

1985). This specific boundary condition assumes a separation between the top and bottom potential temperature perturbations and interior (QG)PV anomalies such that mutual amplification is theoretically possible (Hakim et al. 1996). In this thesis, for the inversion of the full-column QGPV and the SPERT partitioned layer, potential temperature perturbations are included at the bottom level of the WRF model domain. Top level potential temperature perturbations are neglected due to their negligible contribution to surface development (not shown).

One might question the utility of employing the QGPV to diagnose dynamical processes affecting surface cyclogenesis, given that QGPV is derived under a set of assumptions tailored for low Rossby number, frictionless, adiabatic flow. Such concerns are legitimate; however, as noted in Davis (1992b), particularly for situations with large Rossby number, useful information is still gained through employing QGPV inversion ***if*** the QGPV field is reasonably well-correlated with the Ertel PV (EPV) field. For the case of the NV19 storm, the EPV field agrees well with the QGPV field (Fig. 3.6), and so QGPV inversion is likely to produce meaningful results. Hakim et al. (1996) mentioned that, despite the potentially limiting assumptions made in deriving the QGPV, an inversion of QGPV allows one to gain accurate insight into the impact of different dynamical processes on the development of a system without sacrificing simplicity or increasing computational overhead by inverting the full PV. Therefore, despite the limiting QG assumptions, we can confidently employ the inversion of QGPV in order to gain physical insight into the development of the NV19 storm.

3.4 Integrated QG Mass Divergence and Near-Surface Pressure Tendency

The usefulness of the basic state variables approach is such that direct model output variables can all be considered simultaneously in order to diagnose potential regions of vertical motion, divergence, and surface pressure falls. One of these variables, represented by the lower-case Greek letter omega, represents a direct assessment of vertical mass flux times the acceleration due to gravity and can describe how net mass transfer is occurring in columns throughout the atmosphere in the vicinity of a developing cyclone. This approach utilizes the very simple idea that greater mass divergence at the top of a column than near the surface results in rising motion, surface pressure falls, and cyclogenesis, which is incorporated in the revolutionary Sutcliffe development theorem (Sutcliffe 1947). The isobaric mass continuity is expressed as

$$\frac{\partial u}{\partial x}+\frac{\partial v}{\partial y}+\frac{\partial \omega}{\partial p}=0 \tag{32}$$

where omega is defined as the Lagrangian rate of change of pressure,

$$\omega=\frac{dp}{dt}. \tag{33}$$

Noting that $\frac{\partial u}{\partial x}+\frac{\partial v}{\partial y}$ is the horizontal divergence of the wind, equation (32) can be rewritten as

$$\nabla \cdot V+\frac{\partial \omega}{\partial p}=0. \tag{34}$$

Vertical integration equation (34) from the surface to the top of the atmosphere results in

$$\omega_{p_{sfc}}=-\int_{0}^{p_{sfc}}(\nabla \cdot V)\,\partial p=\frac{dp_{sfc}}{dt} \tag{35}$$

where

$$\frac{dp_{sfc}}{dt}=\frac{\partial p_{sfc}}{\partial t}+V_{as}\cdot \nabla p_{sfc}+w_s\frac{\partial p}{\partial z} \tag{36}$$

and $V_{as}\cdot \nabla p_{sfc}$ is the advection of the surface pressure by the ageostrophic wind at the surface, V_{as}, also known as the cross-isobaric flow. If we neglect this cross-isobaric flow and assume no-slip conditions at the surface, equation (36) reduces to

$$\frac{\partial p_{sfc}}{\partial t}=-\int_{0}^{p_{sfc}}(\nabla \cdot V)\,\partial p\,. \tag{37}$$

We are forced to curtail the integration bounds to be between 100 and 950 hPa, as separate calculations of QG-omega are similarly constrained. Thus, the contribution of integrated mass divergence in the 100 to 950 hPa portion of the column, accomplished by the QG-omega, is formally expressed as

$$\frac{\partial p_{sfc}}{\partial t}\approx-\int_{100}^{950}(\nabla \cdot V)\,\partial p=\int_{100}^{950}\frac{\partial \omega}{\partial p}\partial p \tag{38}$$

where $\frac{\partial \omega}{\partial p}$ is calculated for each 50 hPa layer from 975 hPa to 75 hPa employing QG-omega at 50 hPa increments from 1000 hPa to 50 hPa. The resulting value will be an overestimate of the instantaneous pressure tendency at the bottom of the column mostly because the effect of cross-isobar flow in the boundary layer is completely ignored and *always* contributes to mass accumulation (and pressure rises). Effects of QG-omega on near-surface pressure tendencies from 100 hPa to the top of the atmosphere layer are also neglected; however, these are assumed to be small. Nonetheless, the calculation allows for valid *comparisons* to be made amongst QG-omega in different isobaric layers and their respective influences on surface development. Vertical partitioning of the forcing for QG-omega (and subsequent independent, height attributable pieces of QG-omega) also allow the respective roles of various isobaric layers on near surface development to be isolated and compared following the same partitioning of UPERT, MPERT, and SPERT.

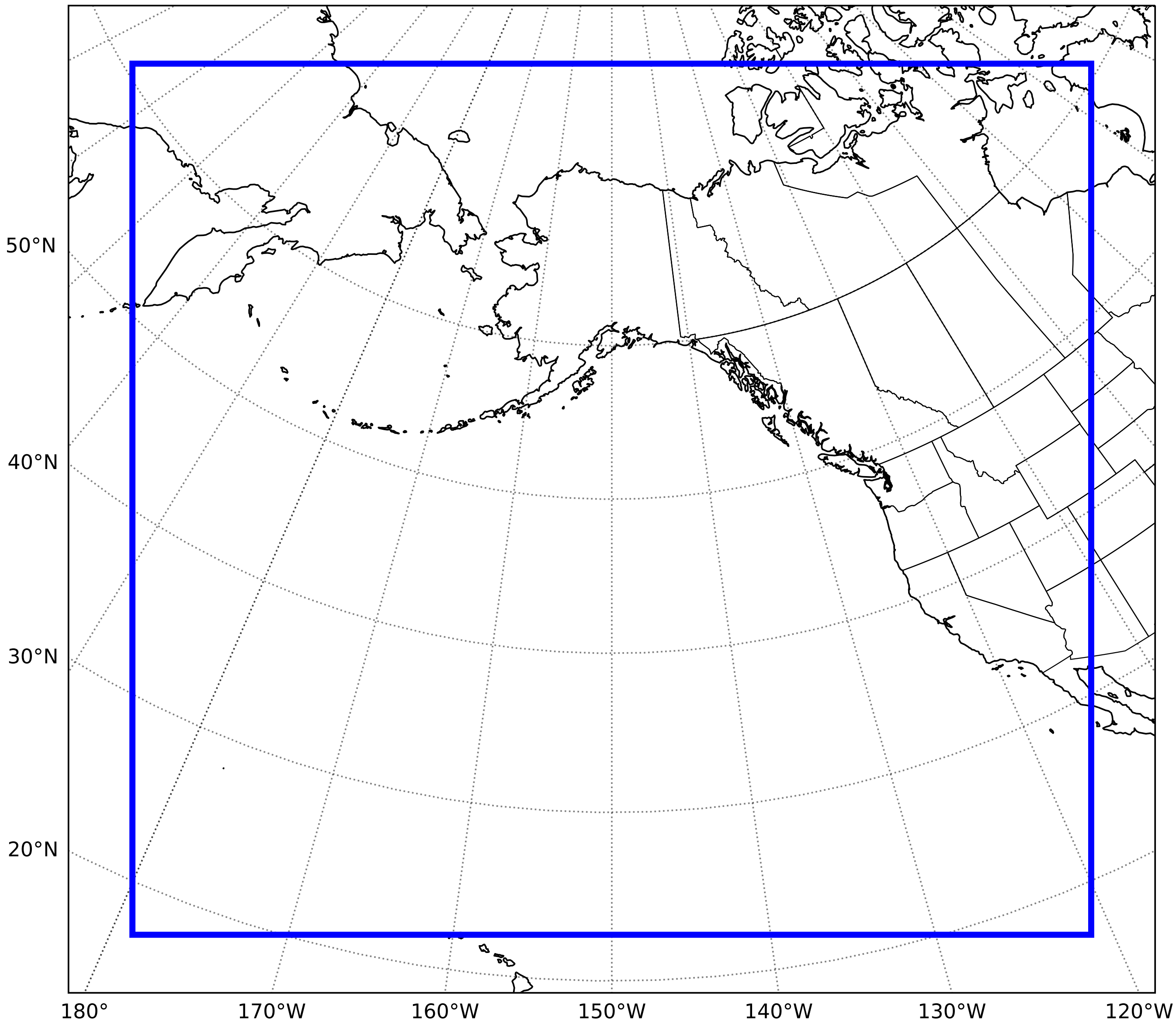

Figure 3.1. Model domain of the WRF simulation for the November 2019 storm with horizontal resolution of 30 km. Model domain is outlined by the blue box.

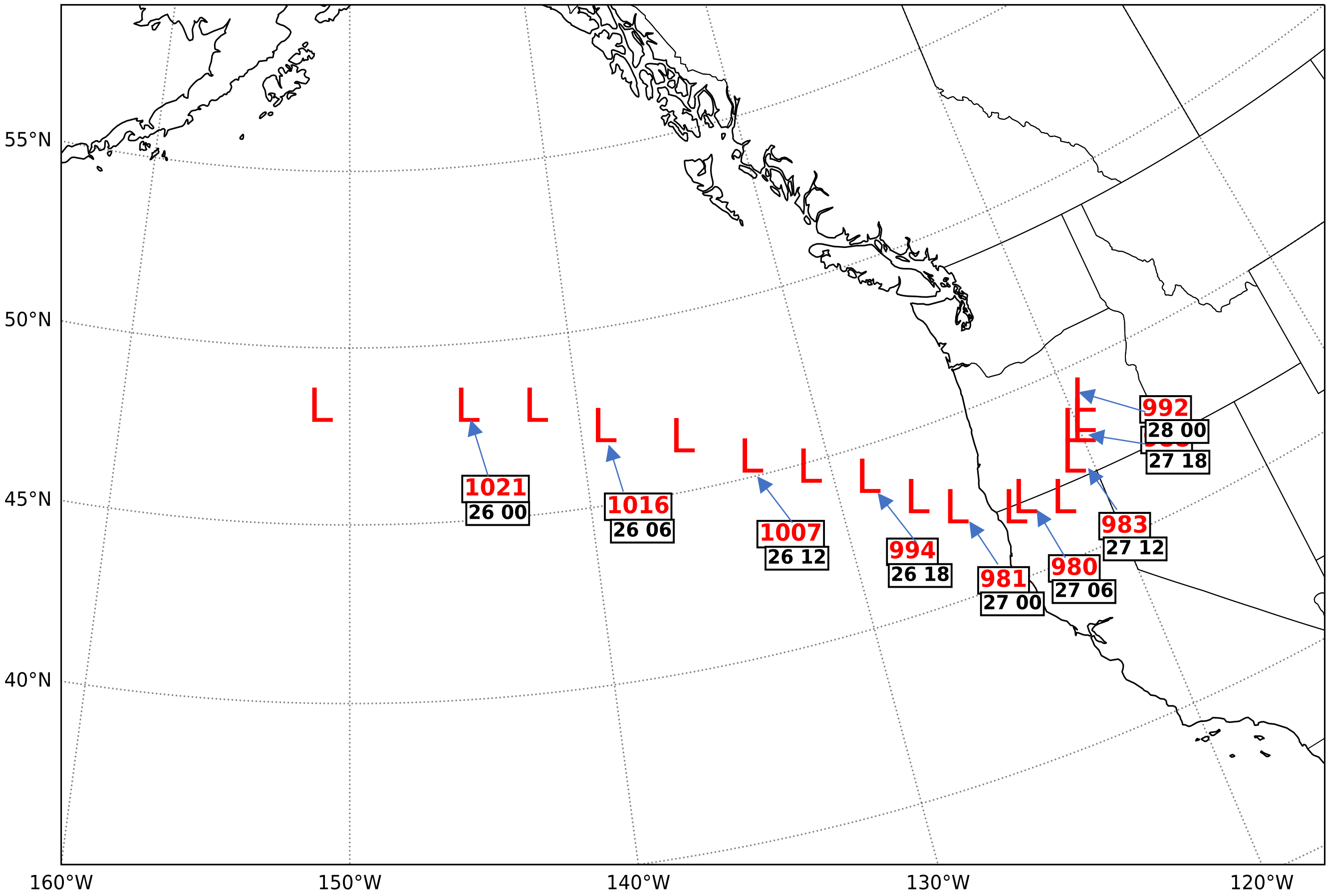

Figure 3.2. Storm track of the November 2019 storm from the WRF-model simulation based on location of the minimum in central sea-level pressure. Times are plotted in black and are in Universal Time Coordinated (UTC) where “26 00” indicates 0000 UTC 26 November 2019. Sea-level pressure is plotted in red and is in hectopascals. The red “L” indicates the location of the minimum central sea-level pressure.

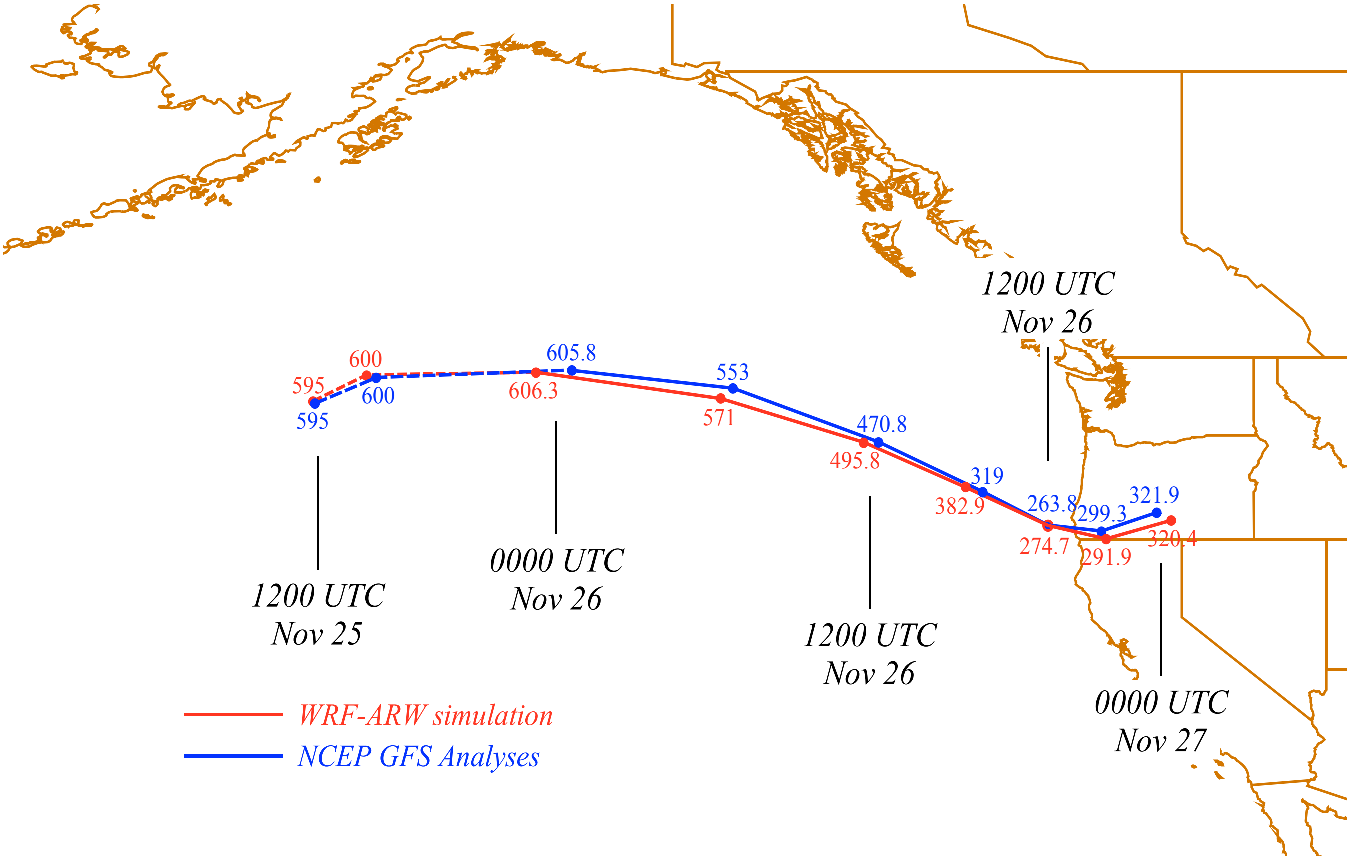

Figure 3.3. Comparison of the Weather Research and Forecasting - Advanced Research WRF model (WRF-ARW) simulation and National Centers for Environmental Prediction Global Forecast System (NCEP GFS) analysis of storm track based on location of height minima at 950 hPa. Location of WRF-ARW simulation height minima are shown in red and plotted in meters. Location of NCEP GFS analysis height minima are shown in blue and plotted in meters. Dashed contours represent approximate track before a low pressure center was officially analyzed.

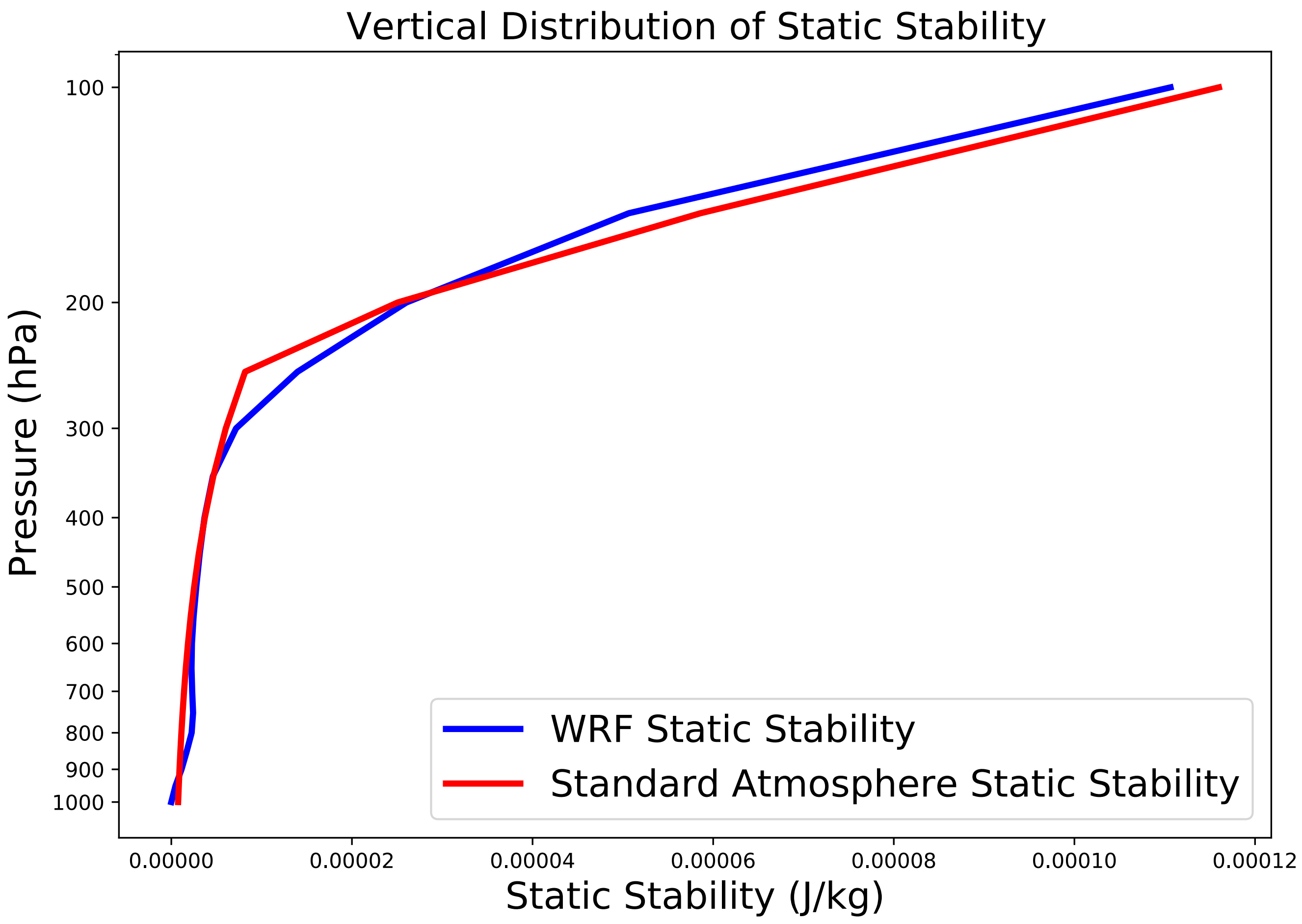

Figure 3.4. Comparison of static stability between the 1976 standard atmosphere static stability and the isobaric level average static stability from the WRF-model calculations for all isobaric levels within the WRF model domain. The 1976 standard atmosphere static stability is shown in red and plotted in J kg^{-1}. The WRF-model static stability is shown in blue and plotted in J kg^{-1}.

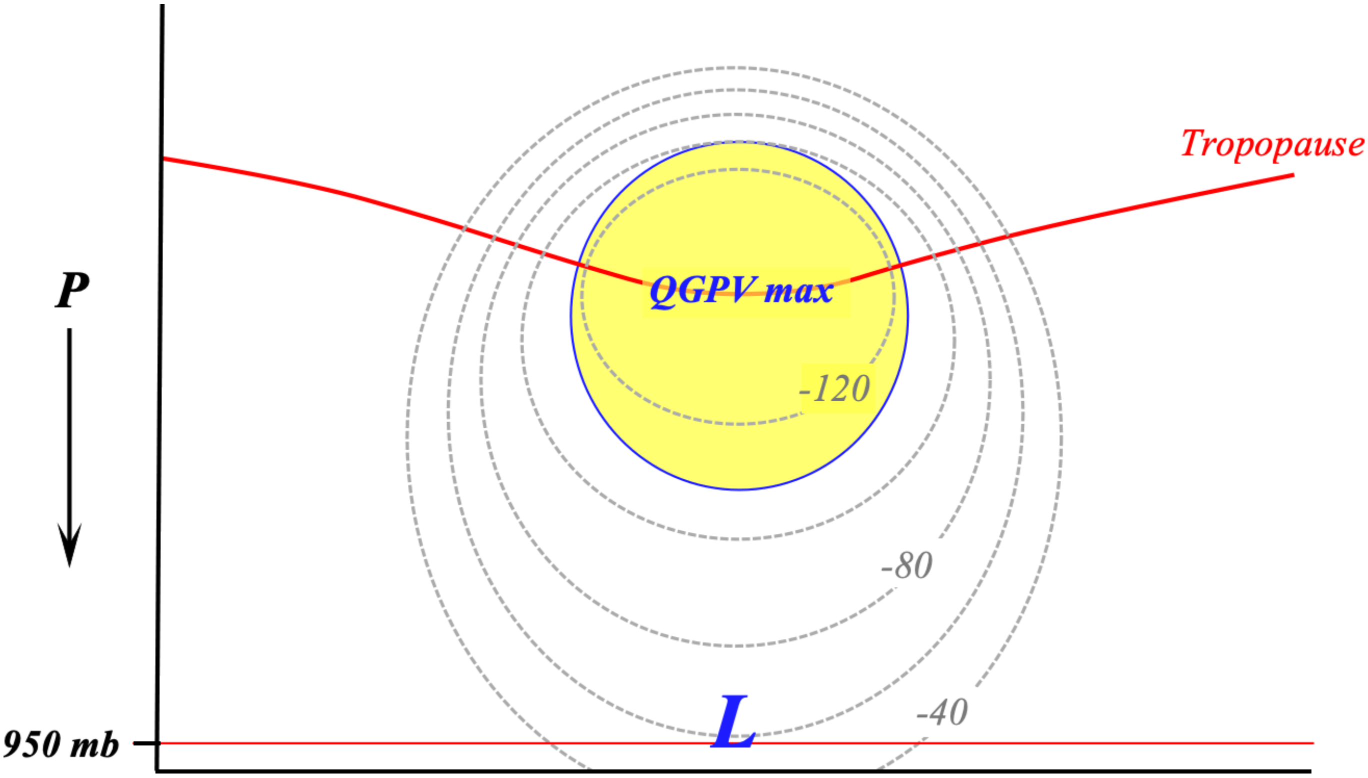

Figure 3.5. Schematic of idealized quasi-geostrophic potential vorticity (QGPV) anomaly located at the dynamic tropopause level and associated theoretical inverted geopotential heigh field in meters. QGPV anomaly denoted by yellow shading along dynamic tropopause. Location of the dynamic tropopause is contoured in solid red. Theoretical inverted geopotential height field is contoured in dashed gray every 20 meters. Location of a representative low pressure center is denoted by the blue “L” at 950 hPa.

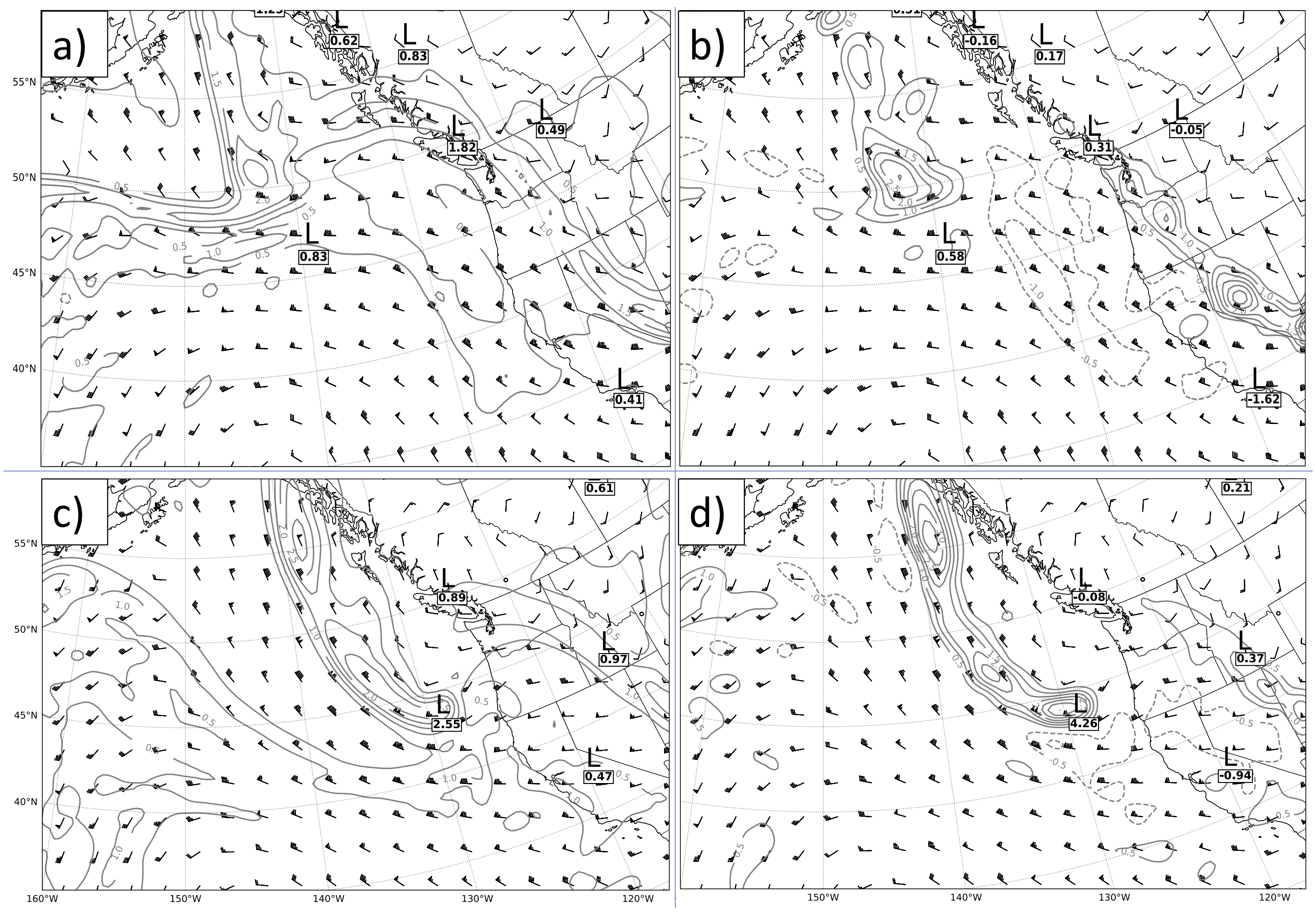

Figure 3.6. Comparison of Ertel potential vorticity (EPV) to quasi-geostrophic potential vorticity (QGPV) for two representative times during the rapid development of the November 2019 storm. (a.) 18-hour forecast valid 0600 UTC 26 November 2019 of EPV at 500 hPa. Gray contours are EPV in potential vorticity units (PVU) contoured every 0.5 PVU. Black "L" denotes location of 1000-hPa central sea-level pressure minimum and EPV at the location of the 1000-hPa central sea-level pressure minimum is plotted in PVU. (b.) 18-hour forecast valid 0600 UTC 26 November 2019 of quasi-geostrophic potential vorticity (QGPV) at 500 hPa, scaled by $-g\frac{\partial\theta}{\partial p}\ x\ 10^{6}$ to convert from units of s^{-1} to units of PVU, as in Hakim et al. (1996). Gray contours are QGPV in PVU contoured every 0.5 PVU. Black "L" denotes location of 1000-hPa central sea-level pressure minimum and QGPV at the location of the 1000-hPa central sea-level pressure minimum is plotted in PVU. (c.) 30-hour forecast valid 1800 UTC 26 November 2019 of EPV at 500 hPa. Gray contours are EPV in potential vorticity units (PVU) contoured every 0.5 PVU. Black "L"

denotes location of 1000-hPa central sea-level pressure minimum and EPV at the location of the 1000-hPa central sea-level pressure minimum is plotted in PVU. (d.) 30-hour forecast valid 1800 UTC 26 November 2019 of quasi-geostrophic potential vorticity (QGPV) at 500 hPa, scaled by $-g\frac{\partial\theta}{\partial p}\ x\ 10^6$ to convert from units of s^{-1} to units of PVU, as in Hakim et al. (1996). Gray contours are QGPV in PVU contoured every 0.5 PVU. Black "L" denotes location of 1000-hPa central sea-level pressure minimum and QGPV at the location of the 1000-hPa central sea-level pressure minimum is plotted in PVU.

4. QGPV INVERSION RESULTS

4.1 Diagnosis using partitioned inverted height anomalies from the QGPV

Through the partitioning of the QGPV into UPERT, MPERT, and SPERT, it is possible to evaluate which specific partitioned layer is driving development throughout the lifecycle of the NV19 storm. The inverted height anomaly field at 950 hPa associated with each of the partitioned layers will be compared to each other and to the results of inverting the full column[2] QGPV to assess their relative effects on near-surface development. An example of this method of investigation is shown in the cross-section taken at 1800 UTC 26 November 2019 in Fig. 4.1. A distribution of QGPV perturbations is inverted and their associated height anomalies (HA) are depicted in relation to the cyclone center. Stronger positive QGPV perturbations translates to stronger negative HA by equation (20) and one can assess which levels of the atmosphere are contributing the most to negative HA near the surface, which will alter the low-level height field and support storm development. The inverted height anomaly field associated with the diabatic heating term in equation (31) will also be compared to the inverted HA from UPERT, MPERT, and SPERT. The analysis will follow the same period and time interval as the synoptic overview in Chapter 2.1 and will be conducted at 950 hPa, as this is the lowest level for which the inversion of the QGPV is performed and most nearly describes surface development.

Beginning at 1200 UTC 25 November 2019, the development region of the NV19 storm was located in a small region of negative geopotential HA (Fig. 4.2a). Another region of negative HA extended from southeast of the development region towards central and southern California with a large band of positive HA stretching from the northwestern United States to the Aleutian Islands. The UPERT QGPV at this time made no contribution to any HA in the vicinity of the NV19 development region and can be considered negligible (Fig. 4.2b). The HA associated with the MPERT QGPV near the development region nearly mirrors that from the full inversion, and so the MPERT QGPV can be considered as driving the initial development of the NV19 storm (Fig. 4.2a; Fig. 4.2c). The spatial distribution of the HA from

---

[2] Defined as a column extending from 1000 hPa to 100 hPa and including 975 hPa potential temperature perturbation effects.

the MPERT QGPV is larger than that of the full inversion HA, indicating that another layer is acting to weaken the total HA. This weakening is reflected by the HA associated with the SPERT QGPV, which are positive in the development region of the NV19 storm (Fig. 4.2d). The positive SPERT HA around the development region are consistent with the negative potential temperature anomalies and a surface cold pool located there, as the SPERT QGPV includes the bottom-level potential temperature anomalies.

At 0000 UTC 26 November, the center of the NV19 storm is located over the northeast Pacific Ocean, almost exactly centered at 47.5ºN, 145 ºW. From the results of the full inversion, the NV19 storm is situated along a tongue of negative HA extending southeastward from 150ºW to 138ºW (Fig. 4.3a). In assessing the contribution to the HA associated with UPERT, it is clear from the geostrophic wind field that there is once again no significant contribution from the upper-level QGPV on the geopotential height field at 950 hPa at this time (Fig. 4.3b). However, the inverted HA from UPERT at the storm center suggests slight negative contributions to the 950 hPa geopotential height field at the location of the NV19 950 hPa storm center. The contribution of inverted HA associated with MPERT account for a bit more of the full inverted HA than UPERT but are also extremely weak (Fig. 4.3c). The storm center is situated in a region of weaker negative HA, with the geopotential height anomaly at the storm center describing roughly 6% of the full inversion HA. Like the other partitioned layers, SPERT also makes a negative contribution to the 950 hPa HA, however, its inverted HA nearly perfectly mimic the results from the full inversion (Fig. 4.3d). About 90% of the full inversion HA are accounted for by SPERT, coincident with a rather intense region of positive potential temperature anomalies of 6 to 8 K existing due south and southeast of the center of the storm. It is worth noting that the sum of the HA contributions associated with UPERT, MPERT, and SPERT at 0000 UTC 26 November account for nearly 98% of the full inversion HA (Fig. 4.3). This is a testament to the accuracy of the partitioning as the sum of the partitioned layers of QGPV should, theoretically, perfectly add up to the full inversion HA. Similar agreement is shown at the subsequent times, with the sum of the partitioned layer HA falling within at least 98% of the total inverted HA from the full column.

By 1200 UTC 26 November, the storm continued to move eastward as the negative full inversion HA at the storm center strengthened 83% compared to the previous time, reflecting consolidation of positive QGPV and its attendant impact on the development of the storm at 950 hPa at this time (Fig. 4.3a; Fig. 4.4a). The relative contribution from UPERT transitioned from weak to zero at this time (Fig. 4.4b). About 10% of the full inversion HA were contributed by the MPERT QGPVP (Fig. 4.4c). This 10% contribution signals the first time in which a layer other than SPERT had more than a 5% overall contribution to the full inversion HA. These inverted HA associated with MPERT were oriented in a compact circulation due north of the storm center. The remaining 90% of the storm's negative HA were contributed by the SPERT layer (Fig. 4.4d). Along with this, a robust and compact area of negative SPERT HA were located closer to the storm center than those associated with MPERT. These SPERT HA were coincident with a continued, strong lower boundary potential temperature perturbation that clearly identifies the near-surface warm sector.

Just before landfall, at 0000 UTC 27 November, the full inversion HA at the storm center were 66% larger than 12 hours prior, the second consecutive 12-hour period with a substantial full inversion HA magnitude increase (Fig. 4.3a; Fig. 4.4a; Fig. 4.5a). The magnitude of the piece of the inverted HA from the UPERT QGPV continued to remain insignificant as compared to the full column, with these HA contributions associated with UPERT being only 2% of the full column (Fig. 4.5b). The MPERT layer, meanwhile, made its maximum contribution to the full inversion HA up to this point in the lifecycle; about 21% (Fig. 4.5c). The inverted HA from MPERT also expanded in both magnitude and spatial distribution, reflecting how the MPERT QGPV was having an increasingly larger influence on the surface circulation near the time of landfall. The lower-boundary potential temperature perturbation was both displaced from, and weakened near, the center of the storm. This change was a factor in the reduced contribution of the SPERT HA (only 77%) compared to the full inversion HA (Fig. 4.5d). While this demonstrates that the SPERT QGPV was still dominating development at 950 hPa, it also signals the beginning of a weakening trend in the relative impact of the SPERT QGPV on the full inversion HA and 950 hPa cyclogenesis.

By 1200 UTC 27 November, the full inversion HA at the storm center had weakened by 42%, a sign of the corresponding cyclolysis period of the NV19 storm after rapid deepening (Fig. 4.6a). Negative HA from the full inversion dominated the entire western United States. The UPERT QGPV accounted for nearly 9% of the full inversion HA, its largest contribution of the analysis period, with the inverted geostrophic winds from the UPERT HA fostering a very broad, 950 hPa cyclonic circulation around the NV19 storm (Fig. 4.6b). The contribution of the MPERT HA to the full inversion HA was roughly 22%, a slight increase in total contribution from the previous analysis time (Fig. 4.5c; Fig. 4.6c). The HA associated with MPERT were also increasingly expansive, extending across much of the western United States and into southwest Canada. The SPERT HA remained the dominant contributor to the full inversion HA but continued to lose connection to the positive low-level potential temperature anomaly by which it had been supported throughout storm development (Fig. 4.6d). The trend of MPERT essentially gaining on SPERT with respect to contributions to the full inversion HA minimum continued as the storm moved inland and further lost connection to the lower-boundary potential temperature perturbation which had long contributed to its deepening (not shown).

4.2 Inverted height anomalies associated with diabatic heating

As previously stated, equation (31) suggests that QGPV can be derived to include a diabatic heating term, which would account for this otherwise neglected process in the derivation of the traditional QGPV. When calculated, this term has the same units and magnitude as the QGPV and can, therefore, be inverted using the same inversion operator as discussed in Chapter 3.3. It is then trivial, and useful, to perform an inversion on the diabatic term once the inversion calculations have already been performed on other distributions of the QGPV. The diabatic heating in equation (31), $\dot{Q}$, is output from the WRF model simulation to ensure calculations using the true diabatic heating represented in the model integrations during the lifecycle of the NV19 storm. The results then explain how the inclusion of $\dot{Q}$ and might impact the full inversion HA field.

Following a similar analysis as in Section 4.1, we begin with the distribution of inverted HA associated with the diabatic heating term at 950 hPa for the first analysis time: 1200 UTC 25 November

2019. There is no substantial contribution before the storm is first analyzed 6 hours later and this is reflected in the zero contribution of the inverted HA from the diabatic heating term at this time (Fig. 4.7a). At 0000 UTC 26 November, the inverted HA field exhibits a negative extremum located to the northeast of the 950 hPa storm center, while at the storm center the HA are close to zero (Fig. 4.7b). This shows that the diabatic heating contributes lower heights to the northeast of the storm center, coincident with the maximum in the 850 hPa positive frontogenesis as described in Chapter 2.1.1 (Fig. 2.2b). At 1200 UTC 26 November, twelve hours after initial formation, the influence of diabatic heating on the storm is more apparent in an intensified negative HA both near, and to the east of, the center of the storm (Fig. 4.7c). At this time, diabatic heating contributed negative inverted HA greater than those associated with the UPERT and MPERT QGPV and were $\frac{1}{6}$ of the magnitude of the contribution made by the SPERT QGPV (Fig. 4.4; Fig. 4.7c). At 0000 UTC 27 November, the storm was located in between two negative extrema of inverted HA and the contribution of the diabatic heating to the HA at the storm center was the highest of the analysis period (Fig. 4.7d). The inverted HA from the diabatic heating greatly expanded in spatial distribution and increased in magnitude, with the strongest portion of the HA being located to the southwest of the 950 hPa storm center along the now-expansive cold front (Fig. 2.4a). The inverted HA attributed to diabatic heating again explained more than the UPERT HA, 62% of the MPERT HA, and 17% of the SPERT HA at the same time (Fig. 4.5; Fig. 4.7d). Twelve hours later, the inverted HA from the diabatic heating term, though weakened, continued to surpass the HA associated with the UPERT QGPV, were roughly one half of the HA associated with the MPERT QGPV, and were 11% of the SPERT HA (Fig. 4.7e).

A noteworthy feature for discussion is the relative location between the 950 hPa HA associated with the diabatic heating term and the NV19 storm center. For 0000 UTC 26 November – 0000 UTC 27 November, the 950 hPa HA minimum associated with the inversion of the diabatic heating term is located downstream of the storm center (Fig. 4.7b – 4.7d). This means that the influence of the diabatic heating on the inverted HA is occurring ahead of the storm center during this period, which is consistent with the downstream-biased cloud shield characteristic of extratropical cyclones. This geometry ceases at 0000 UTC 27 November when the influence of the diabatic heating is most notable upstream and to the southwest of the 950 hPa cyclone center (Fig. 4.7d) and this influence remains upstream and situated just off the California-Oregon border as the cyclone moved inland (Fig. 4.7e). The change in storm-relative location of the influence of the diabatic heating coincides with the storm being dominated by cold air advection along the expansive cold front and signals the end of the extreme deepening period of the storm (Fig. 2.4a).

Adding to the complexity of how the NV19 storm developed, tracked, and underwent maximum deepening, a pronounced region of strong, positive diabatic heating emerged downstream of the surface cyclone, extremely close to the surface, and persisted in proximity to the storm as both it and the NV19 storm underwent strengthening. This diabatic heating is most likely associated with a distinct warm front during the lifecycle of the storm. From 1200 UTC 25 November to 0000 UTC 26 November 2019, areas of relatively strong diabatic heating and cooling developed below 400 hPa in the vicinity of the storm, with the maximum in diabatic heating being situated to the east/northeast of the 950 hPa cyclone (Fig. 4.9). The maximum was located at 850 hPa and extended vertically from 950 hPa to 750 hPa. During the next twelve-hour period, this low-level region of positive diabatic heating greatly expanded in strength and vertical extent, while remaining east/northeast of the NV19 storm (Fig. 4.10). The diabatic heating now extended from 850 hPa to 400 hPa, with the center of the diabatic heating being located around 650 hPa. While the storm underwent its most rapid deepening period, the positive diabatic heating region split into two regions of positive maxima located to the east/northeast of the storm, with one region extending from 575 hPa to 350 hPa and the other extending from 900 hPa to 625 hPa (Fig. 4.11). This lower-level positive diabatic heating maintained strength but shrunk in the vertical and horizontal as the cyclone began to interact with topography. As the NV19 storm moved inland, the main regions of positive diabatic heating were now well removed from the 950 hPa cyclone, while weakening in magnitude but maintaining vertical extent (Fig. 4.12).

Under the influence of this low-level diabatic heating, an area of low-level positive QGPV began to develop between 1200 UTC 25 November and 0000 UTC 26 November, as reflected by the emergence of an area of low-level negative HA to the immediate east of the developing storm (Fig. 4.13a; Fig. 4.14a). At these first two analysis times, the mid and upper-levels, represented by MPERT and UPERT, are characterized by positive HA associated with negative QGPV anomalies (Figs. 4.13b-c, Figs. 4.14b-c). While the storm strengthened and moved eastward, distinct regions of negative HA anomalies associated with positive QGPV anomalies began to develop within the MPERT and UPERT layers at 1200 UTC 26 November, with the persistence of the SPERT positive QGPV anomaly and negative HA now directly over the 950 hPa cyclone (Figs. 4.15a-c). Positive QGPV anomalies situated above the 950 hPa cyclone forced an area of negative HA to extend from 950 hPa to above 200 hPa (Fig. 4.15d). While this vertical extension may suggest UPERT HA influencing HA at 950 hPa, the individual inversion of the UPERT QGPV anomalies shows HA only extending down to 650 hPa, meaning that the UPERT QGPV was not influencing HA at the location of the NV19 storm (Fig. 4.15a). At 0000 UTC 27 November, positive QGPV anomalies in all three partitioned levels significantly strengthened as tropopause subduction by the upper front began to also influence development, with associated negative HA reflecting this strengthening (Figs. 4.16a-d). HA associated with the UPERT QGPV anomalies extended down to 700 hPa but were still having no effect on HA at 950 hPa (Fig. 4.16a). However, both the MPERT and SPERT HA were analyzed as affecting HA at 950 hPa at this time, with the SPERT HA describing 83% of the total HA at the location of the 950 hPa cyclone (Figs. 4.16b-c). The total vertical HA showed two areas of maximum in QGPV anomalies, with the maximum situated at 850 hPa forcing the low-level HA minimum directly over the 950 hPa storm (Fig. 4.16d). At 1200 UTC 27 November, as the storm moved inland, a lot of detail in the low-level QGPV anomalies and HA was lost due to orographic effects. Despite this, the signature of lack of influence from the UPERT QGPV remains, as the HA from these QGPV anomalies extended to now 800 hPa despite a very strong positive QGPV maximum in this layer (Fig. 4.17a). The MPERT and SPERT HA described the HA in the lowest 100 hPa, although the strength of these HA appears reduced from the cross-section viewpoint (Figs. 4.17b-d).

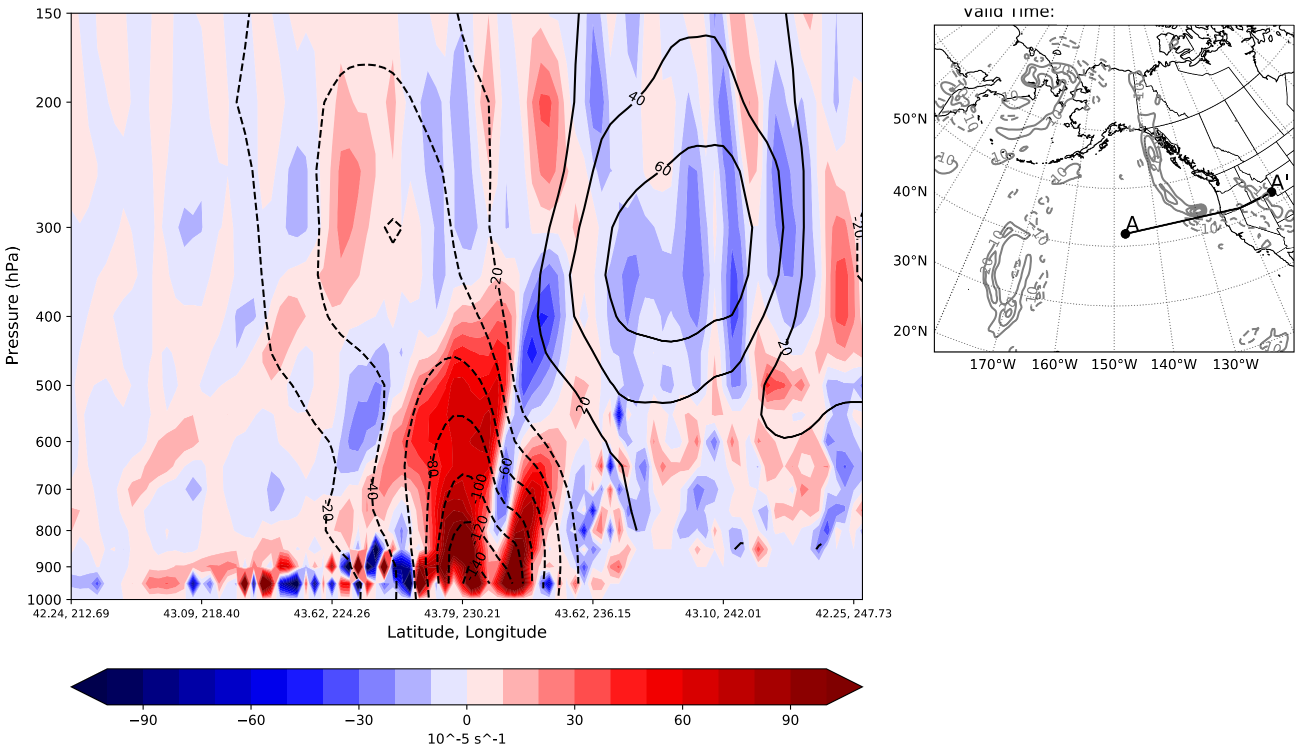

Figure 4.1. Cross-section of a representative distribution of QGPV perturbations and their associated inverted height anomaly field at 1800 UTC 26 November 2019 (left). QGPV perturbations are shown by the color fill and filled every $10 \times 10^{-5}\ s^{-1}$. The inverted height anomaly field is contoured every 20 m, with negative height anomalies depicted as dashed contours and positive height anomalies depicted as full contours. 500 hPa QGPV perturbation at 1800 UTC 26 November 2019 with cross section shown from A to A' (right). QGPV perturbations are contoured every $10 \times 10^{-5}\ s^{-1}$ with dashed contours representing negative QGPV perturbation values and full contours representing positive QGPV perturbation values.

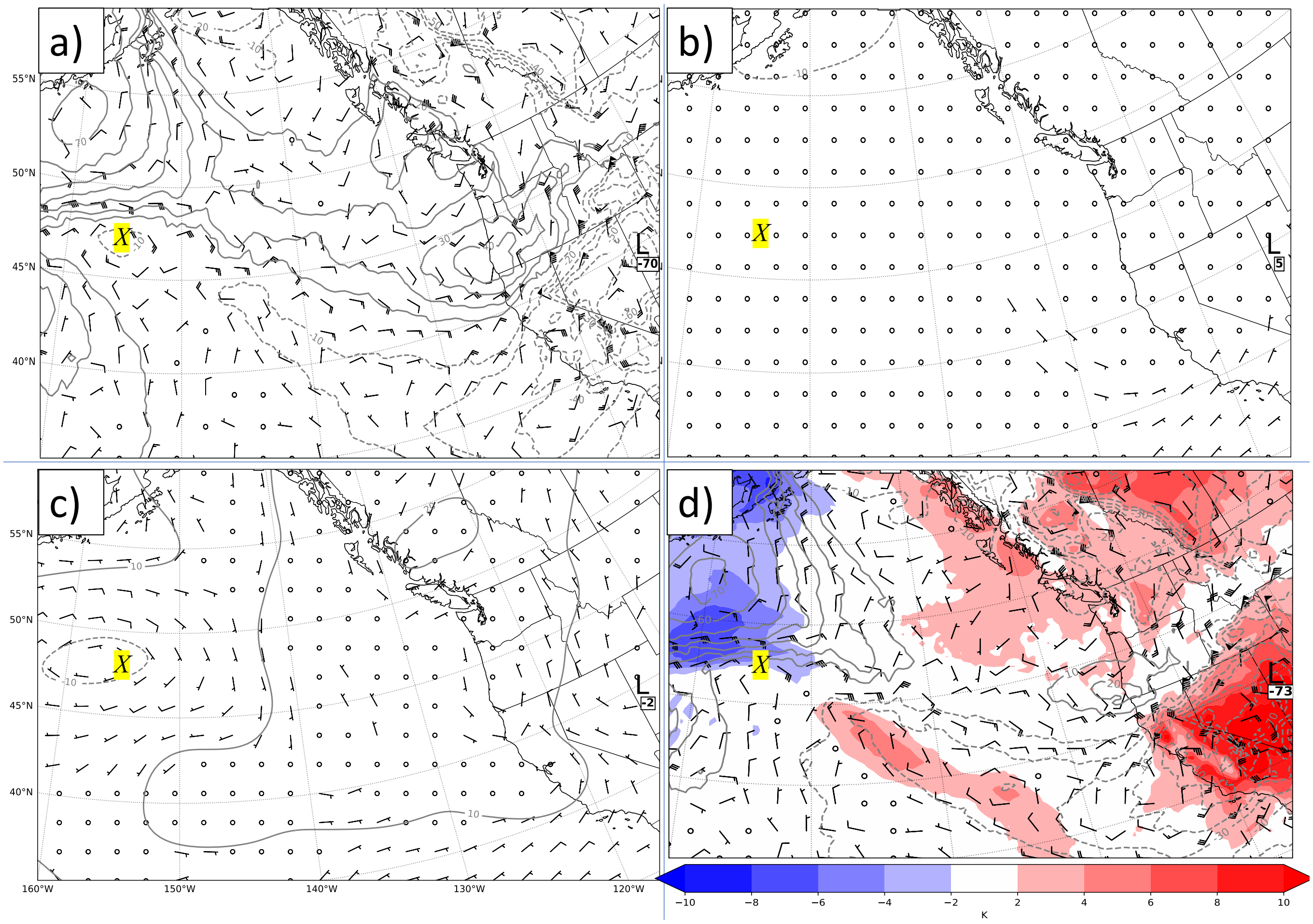

Figure 4.2. Geopotential height anomalies and associated geostrophic winds at 950 hPa from the inversion of the partitioned layers of QGPV at 1200 UTC 25 November 2019. Geopotential height anomalies are contoured in meters every 10 meters with full contours representing positive geopotential height anomalies and dashed contours representing negative geopotential height anomalies. Geostrophic wind speed and direction are depicted as barbs and are plotted in knots. Yellow-highlighted "X" indicates the surface development area of the November 2019 storm. (a.) Inversion results from the full column QGPV. (b.) Inversion results from the UPERT partitioned layer. (c.) Inversion results from the MPERT partitioned layer. (d.) Inversion results from the SPERT partitioned layer. Also shown is the boundary-level potential temperature anomaly depicted by the color fill and plotted in Kelvin.

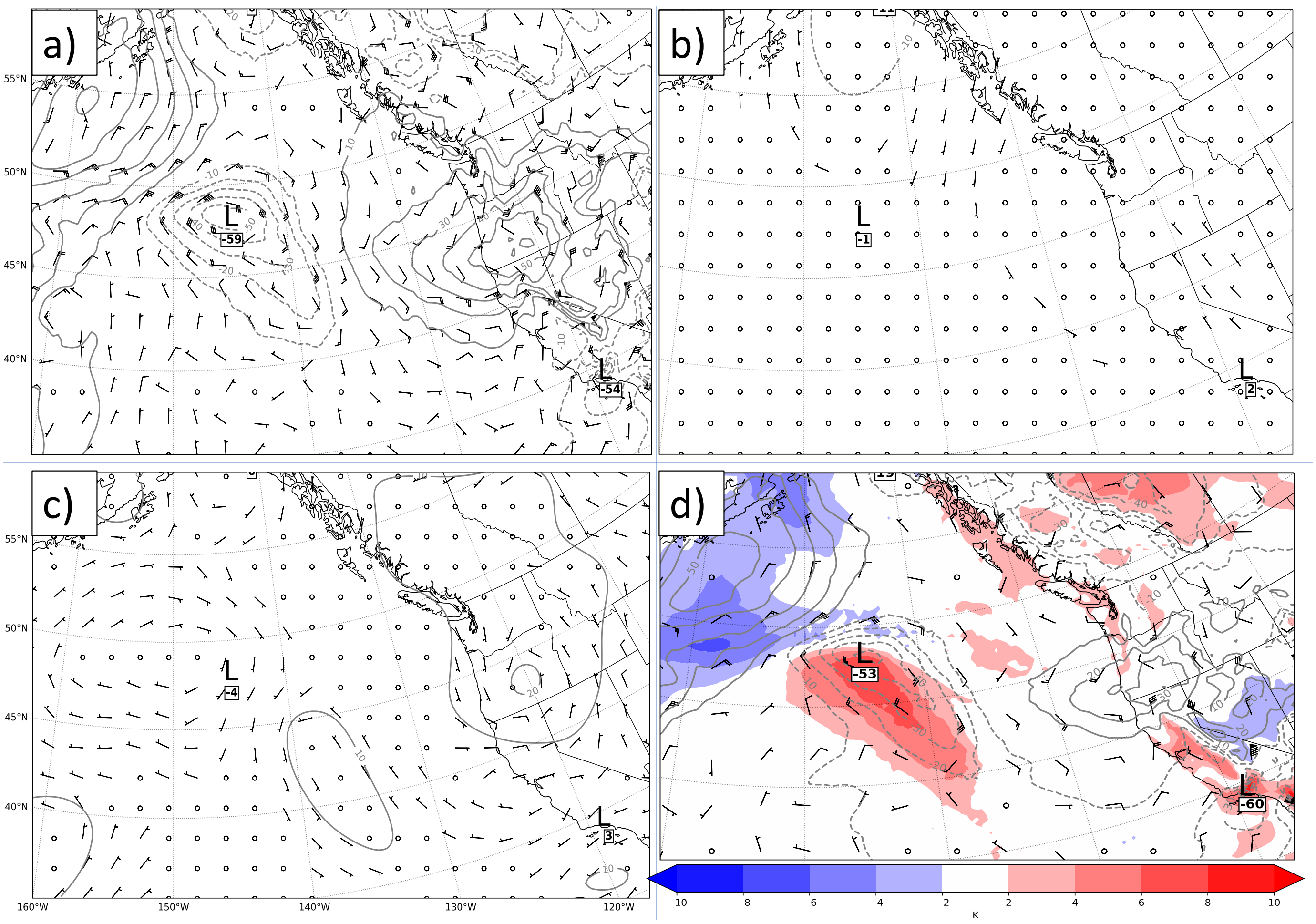

Figure 4.3. As for Fig. 4.2 but for 0000 UTC 26 November 2019 and black "L" denotes location of 950-hPa central sea-level pressure minimum and the inverted geopotential height at the location of the 950-hPa central sea-level pressure minimum is plotted underneath the "L" in meters. (a.) Inversion results from the full atmospheric column QGPV. (b.) Inversion results from the UPERT partitioned layer. (c.) Inversion results from the MPERT partitioned layer. (d.) Inversion results from the SPERT partitioned layer. Also shown is the boundary-level potential temperature anomaly depicted by the color fill and plotted in Kelvin.

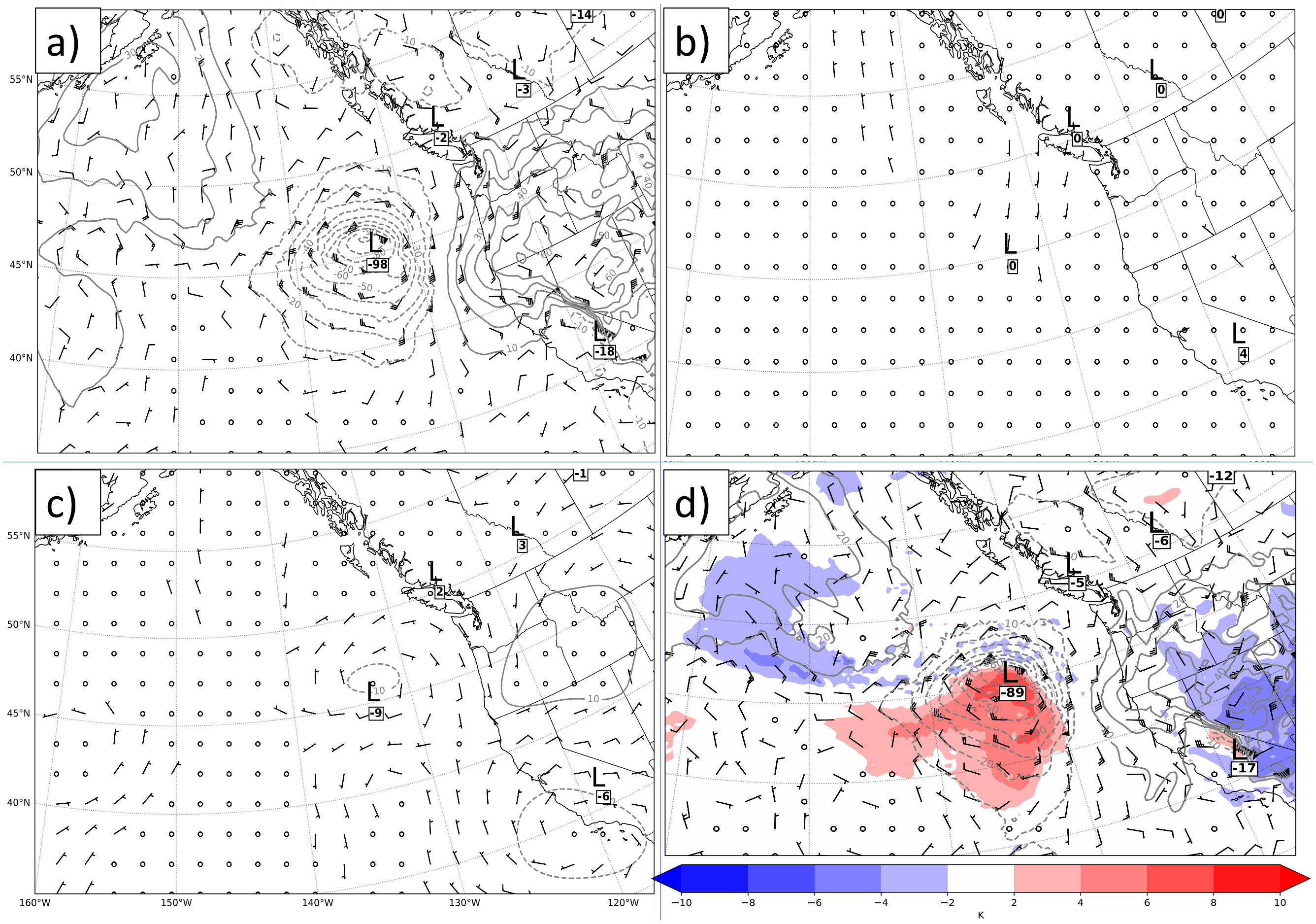

Figure 4.4. As for Fig. 4.3 but for 1200 UTC 26 November 2019. (a.) Inversion results from the full atmospheric column QGPV. (b.) Inversion results from the UPERT partitioned layer. (c.) Inversion results from the MPERT partitioned layer. (d.) Inversion results from the SPERT partitioned layer. Also shown is the boundary-level potential temperature anomaly depicted by the color fill and plotted in Kelvin.

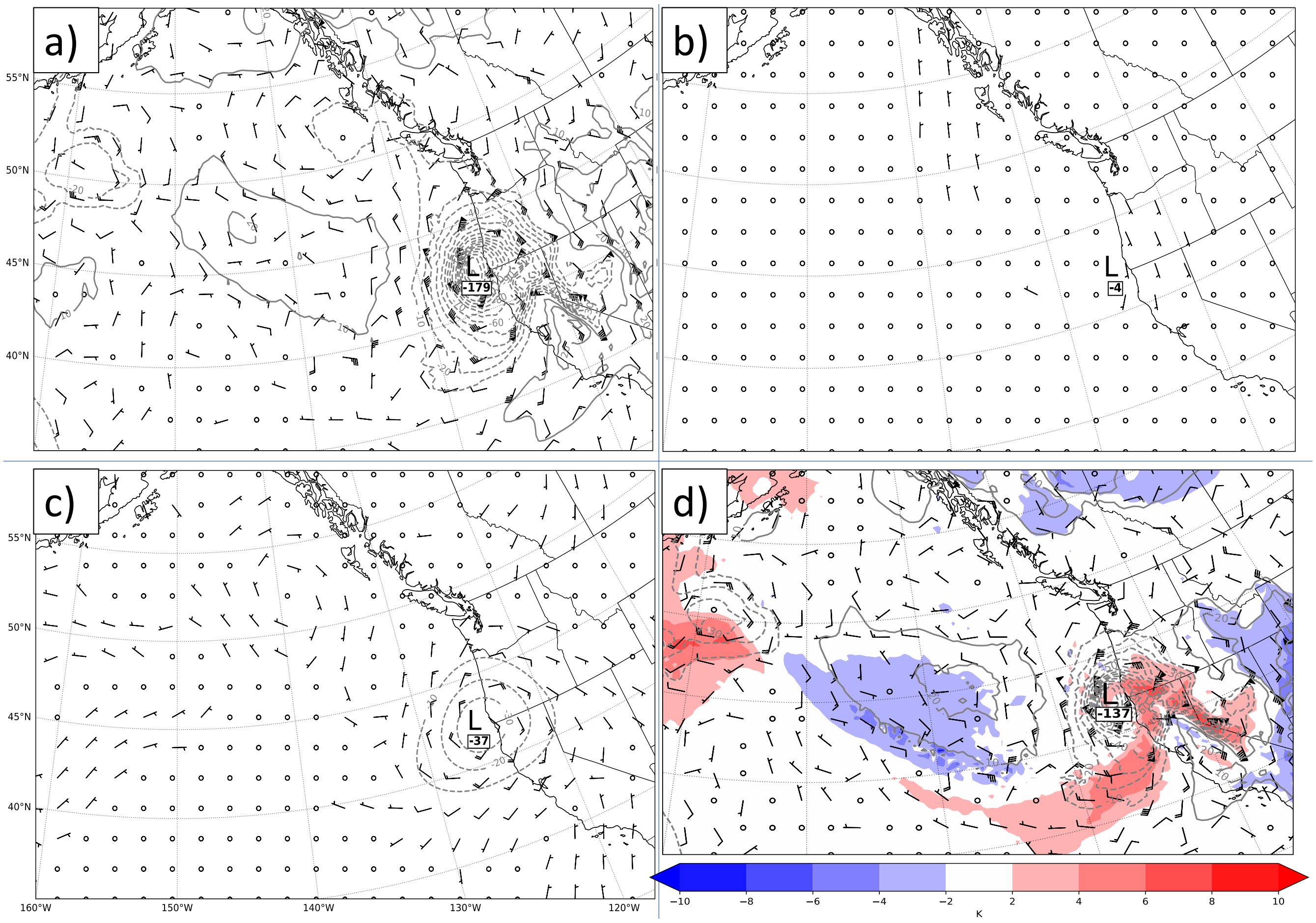

Figure 4.5. As for Fig. 4.4 but for 0000 UTC 27 November 2019. (a.) Inversion results from the full atmospheric column QGPV. (b.) Inversion results from the UPERT partitioned layer. (c.) Inversion results from the MPERT partitioned layer. (d.) Inversion results from the SPERT partitioned layer. Also shown is the boundary-level potential temperature anomaly depicted by the color fill and plotted in Kelvin.

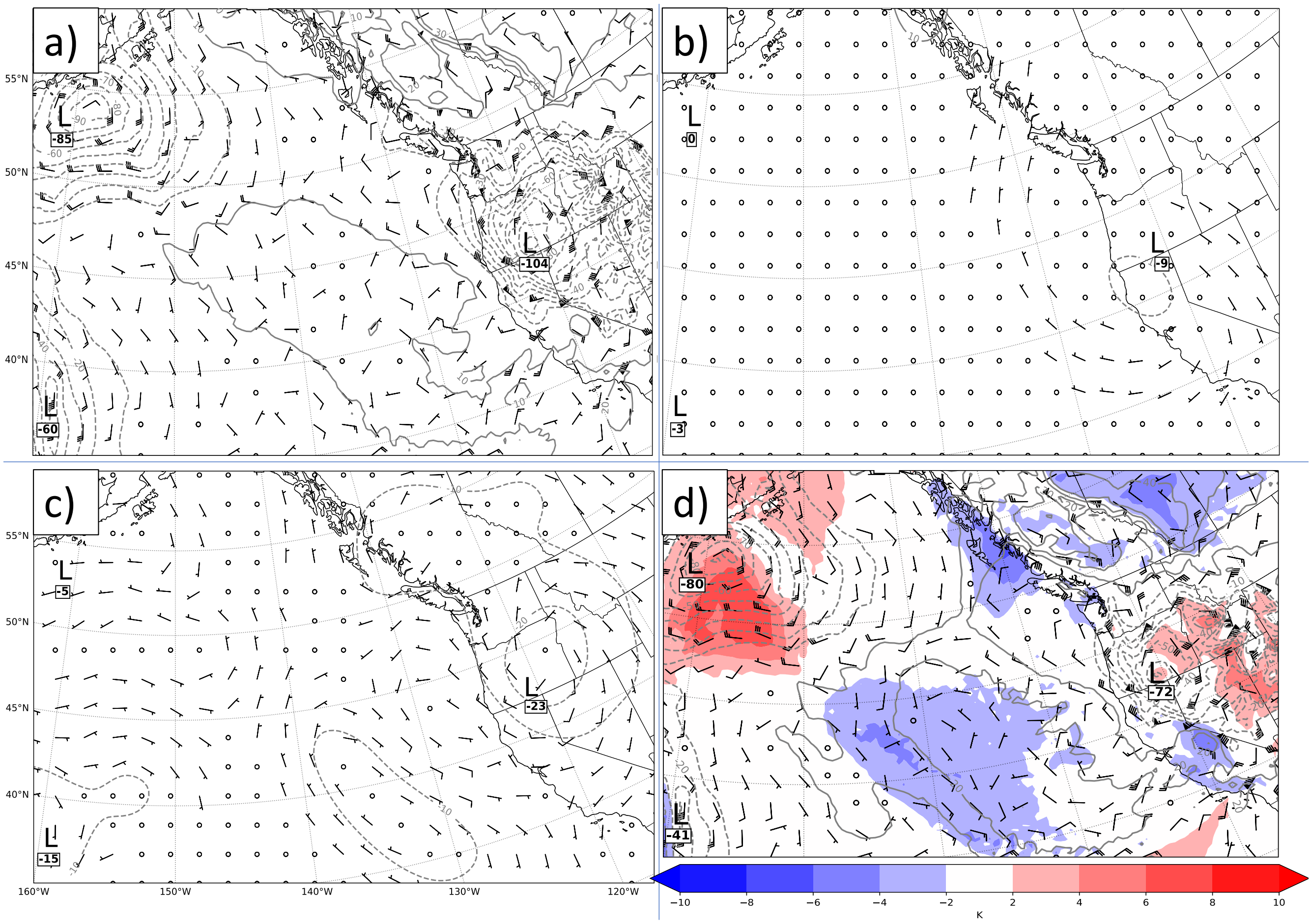

Figure 4.6. As for Fig. 4.5 but for 1200 UTC 27 November 2019. (a.) Inversion results from the full atmospheric column QGPV. (b.) Inversion results from the UPERT partitioned layer. (c.) Inversion results from the MPERT partitioned layer. (d.) Inversion results from the SPERT partitioned layer. Also shown is the boundary-level potential temperature anomaly depicted by the color fill and plotted in Kelvin.

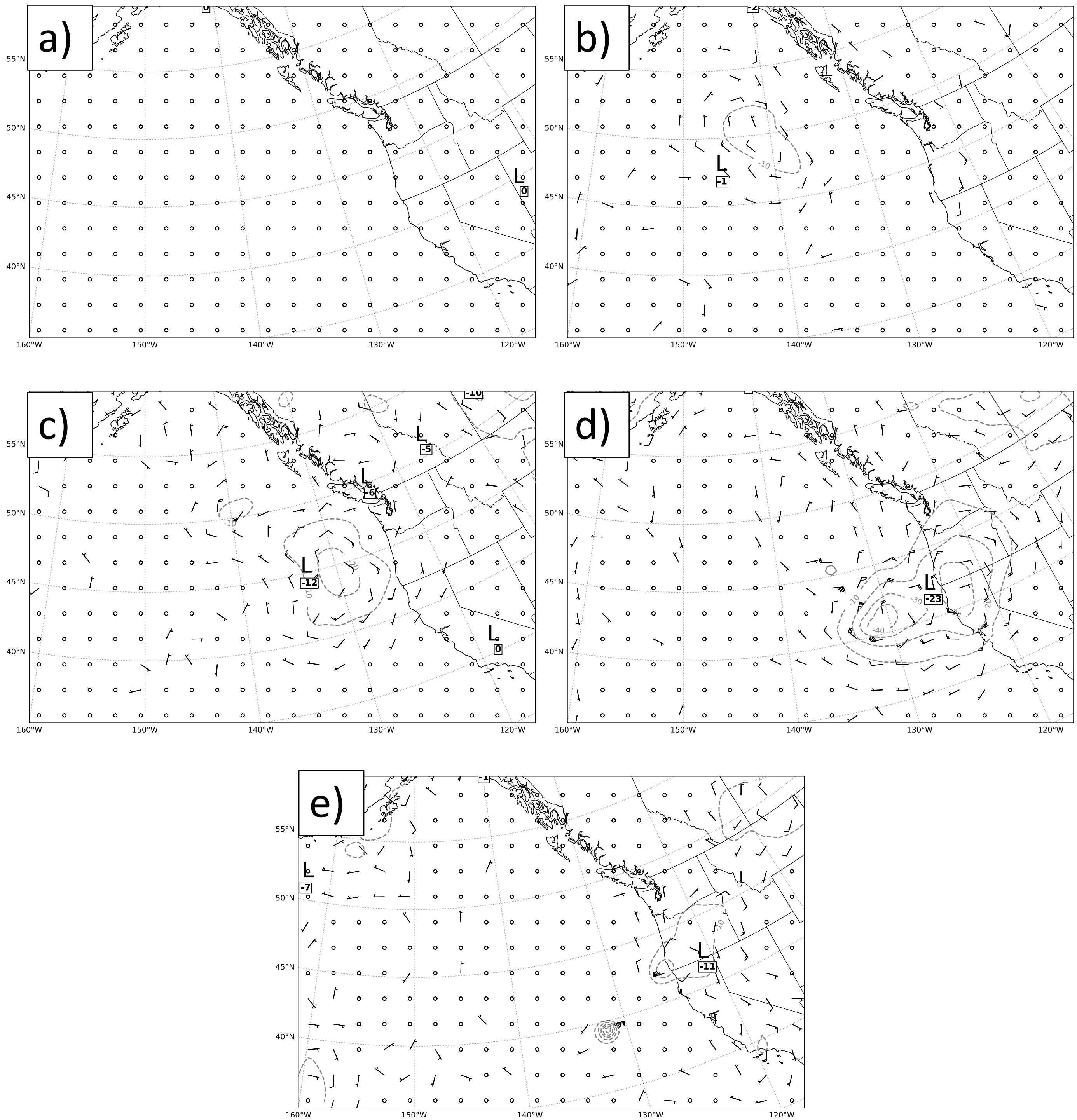

Figure 4.7. Geopotential heights and associated geostrophic winds from the inversion of the diabatic heating term at 950 hPa at (a.) 1200 UTC 25 November 2019, (b.) 0000 UTC 26 November 2019, (c.) 1200 UTC 26 November 2019, (d.) 0000 27 November 2019, and (e.) 1200 UTC 27 November 2019. Heights are contoured in meters every 10 meters with full contours representing positive heights and

dashed contours representing negative heights. Winds are depicted as barbs and are plotted in knots. Black “L” denotes location of 950-hPa geopotential height minimum and the inverted height at the location of the 950-hPa central geopotential height minimum is plotted in meters.

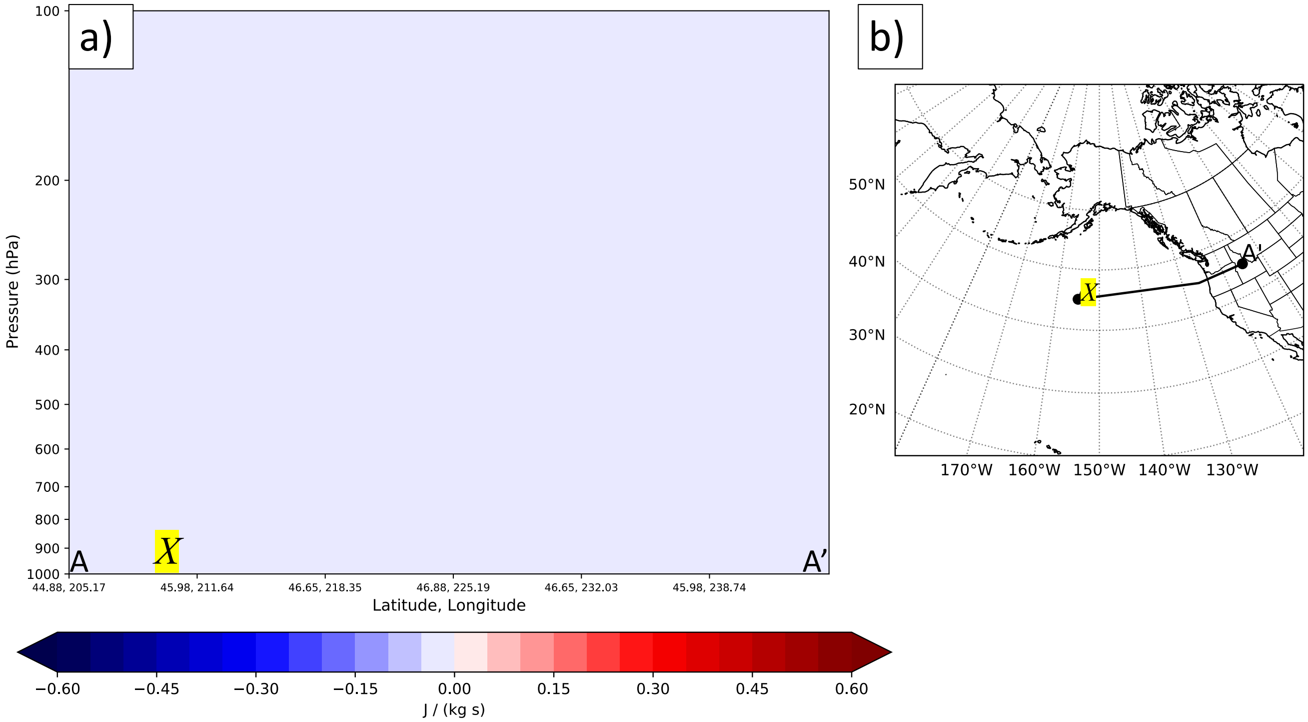

Figure 4.8. Diabatic heating from the WRF model simulation of the November 2019 storm valid 1200 UTC 25 November. (a). Cross section of diabatic heating represented by the color fill and contoured every 0.05 J kg^{-1} s^{-1} where red indicates positive diabatic heating and blue indicates negative diabatic heating, or diabatic cooling. Yellow-highlighted “X” indicates the region of storm development. (b). Diabatic heating at 600 hPa contoured in gray every 0.2 J kg^{-1} s^{-1} where solid contours indicate positive diabatic heating and dashed contours indicate diabatic cooling. Area of the cross sections in (a). depicted by the black line drawn from A to A’. Yellow-highlighted “X” indicates the region of storm development.

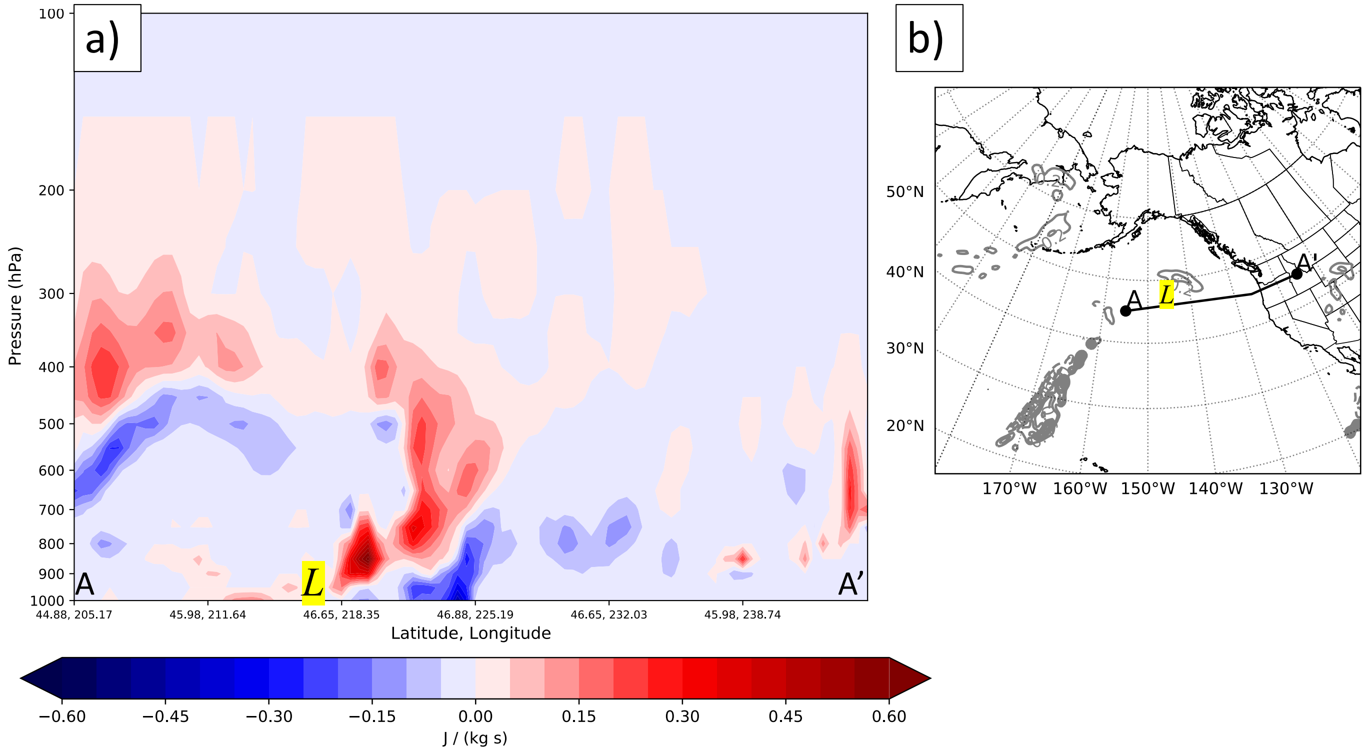

Figure 4.9. As in Fig. 4.8 but valid for 0000 UTC 26 November 2019. Yellow-highlighted "L" indicates the location of the surface geopotential height minimum on both (a). and (b).

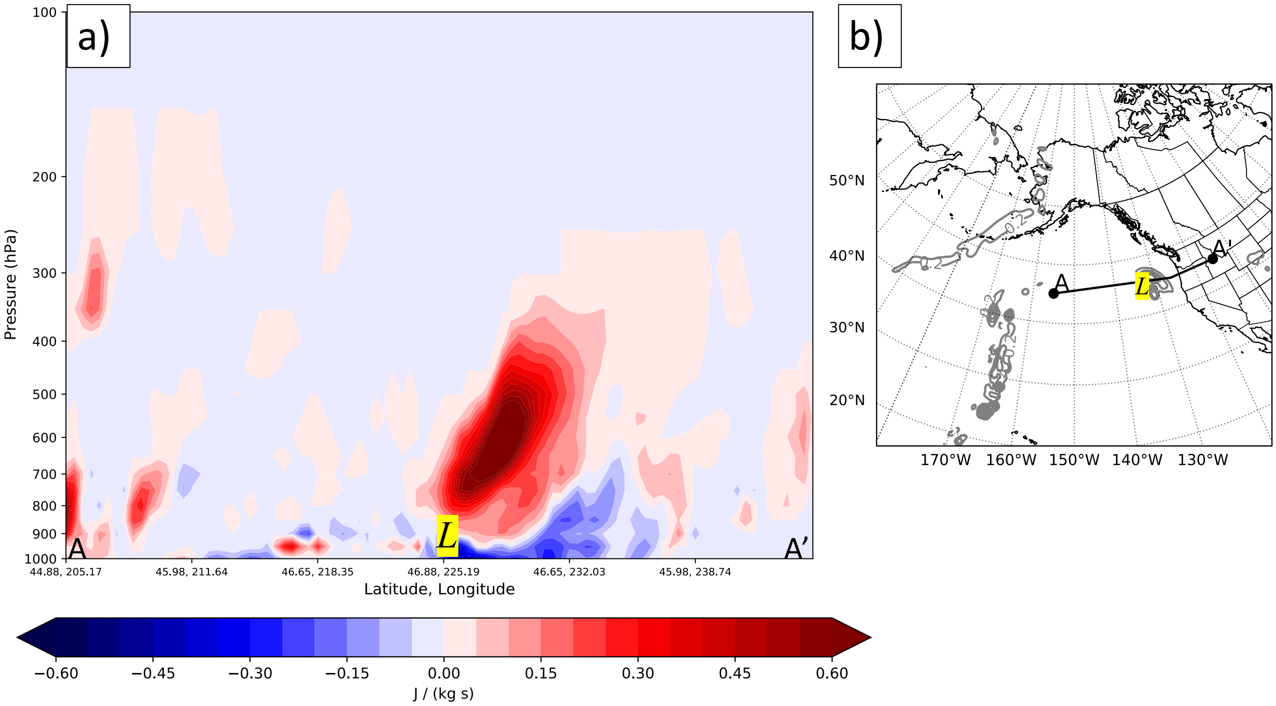

Figure 4.10. As in Fig. 4.9 but valid for 1200 UTC 26 November 2019.

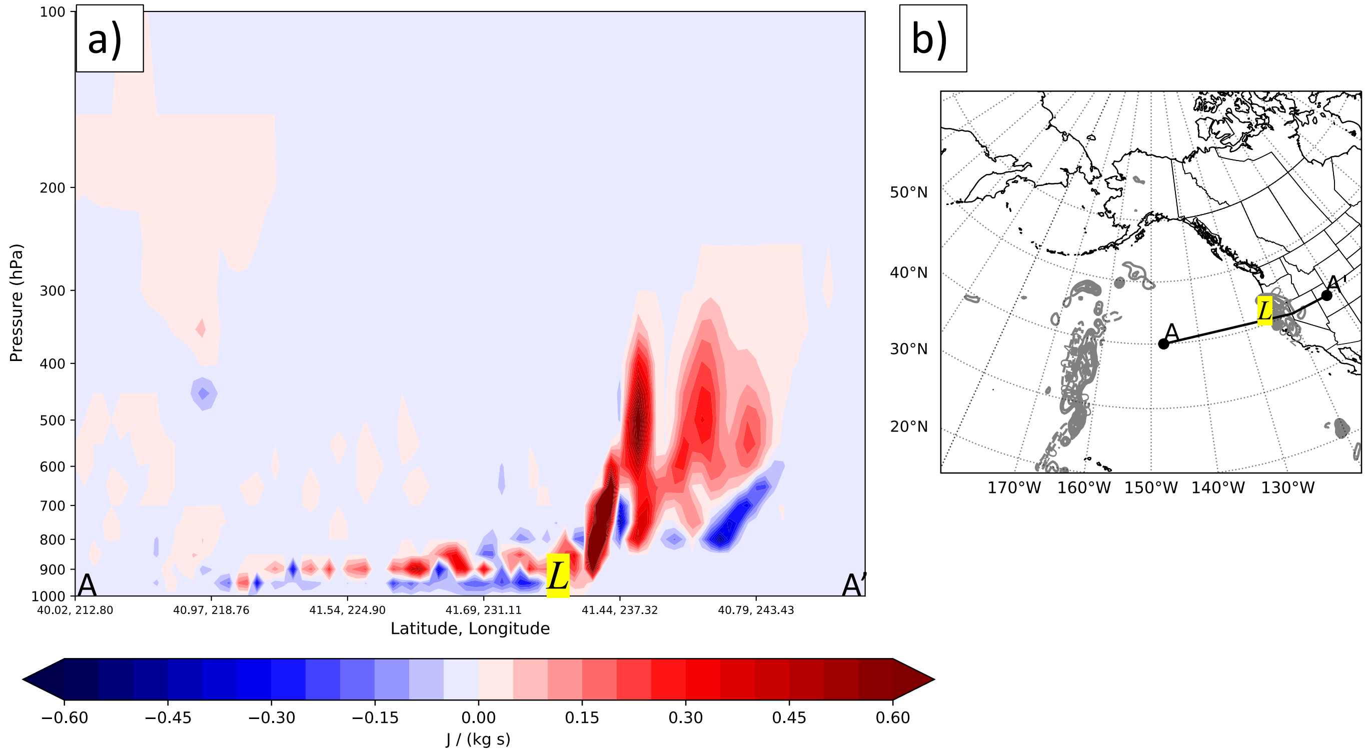

Figure 4.11. As in Fig. 4.10 but valid for 0000 UTC 27 November 2019.

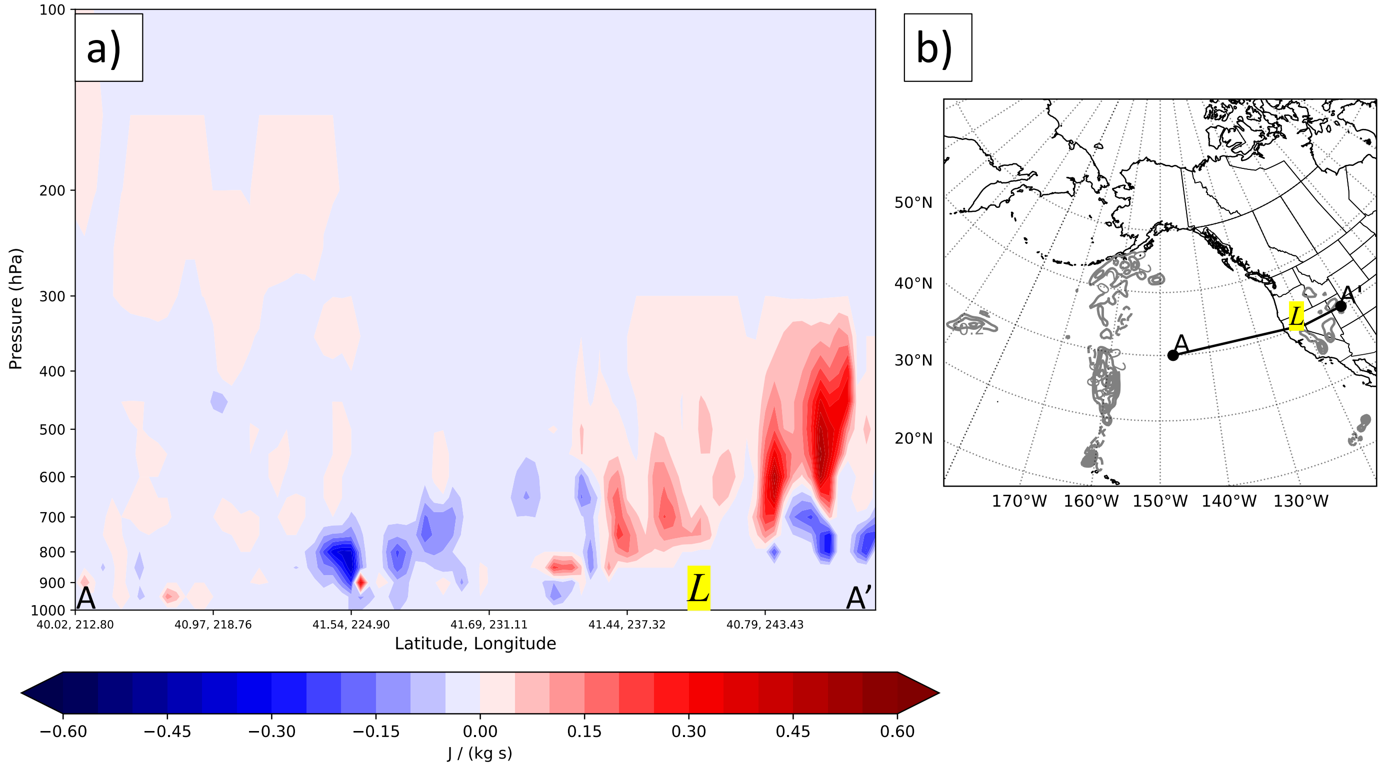

Figure 4.12. As in Fig. 4.11 but valid for 1200 UTC 27 November 2019.

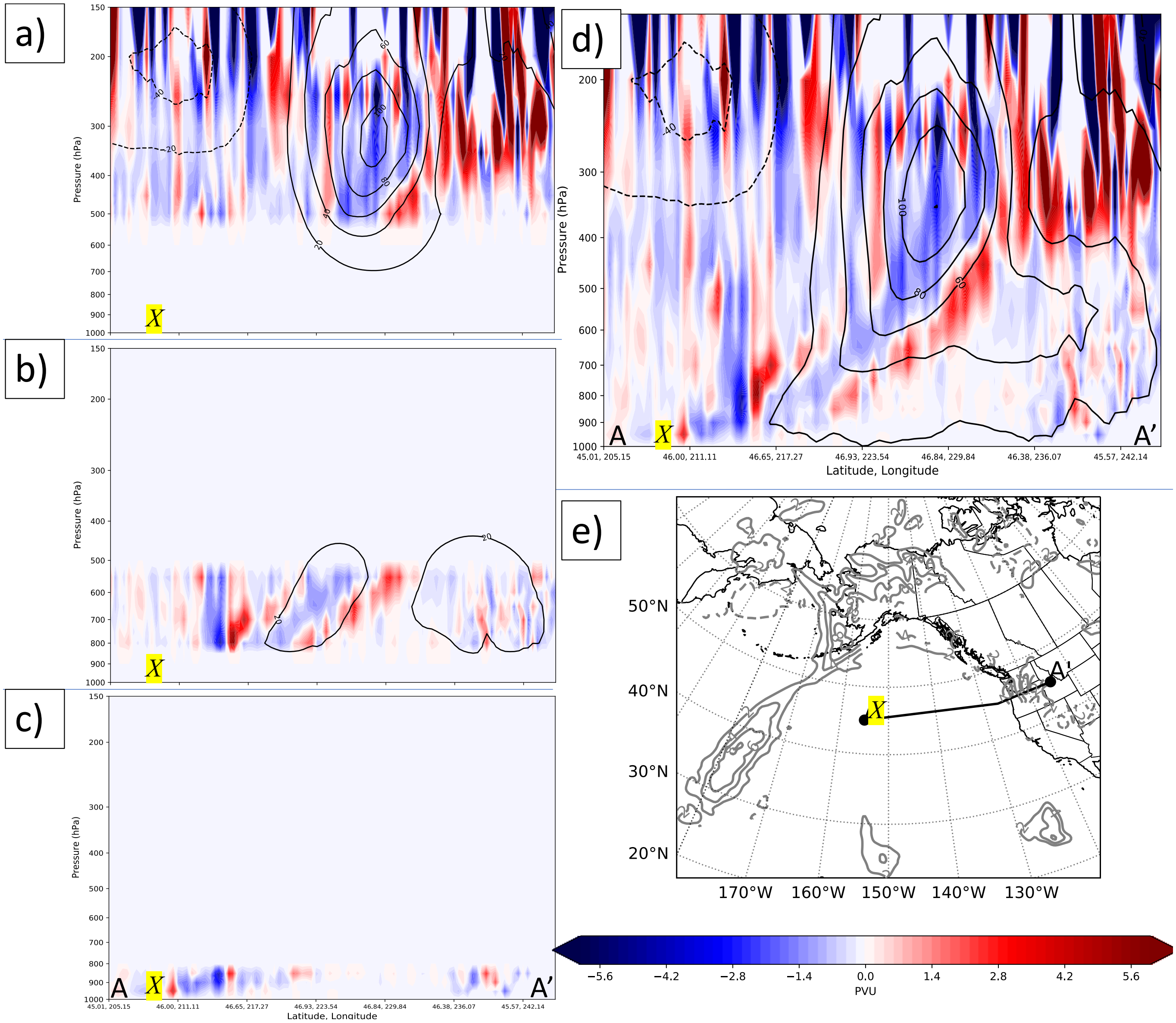

Figure 4.13. Cross sections of the distribution of QGPV perturbations and associated inverted geostrophic height anomalies valid 1200 UTC 25 November 2019. QGPV perturbations are shown by the color fill and are plotted in potential vorticity units (PVU). Inverted geostrophic height anomalies are contoured in black in meters. Solid contours represent positive inverted geostrophic height anomalies and dashed contours represent negative inverted geostrophic height anomalies. Yellow-highlighted “X” indicates the region of storm development. (a). QGPV perturbations and inverted geostrophic height anomalies associated with UPERT. (b). QGPV perturbations and inverted height anomalies associated with MPERT.

(c). QGPV perturbations and inverted height anomalies associated with SPERT. (d). QGPV perturbations and inverted height anomalies associated with the full column. (e). 300 hPa QGPV perturbations contoured in gray, with solid contours representing positive QGPV perturbations and dashed contours representing negative QGPV perturbations. Area of the cross sections in (a). through (d). depicted by the black line drawn from A to A’.

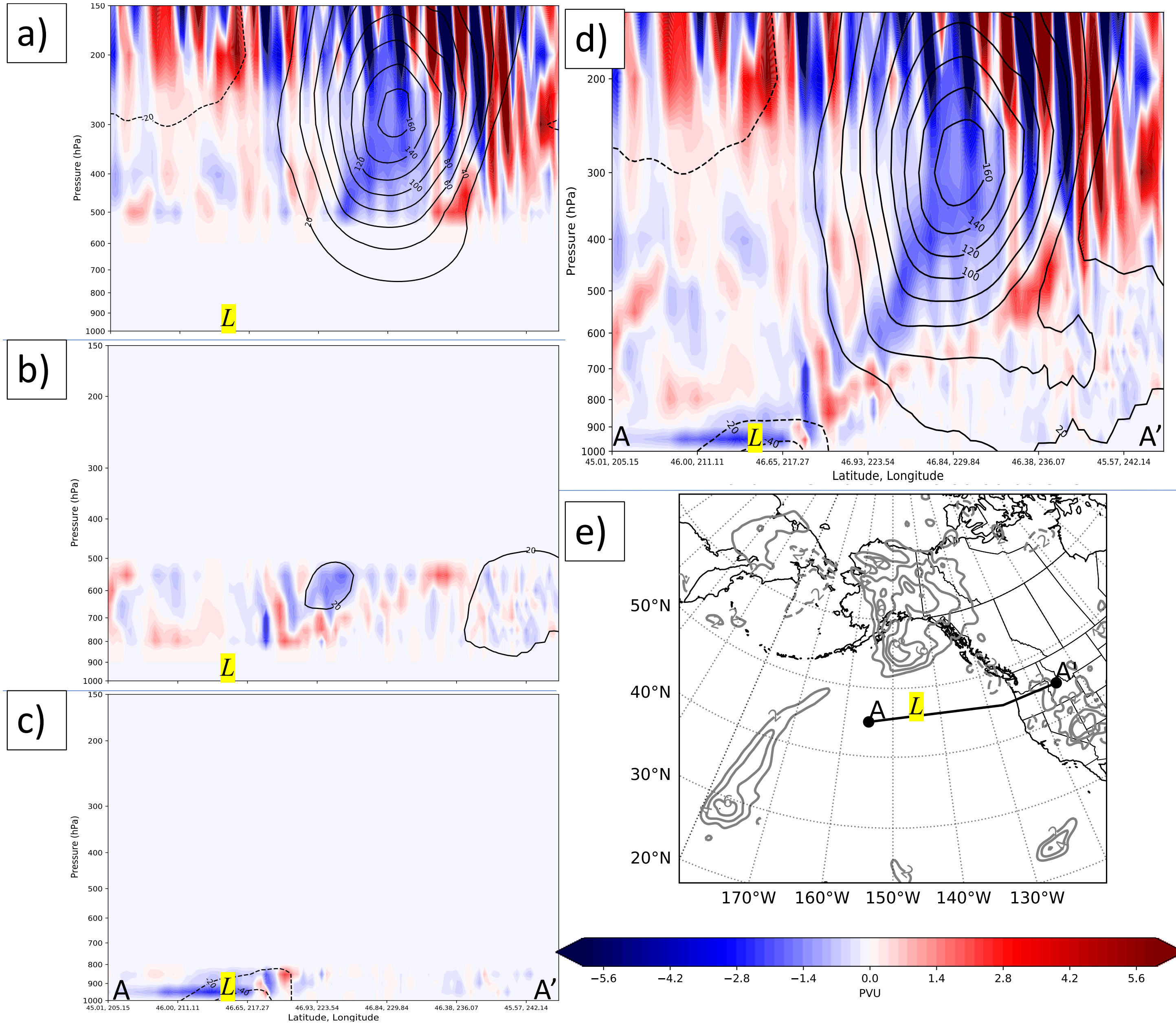

Figure 4.14. As in Fig. 4.13 but valid for 0000 UTC 26 November 2019. Yellow-highlighted “L” indicates the location of the surface geopotential height minimum on both (a). through (e).

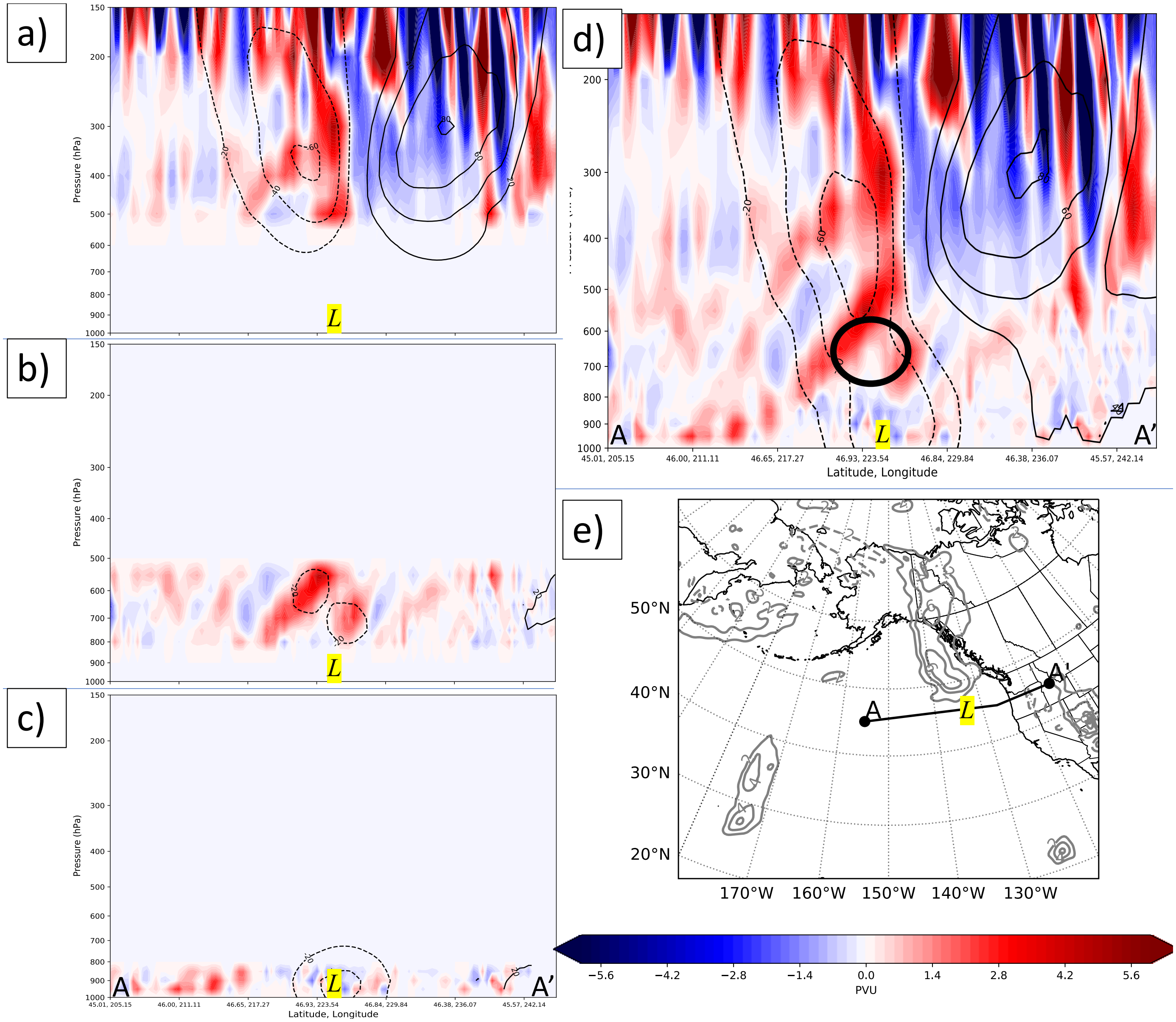

Figure 4.15. As in Fig. 4.14 but valid for 1200 UTC 26 November 2019. (d). Black circle indicates region of locally reduced positive QGPV anomaly.

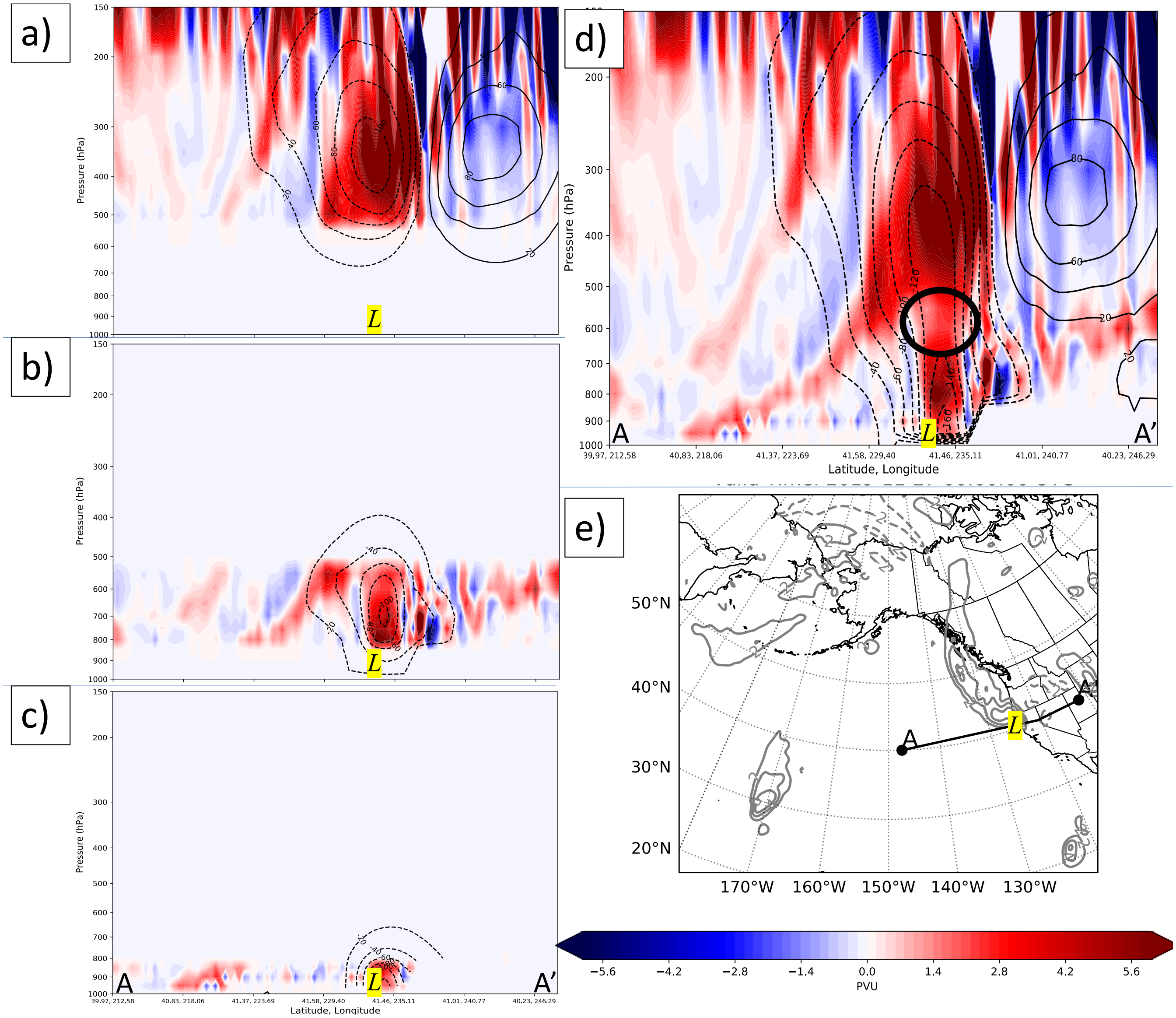

Figure 4.16. As in Fig. 4.15 but valid for 0000 UTC 27 November 2019. (d). Black circle indicates region of locally reduced positive QGPV anomaly.

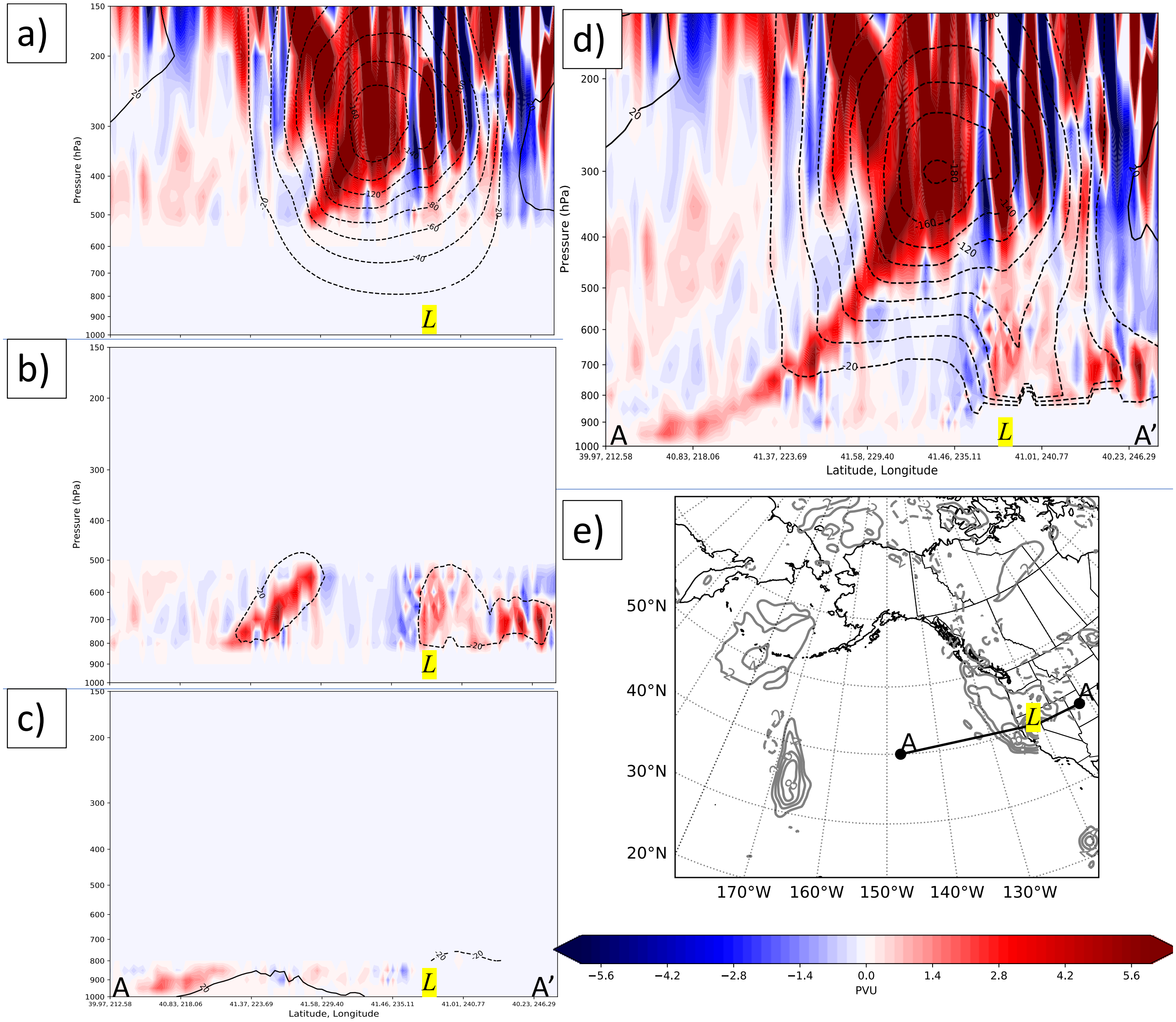

Figure 4.17. As in Fig. 4.16 but valid for 1200 UTC 27 November 2019.

5. INTEGRATED QG MASS DIVERGENCE RESULTS

To begin the analysis of the QG mass divergence, recall that an approximation to equation (38), where the integration proceeds from 950 hPa to 100 hPa, is given by

$$\frac{\partial p_{sfc}}{\partial t} \approx \int_{100}^{950} \frac{\partial \omega}{\partial p} \partial p \tag{38a}$$

with the vertical integration proceeding at 50 hPa increments. In order to assess the effects of QG mass divergence on near-surface pressure tendencies, one needs to know the vertical distribution of QG-omega in the domain surrounding the NV19 storm as shown in Figure 3.1. To solve for this distribution, one can begin with the Q-vector form of the omega equation,

$$\left(\nabla_p^2 + \frac{f_0^2}{\sigma}\frac{\partial^2}{\partial p^2}\right)\omega = -2\nabla_p \cdot \vec{\boldsymbol{Q}} \tag{39}$$

where $\vec{\boldsymbol{Q}}$ is the Q-vector and ∇_p indicates the gradient on a constant pressure surface. By applying an inverse operator on equation (39), one can solve for the distribution of QG-omega based on the divergence of the Q-vectors on a constant pressure surface. If this calculation is performed at 50 hPa increments extending from 950 hPa to 100 hPa, the effects of QG mass divergence in the vertical is able to be related to near-surface pressure tendencies as shown in equation (38a). It is also possible to further partition the QG-omega into portions associated with Q-vectors forcings in discrete layers; UPERT (450 hPa to 100 hPa), MPERT (800 hPa to 500 hPa), and SPERT (1000 hPa to 850 hPa) layers, as was done in Chapter 4 with QGPV inversion. Since the inversion is linear, the sum of the resulting three pieces of QG-omega equates to the full column distribution of QG-omega,

$$\omega_{full} = \omega_{UPERT} + \omega_{MPERT} + \omega_{SPERT}\,. \tag{40}$$

Next, the UPERT, MPERT, and SPERT QG-omega can be inserted into the right hand side of equation (38a) in order to assess the individual contributions of each piece of QG-omega to near-surface pressure tendencies. For example, the UPERT piece of the QG-omega can be calculated using equation (39) by inverting the distribution of Q-vector forcing in the UPERT layer. Then, this distribution of the

QG-omega, which is attributable to forcings for ascent within the 450 hPa to 100 hPa layer, is related to near-surface pressure tendencies driven only by UPERT QG-omega,

$$\frac{\partial p_{sfc_{UPERT}}}{\partial t} \approx \int_{100}^{950} \frac{\partial \omega_{UPERT}}{\partial p} \partial p \, . \tag{41}$$

The same process is then performed using the distribution of QG-omega in both the MPERT and SPERT layers to yield, respectively,

$$\frac{\partial p_{sfc_{MPERT}}}{\partial t} \approx \int_{100}^{950} \frac{\partial \omega_{MPERT}}{\partial p} \partial p \tag{42}$$

and

$$\frac{\partial p_{sfc_{SPERT}}}{\partial t} \approx \int_{100}^{950} \frac{\partial \omega_{SPERT}}{\partial p} \partial p \tag{43}$$

where $\frac{\partial p_{sfc_{MPERT}}}{\partial t}$ and $\frac{\partial p_{sfc_{SPERT}}}{\partial t}$ are the near-surface pressure tendencies associated with QG mass divergence within only the MPERT and SPERT layers, respectively. The near-surface pressure tendencies attributable to QG mass divergence also satisfies the following equality

$$\int_{100}^{950} \frac{\partial \omega_{full}}{\partial p} \partial p \ = \int_{100}^{950} \frac{\partial \omega_{UPERT}}{\partial p} \partial p + \int_{100}^{950} \frac{\partial \omega_{MPERT}}{\partial p} \partial p + \int_{100}^{950} \frac{\partial \omega_{SPERT}}{\partial p} \partial p \tag{43}$$

from which is follows that

$$\frac{\partial p_{sfc_{full}}}{\partial t} = \frac{\partial p_{sfc_{UPERT}}}{\partial t} + \frac{\partial p_{sfc_{MPERT}}}{\partial t} + \frac{\partial p_{sfc_{SPERT}}}{\partial t} . \tag{44}$$

The resulting expression represents the contribution of the integrated QG mass divergence in the 950 hPa to 100 hPa portion of the column, a substantial portion of the total integrated mass divergence, on the near-surface pressure tendencies. The effects of cross-isobaric flow in the boundary layer are ignored in calculations using equation (44). Such flow would act to force pressure rises and decrease the amount of negative near-surface pressure tendencies (pressure falls) forced by the integrated QG mass divergence. Effects of the total integrated QG mass divergence on near-surface pressure tendencies from the 100 hPa to top of the atmosphere (i.e., 0 hPa) are assumed to be negligible and are also ignored.

Finally, the *relative magnitude* of the near-surface pressure tendencies associated with the UPERT, MPERT, and SPERT layers are compared to each other and to the full column near-surface pressure tendencies in order to identify which partitioned layer(s) is(are) contributing the most robust forcing for near-surface cyclogenesis. Areas in which the near-surface pressure tendency is negative indicate areas of rising motion, mass evacuation, height falls, and cyclogenesis. Areas in which the near-surface pressure tendency is positive indicate areas of sinking motion, mass accumulation, height rises, and cyclolysis. In all the following plots of near-surface pressure tendency forced by the full column, UPERT, and SPERT integrated QG mass divergence, values of near-surface pressure tendency are contoured every 2 hPa hour^{-1}, whereas the near-surface pressure tendency forced by the MPERT integrated QG mass divergence is contoured every 1 hPa hour^{-1} due to their magnitudes never equaling more than +/-2 hPa hour^{-1}.

At 12 hours prior to formation, 1200 UTC 25 November 2019, a couplet of positive and negative near-surface pressure tendencies forced by the full column (950 hPa to 100 hPa) integrated QG mass divergence straddled the development region of the NV19 storm, with near-surface pressure tendencies of -2 hPa hour^{-1} occurring to its southeast and near-surface pressure tendencies of +2 hPa hour^{-1} occurring to its northwest (Fig. 5.1a). Both the UPERT and MPERT QG-omega near-surface pressure tendencies in the vicinity of the NV19 storm were weaker than +/-2 hPa hour^{-1} and were, therefore, not significantly influencing development at this time (Fig. 5.1b; Fig. 5.1c). A nearly identical distribution of near-surface pressure tendencies associated with the SPERT integrated QG mass divergence compared to the full column integrated QG mass divergence was situated around the NV19 development region (Fig. 5.1a; Fig. 5.1d). This signifies that the integrated QG mass divergence within the SPERT layer was describing roughly all of the total near-surface pressure tendencies associated with integrated QG mass divergence in the full column prior to storm development.

As the storm began to form as a weak (~1024 hPa) cyclone at 0000 UTC 26 November, a more disorganized region of near-surface pressure tendencies established themselves around the cyclone with the same spatial orientation and +/-2 hPa hour^{-1} magnitude as 12 hours prior (Fig. 5.1a; Fig. 5.2a). The

UPERT integrated QG mass divergence was forcing weak, less than +/-2 hPa hour^{-1} near-surface pressure tendencies for the second consecutive analysis time (Fig. 5.2b). The MPERT integrated QG mass divergence was forcing near-surface pressure rises of around +1 hPa hour^{-1} to the northwest of the weak cyclone, potentially contributing to the positive near-surface pressure tendencies in the same region as described by the full column integrated QG mass divergence (Fig. 5.2a; Fig. 5.2c). The integrated QG mass divergence within the SPERT layer was contributing almost exclusively to the near-surface pressure falls to the southeast of the cyclone, as the integrated QG mass divergence within this layer was the only partitioned-layer integrated QG mass divergence to be forcing near-surface pressure falls with the same magnitude as those analyzed by the full column (Fig. 5.2d).

While the cyclone began rapidly intensifying, at 1200 UTC 26 November, a well-defined couplet of near-surface pressure falls and rises encircled the NV19 storm in a similar fashion as 1200 UTC 25 November, but with stronger magnitude (Fig. 5.3a). Near-surface pressure rises increased more than 300% from +2 hPa hour^{-1} to +8 hPa hour^{-1} to the west/northwest of the cyclone center while near-surface pressure falls increased more than 100% from -2 hPa hour^{-1} to -4 hPa hour^{-1} to the east/southeast of the storm. A broad region of near-surface pressure rises forced by the UPERT integrated QG mass divergence extended from near the storm center to the southern Alaska (Fig. 5.3b). This region presumably owes its existence to the developing upper front and subsequent tropopause subduction occurring over the same spatial domain at this analysis time. The integrated QG mass divergence within the MPERT layer again described near-surface pressure tendencies of magnitude +/-1 hPa hour^{-1}, with the near-surface pressure falls occurring well ahead of the surface cyclone as it rapidly deepened (Fig. 5.3c). The main contributor to the full column near-surface pressure tendencies was once again the SPERT integrated QG mass divergence, as this mass divergence forced all of the near-surface pressure falls ahead of the storm and 75% of the near-surface pressure rises to the northwest of the storm (Fig. 5.3d).

The couplet of near-surface pressure tendencies maintained its characteristic distribution and slightly strengthened as the storm approached landfall at 0000 UTC 27 November, with near-surface pressure rises increasing from +8 hPa hour^{-1} to +10 hPa hour^{-1} and near-surface pressure falls increasing more than 150% from -4 hPa hour^{-1} to -10 hPa hour^{-1} (Fig. 5.4a). This marked the first time where the spatial extent of the near-surface pressure falls was greater than the near-surface pressure rises. Disorganized and relatively weak near-surface pressure rises forced by the integrated QG mass divergence in both the UPERT and MPERT layer was occurring to the west/northwest of the cyclone (Fig. 5.4b; Fig. 5.4c). 80% of the full column near-surface pressure rises and all of the near-surface pressure falls were described by the integrated QG mass divergence within the SPERT layer, once again solidifying that the SPERT integrated QG mass divergence was commanding near-surface pressure tendencies and contributing an overwhelming amount to the development of the NV19 storm (Fig. 5.4d).

For the final analysis time, at 1200 UTC 27 November, disorganization of the near-surface pressure tendencies characterized the vicinity of the NV19 storm, but very broad and weak, -2 hPa hour^{-1}, near-surface pressure falls were situated over the storm and along a line extending to its southeast (Fig. 5.5a). Following the previous analysis time, the near-surface pressure tendencies from the integrated QG mass divergence within the UPERT and MPERT layer were far removed from the cyclone and relatively weak (Fig. 5.5b; Fig. 5.5c). A spatially small region of near-surface pressure falls forced by the integrated QG mass divergence within the SPERT layer was situated almost directly over the NV19 storm, with this being the only region of near-surface pressure tendencies forced by the SPERT integrated QG mass divergence within the vicinity of the cyclone (Fig. 5.5d).

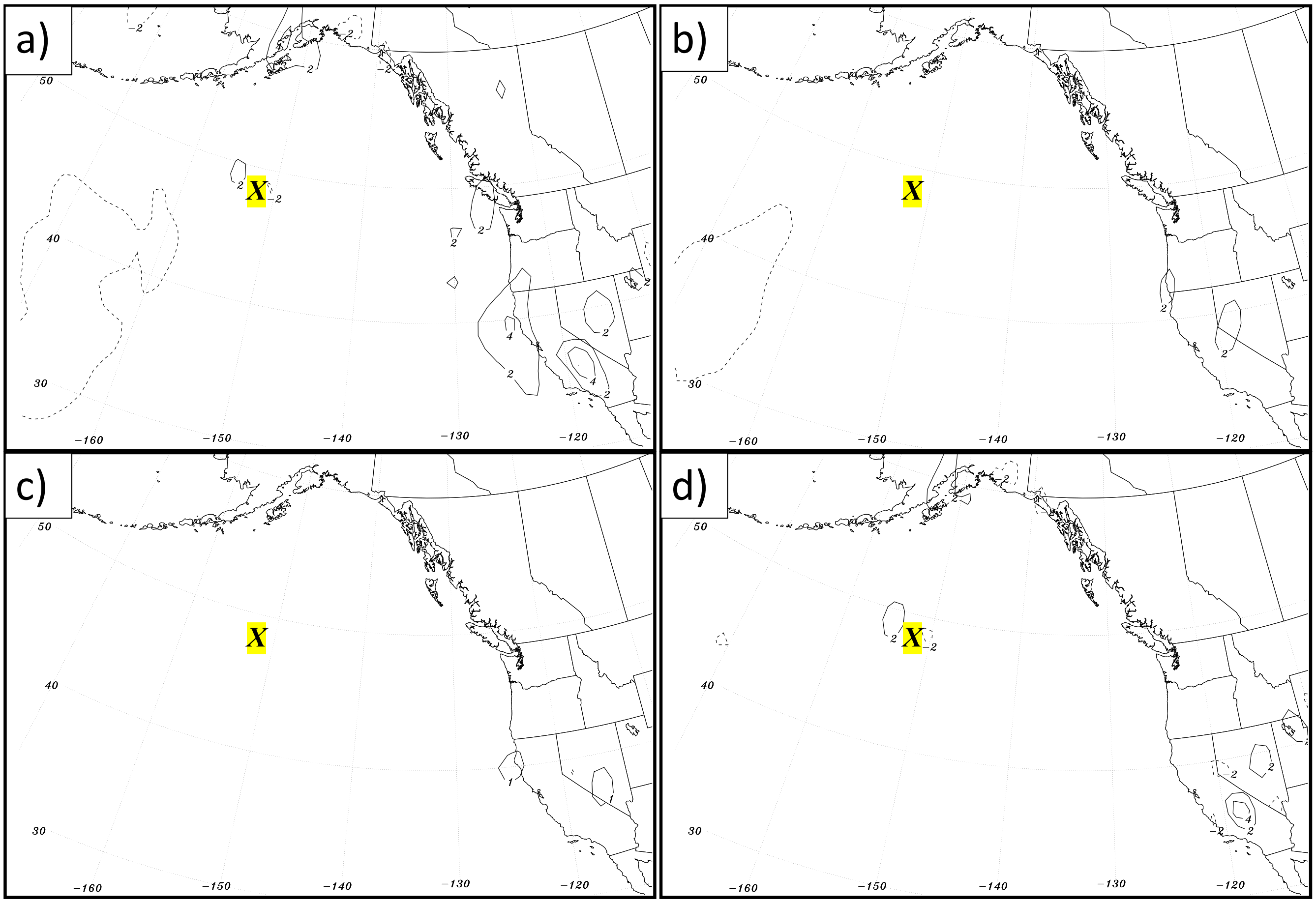

Figure 5.1. Eulerian rate of change in surface pressure associated with vertical motions forced by $\vec{\boldsymbol{Q}}$ convergence within layers defined from a) 950 hPa to 100 hPa, b) 450 hPa to 100 hPa, c) 800 hPa to 500 hPa, and d) 950 hPa to 850 hPa valid at 1200 UTC 25 November 2019. Eulerian rate of change in surface pressure is contoured in hPa hour^{-1} every 2 hPa hour^{-1} with dashed contours indicating negative values and rising motion and solid contours indicating positive values and sinking motion at the top of the column. Note, for c), Eulerian rate of change in surface pressure is contoured in hPa hour^{-1} every 1 hPa hour^{-1}. Yellow-highlighted "X" indicates the surface development area of the November 2019 storm. A 9-point smoother was applied to the data to enhance readability.

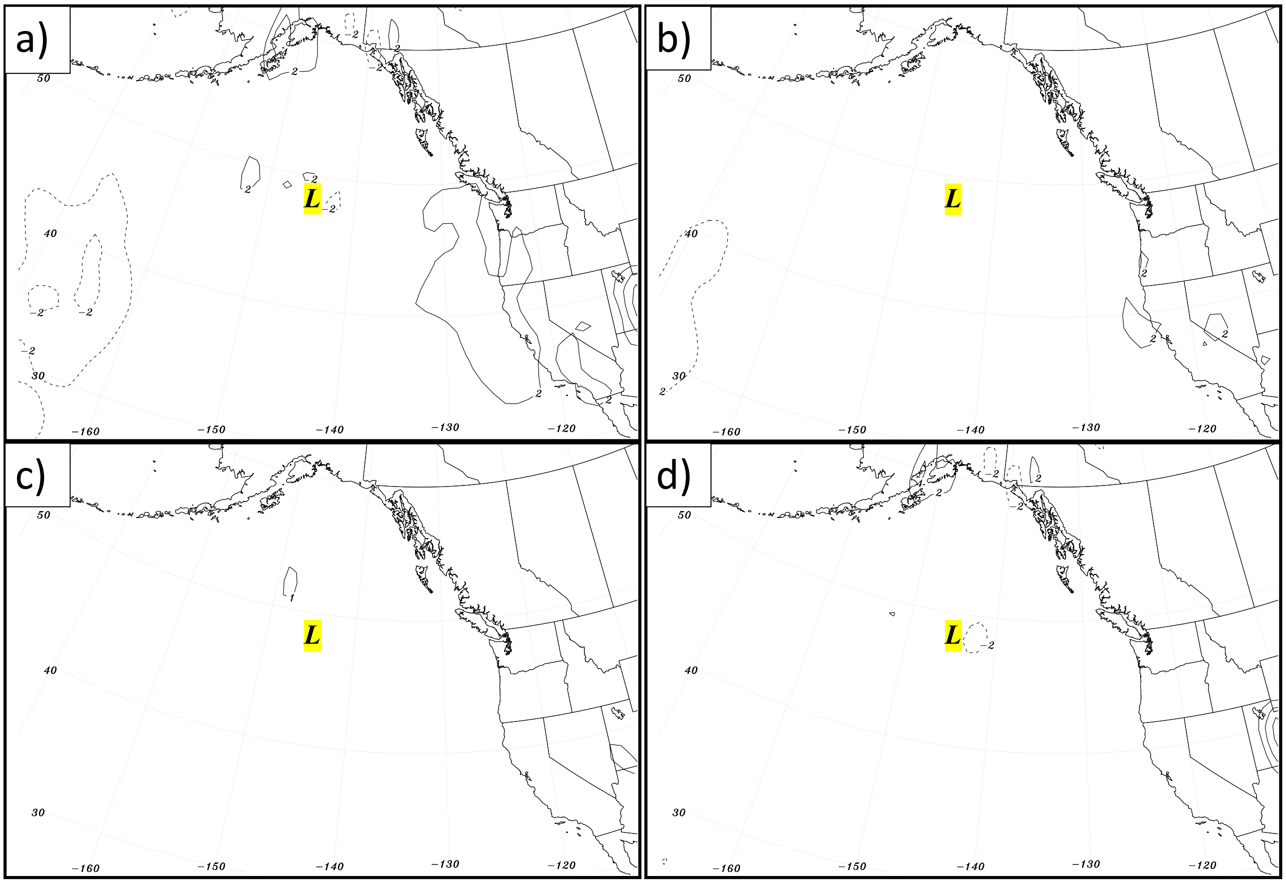

Figure 5.2. As in Fig. 5.1 but for 0000 UTC 26 November and with a yellow-highlighted “L” denoting the location of the 950-hPa central sea-level pressure minimum. Note, for c), Eulerian rate of change in surface pressure is contoured in hPa hour^{-1} every 1 hPa hour^{-1}.

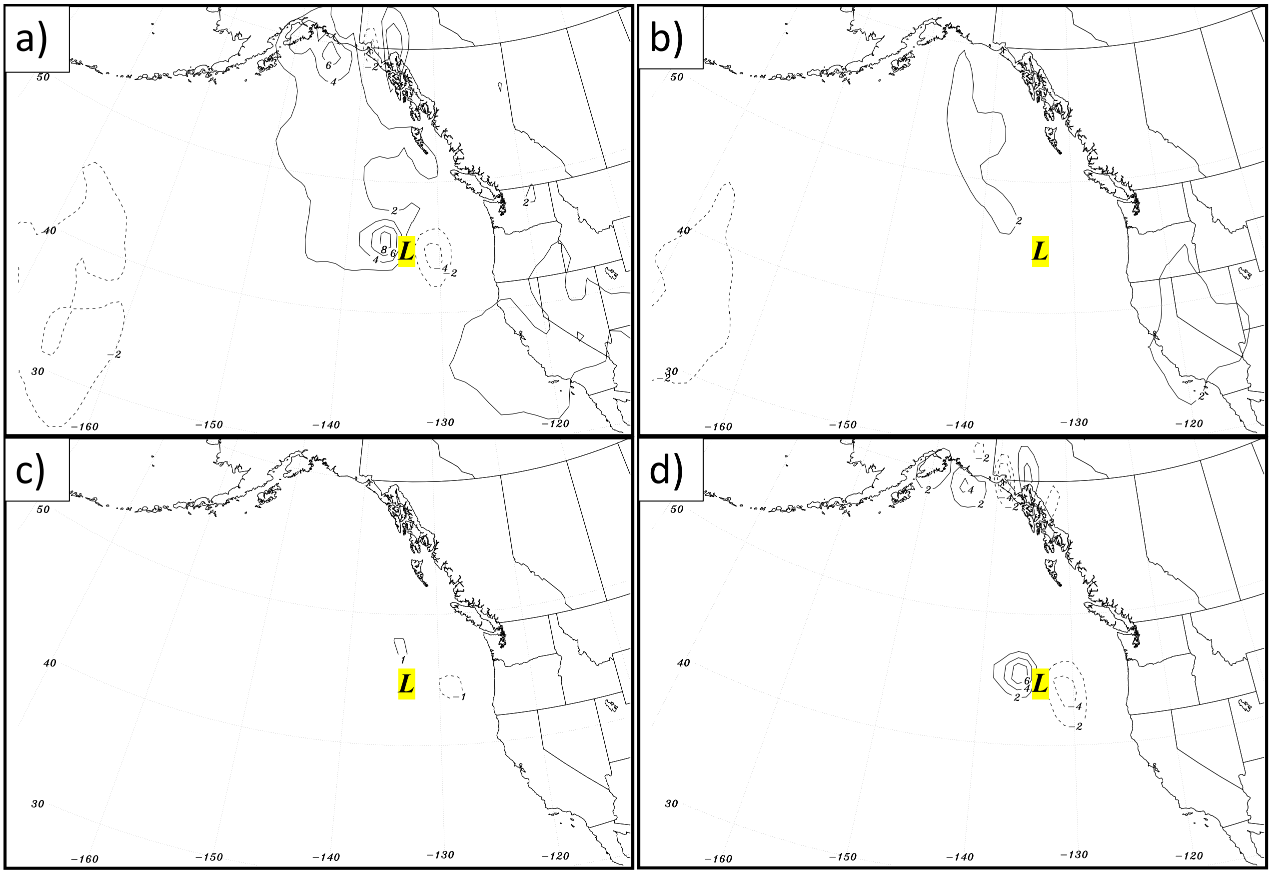

Figure 5.3. As in Fig. 5.2 but for 1200 UTC 26 November. Note, for c), Eulerian rate of change in surface pressure is contoured in hPa hour^{-1} every 1 hPa hour^{-1}.

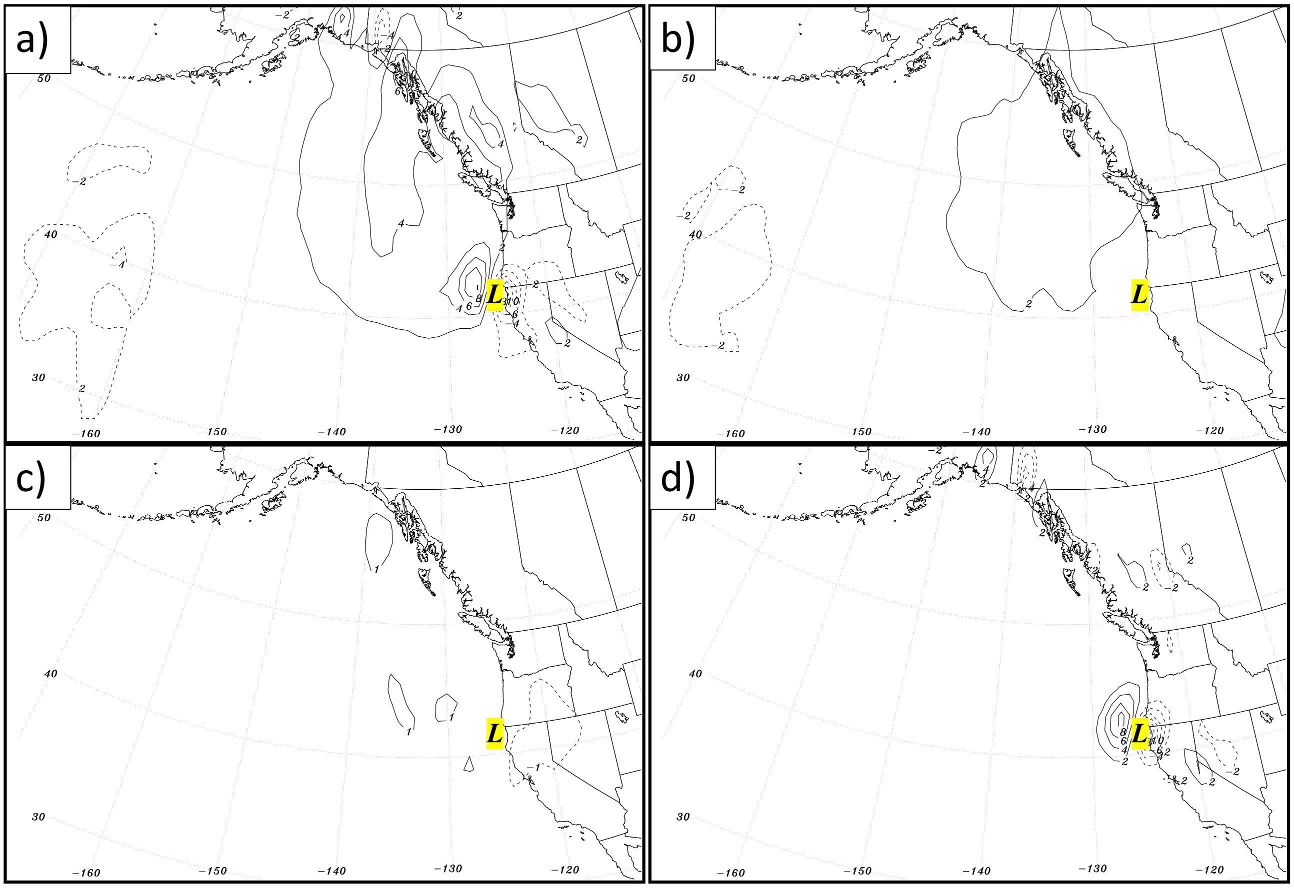

Figure 5.4. As in Fig. 5.3 but for 0000 UTC 27 November. Note, for c), Eulerian rate of change in surface pressure is contoured in hPa hour^{-1} every 1 hPa hour^{-1}.

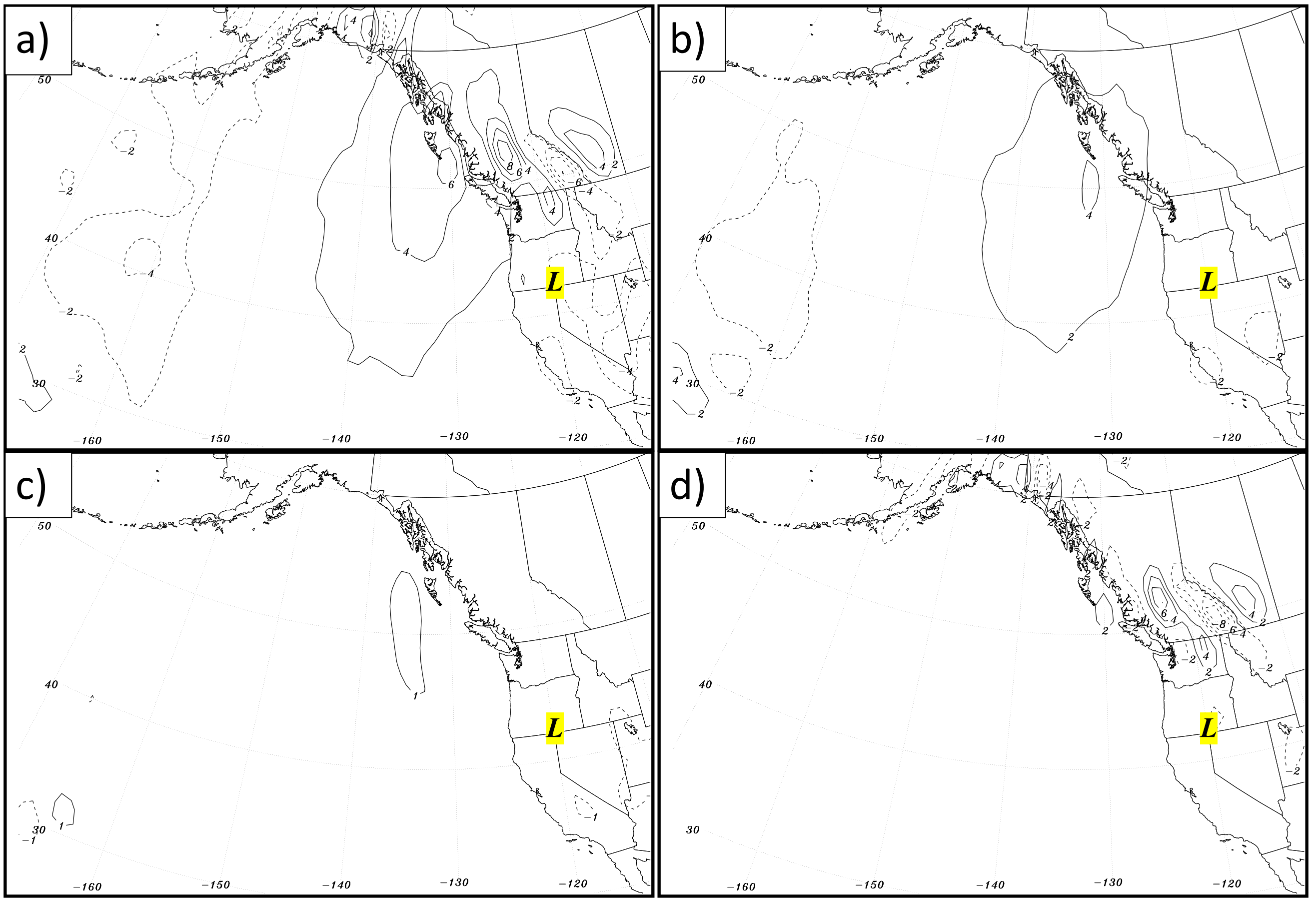

Figure 5.5. As in Fig. 5.4 but for 1200 UTC 27 November. Note, for c), Eulerian rate of change in surface pressure is contoured in hPa hour^{-1} every 1 hPa hour^{-1}.

6. SUMMARY AND CONCLUSIONS

6.1 Utilizing the QGPV inversion lens

The perturbations associated with low-level positive QGPV anomalies almost completely described low-level negative height anomalies throughout the lifecycle of the NV19 storm, as discussed in Chapter 4.1. This signifies that the lower levels of the atmosphere were the most influential in supporting this EC event. Type B cyclones involve the coupling of lower-level baroclinicity with a pre-existing upper-level feature (Petterssen and Smebye 1971), which was shown to define this storm as outlined in Chapter 2.1. In such a robust event of predominantly Type B cyclogenesis, it is perplexing that the upper-level precursor to development, which upon inspection is incredibly pronounced, would be so delayed in impacting cyclogenesis and would not have a substantial impact on surface development until 6 hours *after* the time of maximum development.

It is clear from the diagnosis of the inverted HA that the partitioned layer defined by SPERT contributes anywhere from 77% to 90% of the 950 hPa HA from the inversion of QGPV of the NV19 storm, with MPERT contributing up to 22% of the 950 hPa HA anomalies and UPERT having negligible contributions (Table 6.1). In relating the partitioned layers to distinguishable features, boundary-layer potential temperature and QGPV anomalies were the primary features that promoted negative HA at 950 hPa and near-surface development, mid-tropospheric QGPV associated with latent heat release was an accompanying process in promoting near-surface development, and upper-level tropopause undulations of (QG)PV were an insignificant process in promoting near-surface development (Petterssen and Smebye 1971). This means that the main driver for surface development during the lifecycle of the NV19 storm were these boundary-layer potential temperature and QGPV anomalies. The rest of this section will attempt to explain why the mid- and especially the low-levels dwarfed the upper-levels in terms of forcing for surface development from the QGPV inversion lens.

Foremost, the biggest limitation of the usefulness of (QG)PV is arguably its lack of considering diabatic heating influences (i.e., Charney and Stern 1962; Hoskins et al. 1985; Davis and Emanuel 1991; Hakim et al. 1996), which, when inverted, were shown to dwarf the mid- and upper-level QGPV perturbations in Chapter 4.2. It has been shown that when using a PV-thinking framework to describe cyclogenesis, diabatic heating (latent heating in particular) can play a substantial role in providing a source of low-level (QG)PV generation and allowing for the coupling of surface and upper-level (QG)PV features (Davis and Emanuel 1991; Stoelinga 1996; Plant et al. 2003; Businger et al. 2005). One form of the isentropic PV is defined as in equation (2) in Chapter 1. If one applies the isobaric Lagrangian operator to equation (2) to determine the Lagrangian time rate of change of PV, and neglects the horizontal components, the vertical component of the Lagrangian time rate of change of PV is described as

$$\frac{d}{dt}(PV) \approx -g(\zeta + f)\frac{\partial \dot{\theta}}{\partial p} \tag{45}$$

where $\dot{\theta}$ is the diabatic heating rate. Equation (45) states that PV is increased where the vertical gradient of diabatic heating is negative, which would strengthen a vortex if a positive vertical gradient of diabatic heating was situated above that vortex. Likewise, equation (45) states that PV is decreased where the vertical gradient of diabatic heating is positive, which would weaken a vortex if a negative vertical gradient of diabatic heating was situated above that vortex.

Based on the WRF model simulation of the NV19 storm, a region of strong diabatic heating emerges around 850 hPa above the storm center at 0000 UTC 26 November and strengthens while expanding throughout the mid- to lower-troposphere during the rapid deepening of the storm and its approach to the west coast of the United States (Figs. 4.9-4.12). For all times when diabatic heating was occurring, the maximum in diabatic heating, which was most pronounced at 1200 UTC 26 November, was located downstream and to the northeast of the surface cyclone. Below this region of diabatic heating, according to equation (45), PV will be increasing with time as the vertical derivative of the diabatic heating is negative making the term on the right-hand side of equation (45) positive. This is depicted as a low-level maximum in QGPV which is centered around 800 hPa as the storm is beginning to develop (Figs. 4.14b-d) and strengthens while expanding towards the surface, remaining situated below 700 hPa for most of the lifecycle of the NV19 storm (Figs. 4.15b-d; Figs. 4.16b-d; Figs. 4.17b-d). Regions of positive maxima in QGPV are associated with negative height anomalies at the surface and support development (Figs. 4.14-4.17). Above this region of intense diabatic heating, PV will be decreasing with time as the vertical derivative of the diabatic heating is positive making the term on the right-hand side of equation (45) negative. The decrease in QGPV as explained by the vertical gradient of diabatic heating is evident at 1200 UTC 26 November and 0000 UTC 27 November, where a reduced area of positive QGPV anomaly is noted by the open black circles (Figs. 4.10-4.11.; 4.15d; & 4.16d).

Equation (45) could explain the clear separation between the upper- and lower-level QGPV anomalies, which both are associated with negative height anomalies that remain relatively isolated from each other throughout the rapid deepening period of the NV19 storm (Figs. 4.15-4.16). These two QGPV anomalies have roughly equal magnitude and height anomalies, and yet the height anomalies associated with the upper-level QGPV anomaly do not penetrate below 700 hPa until the very last analysis time, 1200 UTC 27 November. This is the only analysis time at which the positive upper-level QGPV begins to have a notable effect on the surface development (Fig. 4.17). Likewise, the height anomalies associated with the low-level QGPV anomaly do not penetrate higher than 700 hPa throughout the storm's lifecycle. From equation (45), the vertical distribution of the diabatic heating could be such that the upper- and lower-tropospheric QGPV anomalies are unable to amalgamate during the NV19 storm development and might explain why the robust upper-level QGPV undulation is unable to impact surface development according to the HA associated with the QGPV inversion. The cross sections in Fig. 6.1 illustrate how diabatic heating could be producing this clear separation between the upper- and lower tropospheric (QG)PV anomalies, with the areal extent of the cross sections shown in Fig. 6.2. Throughout the lifecycle of the PV undulation associated with the NV19 storm, the distribution of diabatic heating occurs directly underneath and beyond the periphery of the PV undulation with the maxima in diabatic heating remaining below 800 hPa for every time between 0000 UTC 26 November 2019 to 0000 UTC 27 November except for 1200 UTC 26 November, the start of the 12 hour rapid deepening period (Fig. 6.1a-e). The diabatic heating distribution is such that the maximum in diabatic heating is characterized by anomalously higher values of PV below it and anomalously lower values of PV above it. This distribution hints that the PV undulation and the diabatic heating are coupled throughout this event of EC, resulting in continuous erosion of PV above the diabatic heating maxima and continuous generation of PV below the diabatic heating maxima, and producing the clear signal of low-level forcing dominance on cyclogenesis throughout the lifecycle of the storm. Opposing this theory, a diabatic heating anomaly is also associated with locally reduced static stability, which would increase the penetration depth of the PV anomaly and encourage upper- and lower-level PV coupling. However, any lower-level PV anomaly generated by the diabatic heating is associated with an increase in static stability in the lower troposphere, which corrects for this reduction in static stability and, coupled with the previous analysis of the height anomalies associated with QGPV perturbations, seems to mask the effects of this more mid-level diabatic heating.

The diabatic heating played a comparable role in the development at 950 hPa as the UPERT and MPERT perturbations. In two of the five analysis times, the height anomalies from the diabatic heating term were larger in magnitude than the height anomalies from the UPERT and MPERT layers combined, while being comparable to the height anomalies from the MPERT layer during the other three analysis times (Figs. 4.7-4.11). This proves that the diabatic heating effects involved in this storm were such that they had the same effect on surface development as all of the QGPV in the 800 hPa to 100 hPa layer. The *secondary* effect of the diabatic heating was the generation of low-level QGPV and erosion of mid-level QGPV which produced the distinct separation between the upper- and lower-level QGPV.

As discussed above, the relative magnitude of the erosion of the mid-level QGPV indicated by the vertical gradient in diabatic heating could have been the reason that the associated height anomalies from the upper- and lower-level QGPV anomalies never overlapped. The continued separation of the two QGPV anomalies by the diabatic heating would reduce the potential for phase locking and mutual amplification as discussed in Hoskins et al. (1985). Phase locking discourages the upper- and lower-level PV anomalies from propagating away from each other through the location of the advection of the lower-level PV by the upper-level PV anomaly and the location of the advection of upper-level PV by the lower-level PV anomaly (Fig. 6.2). Mutual amplification begins when upper- and lower-level PV anomalies become phase locked and the PV advection produced by their circulations strengthen the PV anomaly at the opposite atmospheric level. The associated upper- and lower-level circulations from the respective QGPV anomalies during the lifecycle of the NV19 storm might be locally diminished in the region of reduced positive QGPV anomaly as annotated in Figs. 4.15d & 4.16d and this weakening could possibly diminish upper- and lower-level QGPV anomaly mutual amplification associated with phase-locking.

To test this claim, the inverted winds associated with the height anomalies from the inversion of the QGPVP were calculated and visualized on top of representative distributions of the QGPVP within the SPERT, MPERT, and UPERT layers as depicted in Fig. 6.3 from Hoskins et al. (1985). Only the period from 0000 UTC 26 November to 0000 UTC 27 November 2019 will be assessed as there is no mutual amplification signal from any partitioned level before and after this period.

Starting at 0000 UTC 26 November, the first time of storm development, the overall pattern of potential mutual amplification was disorganized. There was an extension of the SPERT inverted winds advecting mid-level QGPVP and a penetration of the UPERT inverted winds advecting boundary-level potential temperature anomalies, but both signals were removed from the 950 hPa geopotential height minimum (Figs. 6.4b; 6.4c). There was no extension of the SPERT inverted winds advecting upper-level QGPVP (Fig. 6.4a). At the beginning of the most rapid development period at 1200 UTC 26 November, the SPERT inverted winds were mutually amplifying mid-level QGPVP to the immediate northwest of the 950 hPa cyclone center, but these winds did not extend into the upper levels (Figs. 6.5a; 6.5b). The UPERT inverted winds were advecting positive boundary-level potential temperature anomalies along the northern edge of the warm sector; however, this signal was weaker than the SPERT inverted winds advecting mid-level QGPVP (Fig. 3.3; Fig. 6.5b). Along with this, the main area of boundary-level potential temperature advection was occurring north of the eastward track of the 950 hPa cyclone (Fig. 6.5c).

As the storm neared landfall at 0000 UTC 27 November, a well-established mutual amplification pattern was occurring between the SPERT inverted winds and the mid-level QGPVP (Fig. 6.6b). As noted at the previous analysis times, mutual amplification of the SPERT inverted winds advecting upper-level QGPVP was not occurring (Fig. 6.6a). Also, during this final analysis time, positive boundary-level potential temperature anomalies downstream of the 950 hPa cyclone center were being advected northward by the UPERT inverted winds (Fig. 6.6c). This UPERT inverted wind advection was focused in the heart of the low-level warm anomaly, indicating mutual amplification by the UPERT inverted winds on the boundary-level potential temperature anomaly at this time, a first for the entire analysis period.

From this assessment of mutual amplification, the UPERT inverted winds did not significantly mutually amplify boundary-level potential temperature anomalies until the storm was concluding its rapid development phase. Even when this mutual amplification occurred, only the northward advection of low-level positive QGPVP, represented by positive boundary-level potential temperature anomalies, was apparent, meaning that a complete couplet of mutual amplification as shown in Fig. 6.3 was not present. This supports the notion that the projection of upper-level winds onto low-level QGPV anomalies represented weak to modest mutual amplification at the end of the rapid intensification period, and that this delay in the signal of mutual amplification may have been the result of mid-level QGPV erosion throughout the lifecycle of the storm.

6.2 Utilizing the integrated QG mass divergence lens

Adding to the conclusions drawn in Chapter 6.1, the analysis of the NV19 storm from the QG-omega lens provides a similar story of lack of support for the forcing of surface development from the UPERT layer. Near-surface pressure rises well behind the NV19 storm were the only pressure tendencies forced by the integrated QG mass divergence within the UPERT layer; this distribution of integrated QG mass divergence did not describe any near-surface pressure tendencies in the vicinity of the cyclone (Table 6.1). The integrated QG mass divergence within the MPERT layer contributed the least to both near-surface pressure rises and near-surface pressure falls, most notably describing none of the near-surface pressure falls ahead of the NV19 storm track.

The near-surface pressure tendencies associated with the integrated QG mass divergence within the SPERT layer described all of the total near-surface pressure falls ahead of the NV19 storm (Table 6.1). A rapid increase in near-surface pressure tendencies from the integrated QG mass divergence in the full column occurred between 1200 UTC 26 November and 0000 UTC 27 November, which was captured in the pressure tendencies from the SPERT integrated QG mass divergence. The rapid increase during this period coincides with the extreme surface deepening of more than 20 hPa as the storm approached landfall. This signifies that forcings for development associated with the integrated QG mass divergence concentrated from 1000 hPa to 850 hPa using the basic state variable lens were much more influential on surface cyclogenesis than forcings for development associated with the integrated QG mass divergence from 800 hPa and above, coinciding with the conclusions reached from the QGPV inversion lens.

6.3 Final discussion

A consensus was reached between both the QGPV inversion and the integrated QG mass divergence lenses in terms of the lack of support from forcings within the UPERT layer. Perhaps more perplexing is that both analysis methods identified the SPERT layer as almost completely explaining the forcings for the rapid deepening of this record-setting storm from late November 2019. This cyclogenesis event featured the development of an intense upper front, forcing tropopause subduction and an intrusion of high-PV, stratospheric air as low as 750 hPa as well as strong diabatic heating maxima centered between 800 hPa and 600 hPa. Yet, forcings in the lowest 150 hPa of the atmosphere overshadowed this deep tropopause undulation and diabatic heating, describing up to 90% of the 950 hPa HA associated with the inversion of QGPV anomalies and all of the near-surface pressure falls associated with the integrated QG mass divergence. Such a strong signal in both the PV and QG-omega lenses provides substantial support for the conclusion that low-level forcings drove this intense cyclogenesis event.

This case of Type B cyclogenesis also incorporated characteristics of a Type A cyclogenesis event, in which baroclinicity in the lower troposphere dominates cyclogenetic dynamics, along with characteristics of a Type C cyclogenesis event, in which midlevel latent heating dominates cyclogenetic dynamics (Petterssen and Smebye 1971; Plant et al. 2003). While latent and diabatic heating effects influenced the cyclogenesis of the NV19 storm, this heating was focused in the low-levels of the atmosphere, such that low-level PV anomalies, along with low-level integrated QG mass divergence, contributed the most to cyclogenetic dynamics in the form of 950 hPa HA and near-surface pressure tendencies, respectively. The NV19 is curious in that it combined the dominant low-level amplifying frontal wave characteristic of Type A cyclones, the coupling of lower-level baroclinicity with a pre-existing upper-level feature characteristic of Type B cyclones, and the PV generation and destruction effects forced by midlevel latent heating characteristic of Type C cyclones (Petterssen and Smebye 1971; Plant et al. 2003). This complex storm exhibited aspects of all three modes of cyclogenesis during its lifecycle, making identification of the level of predominant forcing for cyclogenesis an important consideration.

Applying these methods of QGPV inversion and calculations of integrated QG mass divergence to a past case of extreme cyclogenesis is no doubt a vital effort in the quest to understand the process of cyclogenesis itself. The ability to identify the predominant levels for the forcing of cyclogenesis allows for a detailed analysis of the dynamics involved within these EC events. Both the QGPV inversion and QG-omega techniques, demonstrated within this thesis, offer consistent determination of these levels along with potentially providing some insight into why certain levels provide more significant forcings for cyclogenesis than others. More work is still needed to conclusively explain why the lower levels of the NV19 storm dominated throughout the lifecycle of this storm, though this thesis has offered some speculations. The identification and analysis of storms whose predominant influence is low-level versus upper-level could yield additional new insights into the varied and dramatic process that is cyclogenesis.

Time	**UPERT (%)**	**MPERT (%)**	**SPERT (%)**
1200 UTC 25 November	0	***100***	0
	0	0	***100***
0000 UTC 26 November	0	6	***90***
	0	0	***100***
1200 UTC 26 November	0	10	***90***
	0	~0	***~100***
0000 UTC 27 November	2	21	***77***
	0	0	***100***
1200 UTC 27 November	9	22	***83***
	0	0	***100***

Table 6.1. Comparison of percent contribution to negative near-surface pressure tendencies for 950 hPa cyclogenesis for 12-hour increments during the lifecycle of the late November 2019 West Coast storm. Gray cells indicate percent contributions from QGPV inversion. White cells indicate percent contributions from the vertical derivative of QG-omega. Maximum contributions are in red, italicized, and bolded.

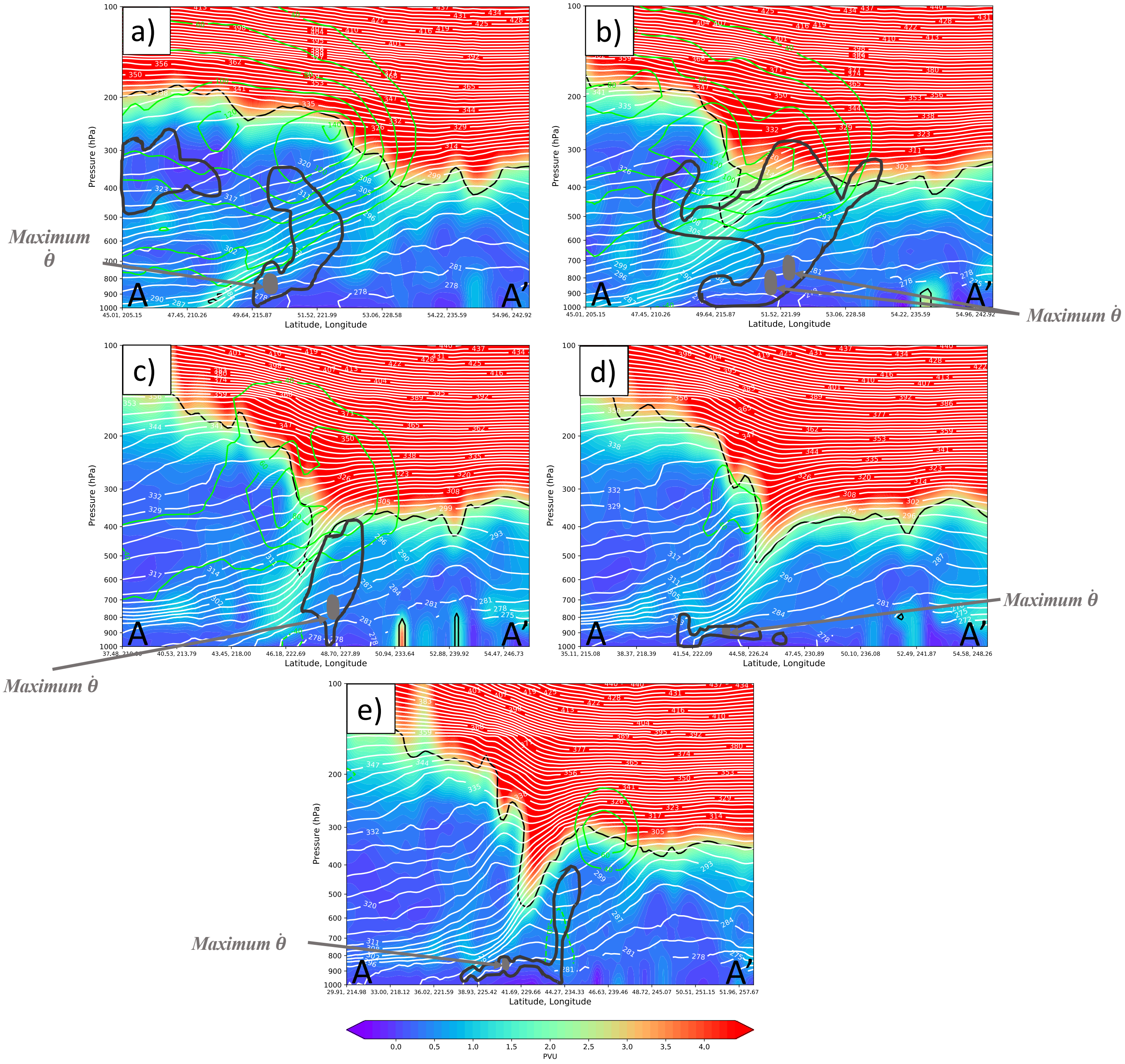

Figure 6.1. Cross sections of the evolution of the potential vorticity undulation associated with the November 2019 storm. Depicted on cross sections is potential vorticity (PVU, shading), potential temperature (Kelvin, white contours) and winds normal to the cross section (knots, green contours) with positive normal winds represented by full contours and negative normal winds represented by dashed contours. The 2 PVU line is contoured in black to indicate the location of the dynamical tropopause. Diabatic heating ($\dot{\theta}$) distribution is contoured in dark gray with the maximum in diabatic heating

indicated by a lighter gray oval. Valid for (a.) 0000 UTC 26 November 2019, (b.) 0600 UTC 26 November, (c.) 1200 UTC 26 November, (d.) 1800 UTC 26 November, and (e.) 0000 UTC 27 November.

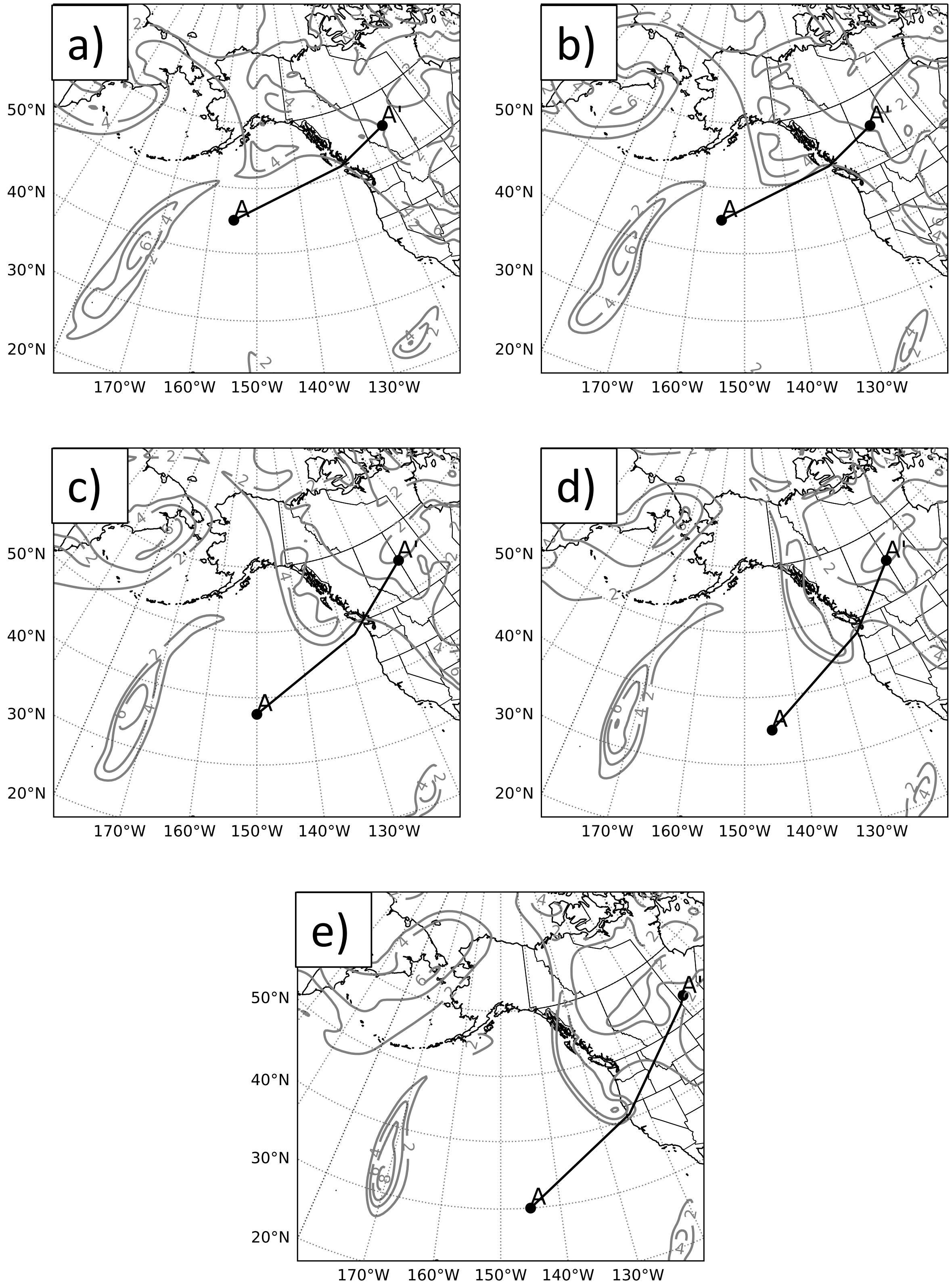

Figure 6.2. Areal extent of the cross sections shown in Fig. 6.1. Potential vorticity at 300 hPa is contoured in gray every 2 PVU with the bounds of the cross section displayed by the black line extending from A to

A’. Valid for (a.) 0000 UTC 26 November 2019, (b.) 0600 UTC 26 November, (c.) 1200 UTC 26 November, (d.) 1800 UTC 26 November, and (e.) 0000 UTC 27 November. Note in (e.) that the cross section is drawn through the maximum in 300 hPa potential vorticity off the coast of northern California despite the apparent neglect of this maximum.

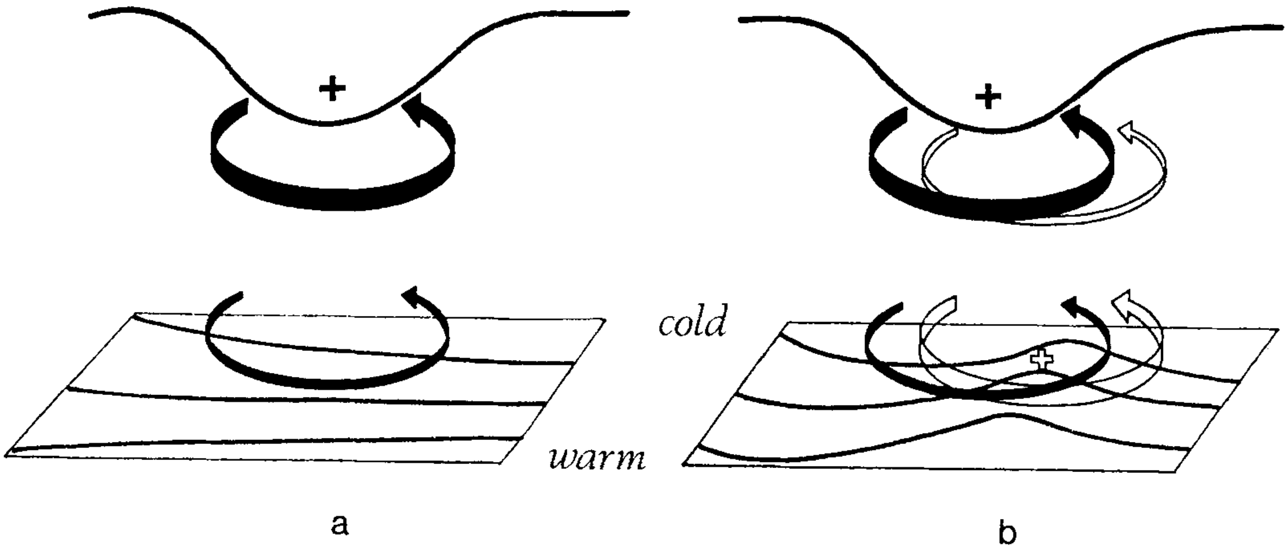

Figure 6.3. Adopted from Hoskins et al. (1985). Schematic of an upper-level potential vorticity (PV) anomaly interacting with a low-level baroclinic zone, demonstrating the mutual amplification that occurs upon superposition of upper- and lower-level PV anomalies. (a). An upper-level positive PV anomaly, indicated by the solid plus sign, and its associated circulation as shown by the solid arrows interacting with a low-level baroclinic zone. The strength of the PV-anomaly-associated circulation is indicated by arrow width. (b). A low-level positive potential temperature anomaly, indicated by the open plus sign, and its associated circulation shown by the open arrows interacting with the upper-level PV anomaly. The strength of the potential-temperature-anomaly-associated circulation is indicated by arrow width. As the two anomalies become phase locked, as is shown in depicted in (b.), the associated cyclonic circulations act to amplify each other.

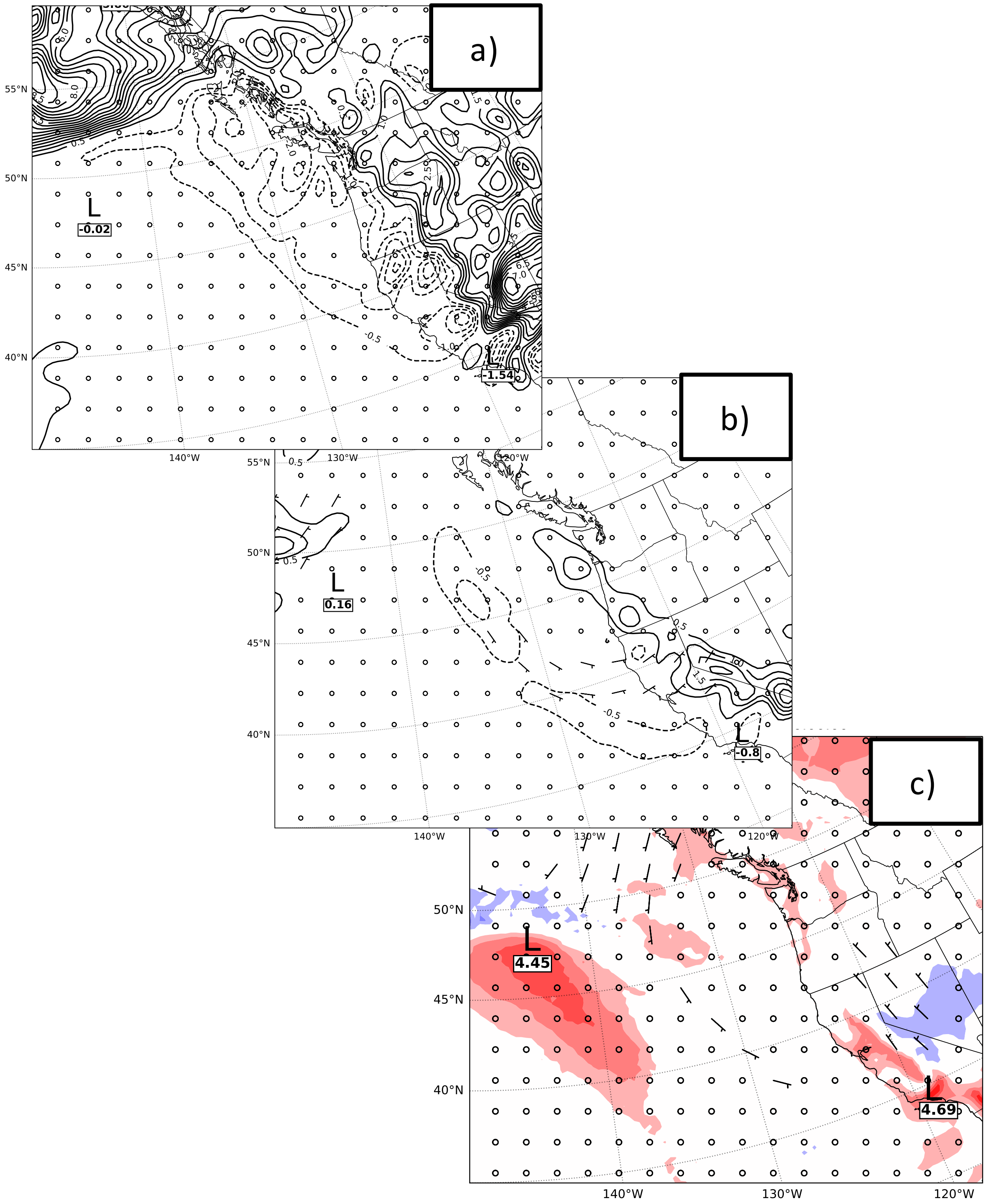

Figure 6.4. Schematic of mutual amplification as in Hoskins et al. (1985) valid at 0000 UTC 26 November 2019. (a). 300 hPa QGPVP contoured in black and scaled by $-g\frac{\partial\theta}{\partial p}\ x\ 10^6$ to convert from

units of s^{-1} to units of PVU, as in Hakim et al. (1996). Black contours are in PVU and plotted every 0.5 PVU. Geostrophic winds are derived from the inverted height anomalies associated with the QGPV anomalies in the SPERT layer and are plotted as barbs in knots. Black "L" denotes location of 950-hPa central sea-level pressure minimum and the 300 hPa QGPVP at the location of the 950-hPa central sea-level pressure minimum is plotted underneath the "L" in PVU. (b). 550 hPa QGPVP contoured in black and scaled by $-g\frac{\partial\theta}{\partial p}\ x\ 10^{6}$ to convert from units of s^{-1} to units of PVU, as in Hakim et al. (1996). Black contours are in PVU and plotted every 0.5 PVU. Geostrophic winds are derived from the inverted height anomalies associated with the QGPV anomalies in the SPERT layer and are plotted as barbs in knots. Black "L" denotes location of 950-hPa central sea-level pressure minimum and the 550 hPa QGPVP at the location of the 950-hPa central sea-level pressure minimum is plotted underneath the "L" in PVU. (c). 950 hPa geostrophic winds derived from the inverted height anomalies associated with the QGPV anomalies in the UPERT layer and plotted as barbs in knots. Boundary-level potential temperature anomaly depicted by the color fill and plotted in Kelvin. Black "L" denotes location of 950-hPa central sea-level pressure minimum and boundary-level potential temperature anomaly at the location of the 950-hPa central sea-level pressure minimum is plotted underneath the "L" in PVU.

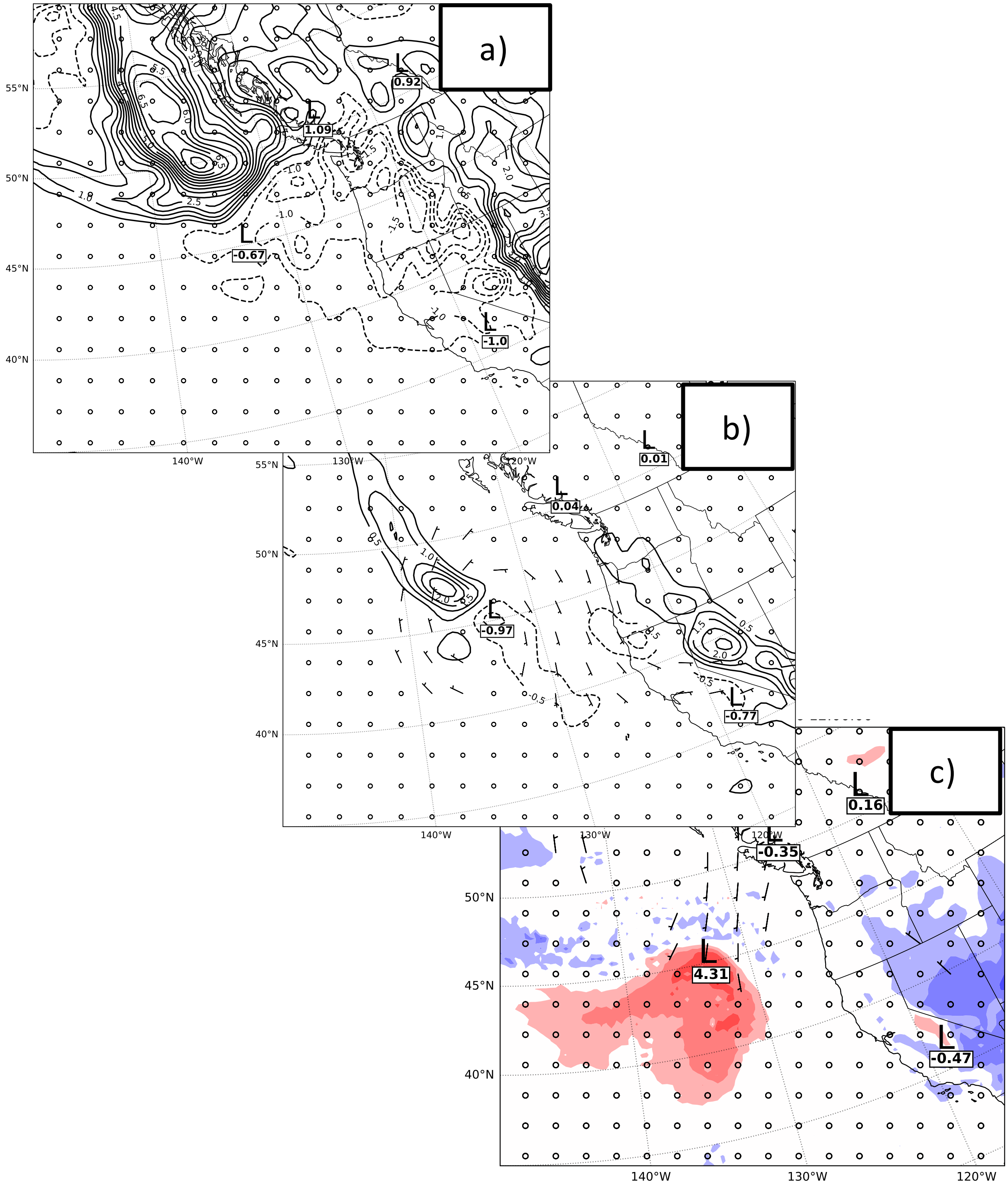

Figure 6.5. As in Fig. 6.4 but for 1200 UTC 26 November 2019.

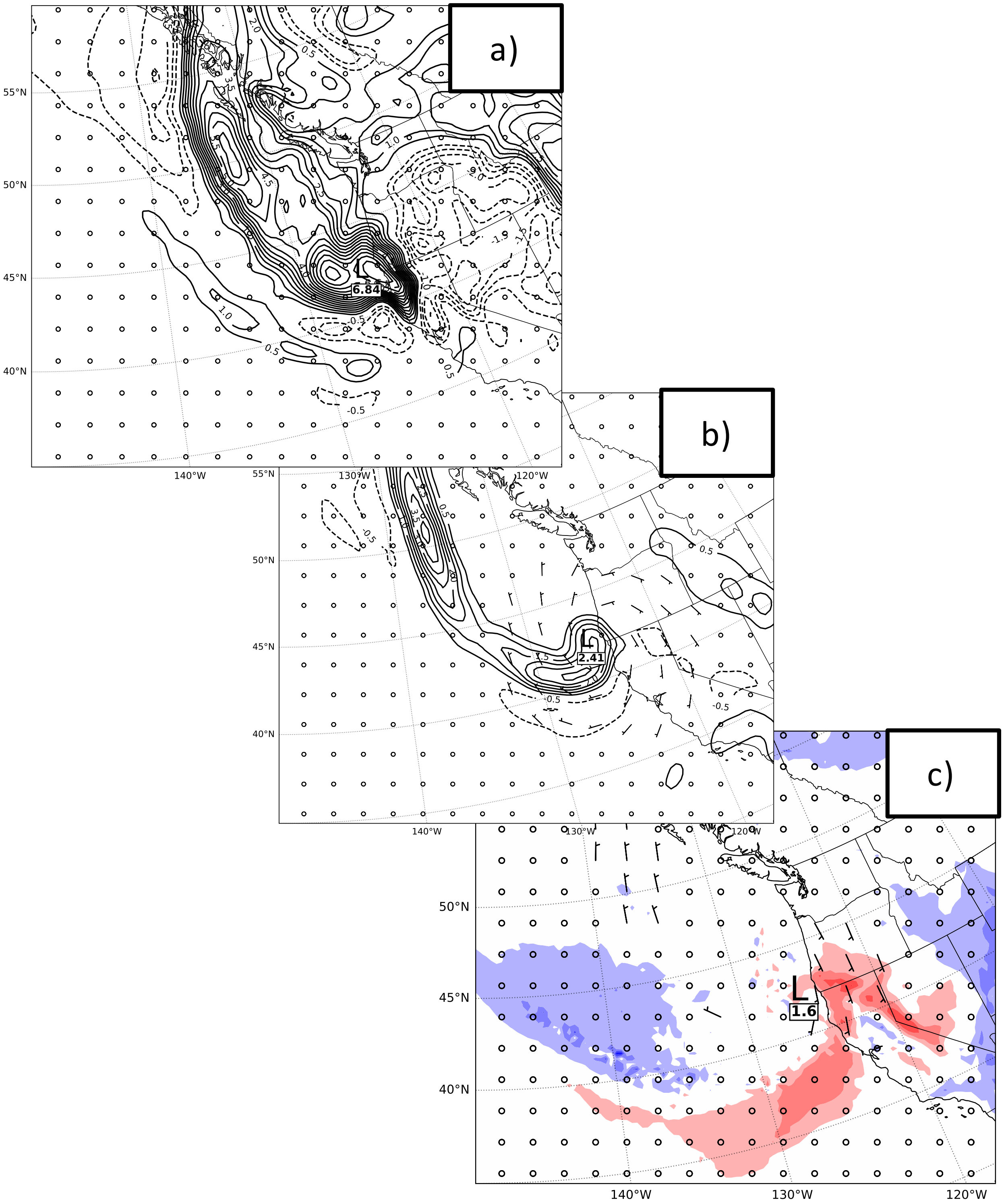

Figure 6.6. As in Fig. 6.5 but for 0000 UTC 27 November 2019.

REFERENCES

Allen, J. T., A. B. Pezza, and M. T. Black, 2010: Explosive Cyclogenesis: A Global Climatology Comparing Multiple Reanalyses. *J. Climate*, **23**, 6468-6484. https://doi.org/10.1175/2010JCLI3437.1.

Berry, G. J., & Thorncroft, C. D., 2012: African Easterly Wave Dynamics in a Mesoscale Numerical Model: The Upscale

Role of Convection. *J. Atmos. Sci.*, **69**(4), 1267-1283. https://doi.org/10.1175/JAS-D-11-099.1.

Bleck, R., 1973: Numerical Forecasting Experiments Based on the Conservation of Potential Vorticity on Isentropic Surfaces. *Journal of Applied Meteorology and Climatology*, **12**(5), 737-752. https://doi.org/10.1175/1520-0450(1973)012<0737:NFEBOT>2.0.CO;2.

Boettcher, M., & Wernli, H., 2011: Life Cycle Study of a Diabatic Rossby Wave as a Precursor to Rapid Cyclogenesis in the North Atlantic—Dynamics and Forecast Performance. *Mon. Wea. Rev.*, **139**(6), 1861-1878. https://doi.org/10.1175/2011MWR3504.1.

Bosart, L. F., 1981: The Presidents' Day Snowstorm of 18–19 February 1979: A Subsynoptic-Scale Event. *Mon. Wea. Rev.*, **109**(7), 1542-1566. https://doi.org/10.1175/15200493(1981)109<1542:TPDSOF>2.0.CO;2.

Brennan, M. J., Lackmann, G. M., & Mahoney, K. M., 2008: Potential Vorticity (PV) Thinking in Operations: The Utility

of Nonconservation. *Weather and Forecasting*, **23**(1), 168-182.

https://doi.org/10.1175/2007WAF2006044.1.

Bretherton, F. P., 1966: Critical layer instability in baroclinic flows. *Quart. J. Royal Meteor*. Soc., **92**, 325–334. https://doi.org/10.1002/qj.49709239303.

Businger, S., Graziano, T., Kaplan, M., and Rozumalski, R.A., 2005: Cold-air cyclogenesis along the Gulf-Stream front: investigation of diabatic impacts on cyclone development, frontal structure, and track. *Meteorol. Atmos. Phys*. **88**, 65–90. https://doi.org/10.1007/s00703-003-0050-y.

Carré, B. A., 1961: The Determination of the Optimum Accelerating Factor for Successive Over-relaxation, *The Computer Journal*, Volume 4, Issue 1, Pages 73–78, https://doi.org/10.1093/comjnl/4.1.73.

Charney, J., and M. E. Stern, 1962: On the stability of internal baroclinic jets in a rotating atmosphere. *J. Atmos. Sci.,* **19**, 159–172. https://doi.org/10.1175/1520-0469(1962)019<0159:OTSOIB>2.0.CO;2.

Chen, F., and J. Dudhia, 2001: Coupling an advanced land-surface/ hydrology model with the Penn State/ NCAR MM5 modeling system. Part I: Model description and implementation. *Mon. Wea. Rev.*, **129**, 569–585. https://doi.org/10.1175/1520-0493(2001)129<0569:CAALSH>2.0.CO;2.

Davis, C. A., and K. A. Emanuel, 1988: Observational evidence for the influence of surface heat fluxes on rapid maritime cyclogenesis. *Mon. Wea. Rev.*, **116**, 2649–2659. https://doi.org/10.1175/1520-0493(1988)116<2649:OEFTIO>2.0.CO;2.

————, 1991: Potential Vorticity Diagnostics of Cyclogenesis. *Mon. Wea. Rev.*, **119**(8), 1929-1953. https://doi.org/10.1175/1520-0493(1991)119<1929:PVDOC>2.0.CO;2.

Davis, C. A., 1992a: Piecewise potential vorticity inversion. *J. Atmos. Sci*., **49**, 1397–1411. https://doi.org/10.1175/1520-0469(1992)049<1397:PPVI>2.0.CO;2.

————, 1992b: A potential vorticity diagnosis of the importance of initial structure and condensational heating in observed cyclogenesis. *Mon. Wea. Rev.,* **120**, 2409–2428. https://doi.org/10.1175/1520-0493(1992)120<2409:APVDOT>2.0.CO;2.

Duginski, P., 2019: A Record 75-Foot Wave off California Coast Was Produced by Big Storm. *Los Angeles Times*. www.latimes.com/california/story/2019-12-05/thanksgiving-week-storm-record-75-foot-wave-off-california-coast.

Ekman, V. W., 1905: On the influence of the earth's rotation on ocean-currents.

Eliassen, A., 1984: Geostrophy. *Q.J.R. Meteorol. Soc*., **110**: 1-12. https://doi.org/10.1002/qj.49711046302.

————, and E. Kleinschmidt, 1957: Dynamic meteorology, in *Handbuch der Physik*, **48**, 112-129.

Springer-Verlag, Berlin.

Elsberry, R. L., & Kirchoffer, P. J., 1988: Upper-level Forcing of Explosive Cyclogenesis Over the Ocean Based on Operationally Analyzed Fields. *Weather and Forecasting*, **3**(3), 205-216. https://doi.org/10.1175/1520-0434(1988)003<0205:ULFOEC>2.0.CO;2.

Engeli, M., Ginsburg, T., Rutishauser, H., Stiefel, E., & Stiefel, E., 1959: Refined iterative methods for computation of the solution and the eigenvalues of self-adjoint boundary value problems. *Basel: Birkhäuser*.

Gyakum, J. R., 1983a: On the Evolution of the QE II Storm. I: Synoptic Aspects. *Mon. Wea. Rev.*, **111**(6), 1137-1155. https://doi.org/10.1175/1520-0493(1983)111<1137:OTEOTI>2.0.CO;2.

————, 1983b: On the evolution of the QE II storm. Part II: Dynamic and thermodynamic structure. *Mon. Wea. Rev*., **111**, 1156–1173. https://doi.org/10.1175/1520-0493(1983)111<1156:OTEOTI>2.0.CO;2.

————, & Danielson, R. E., 2000: Analysis of Meteorological Precursors to Ordinary and Explosive Cyclogenesis in the Western North Pacific. *Mon. Wea. Rev*., **128**(3), 851-863. https://doi.org/10.1175/1520-0493(2000)128<0851:AOMPTO>2.0.CO;2.

Hakim, G. J., D. Keyser, and L. F. Bosart, 1996: Diagnosis of tropopause-based coherent structures. *Preprints, Seventh Conf. on Mesoscale Processes*, Reading, United Kingdom, Amer. Meteor. Soc., 17–22.

Heo, Ki-Young, Ha, Kyung-Ja, and Ha, Taemin, 2019: Explosive Cyclogenesis around the Korean Peninsula in May 2016 from a Potential Vorticity Perspective: Case Study and Numerical Simulations. *Atmosphere*, **10**(6), 322. https://doi.org/10.3390/atmos10060322.

Hoskins, B.J., McIntyre, M.E., and Robertson, A.W., 1985: On the use and significance of isentropic potential vorticity maps. *Q.J.R. Meteorol. Soc*., **111**, 877-946. https://doi.org/10.1002/qj.49711147002.

Hultquist, T. R., Dutter, M. R., and Schwab, D. J., 2006: Reexamination of the 9–10 November 1975

"Edmund Fitzgerald" Storm Using Today's Technology. *Bulletin of the American Meteorological Society,* **87**(5), 607-622. https://doi.org/10.1175/BAMS-87-5-607.

Iacono, M. J., J. S. Delamere, E. J. Mlawer, M. W. Shephard, S. A. Clough, and W. D. Collins, 2008: Radiative forcing by long-lived greenhouse gases: Calculations with the AER radiative transfer models. *J. Geophys. Res*., **113**, D13103. https://doi.org/10.1029/2008JD009944.

Iizuka, S., M. Shiota, R. Kawamura, and H. Hatsushika, 2013: Influence of the monsoon variability and sea surface temperature front on the explosive cyclone activity in the vicinity of Japan during northern winter. *SOLA*, **9**, 1–4, http://doi.org/10.2151/sola.2013-001.

Iwao, K., Inatsu, M., & Kimoto, M., 2012: Recent Changes in Explosively Developing Extratropical Cyclones over the Winter Northwestern Pacific. *J. Climate*, **25**(20), 7282-7296. https://doi.org/10.1175/JCLI-D-11-00373.1.

Janjic, Z. I., 1994: The step-mountain eta coordinate model: further developments of the convection, viscous sublayer and turbulence closure schemes. *Mon. Wea. Rev*., **122**, 927–945. https://doi.org/10.1175/1520-0493(1994)122<0927:TSMECM>2.0.CO;2.

Kleinschmidt, E., 1950a: Über Aufbau und Entstehung von Zyklonen (1. Teil). *Met. Runds.*, **3**, 1-6.

————, 1950b: Über Aufbau und Entstehung von Zyklonen (2. Teil). *Met. Runds.*, **3**, 54-61.

————, 1951: Über Aufbau und Entstehung von Zyklonen (3. Teil). *Met. Runds.*, **4**, 89-96.

————, 1955: Die Enstehung einer Höhenzyklone über Nordamerika, *Tellus.*, **7**, 96-110.

Kluyver, T., Ragan-Kelley, B., Fernando Pérez, Granger, B., Bussonnier, M., Frederic, J., … Willing, C., 2016: Jupyter Notebooks – a publishing format for reproducible computational workflows. In F. Loizides & B. Schmidt (Eds.), *Positioning and Power in Academic Publishing: Players, Agents and Agendas* (pp. 87–90).

Korner, S. O., & Martin, J. E., 2000: Piecewise Frontogenesis from a Potential Vorticity Perspective: Methodology and a Case Study. *Mon. Wea. Rev*., **128**(5), 1266-1288. https://doi.org/10.1175/1520-0493(2000)128<1266:PFFAPV>2.0.CO;2.

Kuo, Y., & Reed, R. J., 1988: Numerical Simulation of an Explosively Deepening Cyclone in the

Eastern Pacific. *Mon. Wea. Rev.*, **116**(10), 2081-2105. https://doi.org/10.1175/1520-0493(1988)116<2081:NSOAED>2.0.CO;2.

————, R. J. Reed, and S. Low-Nam, 1991a: Effects of surface energy fluxes during the early development and rapid intensification stages of seven explosive cyclones in the western Atlantic. *Mon. Wea. Rev.*, **119**, 457–476. https://doi.org/10.1175/1520-0493(1991)119<0457:EOSEFD>2.0.CO;2.

————, M. A. Shapiro, and E. G. Donall, 1991b: The interaction between baroclinic and diabatic processes in a numerical simulation of a rapidly intensifying extratropical marine cyclone. *Mon. Wea. Rev.*, **119**, 368–384. https://doi.org/10.1175/1520-0493(1991)119<0368:TIBBAD>2.0.CO;2.

Kuwano-Yoshida, A., and Y. Asuma, 2008: Numerical study of explosively developing extratropical cyclones in the Northwestern Pacific region. *Mon. Wea. Rev.*, **136**, 712–740. https://doi.org/10.1175/2007MWR2111.1.

————, & Enomoto, T., 2013: Predictability of Explosive Cyclogenesis over the Northwestern Pacific Region Using Ensemble Reanalysis. *Mon. Wea. Rev.*, **141**(11), 3769-3785. https://doi.org/10.1175/MWR-D-12-00161.1.

Ladwig, W., 2017: wrf-python (Version 1.3.2) [Software]. Boulder, Colorado: UCAR/NCAR. https://doi.org/10.5065/D6W094P1.

Lagouvardos, K., Kotroni, V. and Defer, E., 2007: The 21–22 January 2004 explosive cyclogenesis over the Aegean Sea: Observations and model analysis. *Q.J.R. Meteorol. Soc.*, **133**: 1519-1531. https://doi.org/10.1002/qj.121.

Lang, A.A. and Martin, J.E., 2012: The structure and evolution of lower stratospheric frontal zones. Part 1: Examples in northwesterly and southwesterly flow. *Q.J.R. Meteorol. Soc.,* **138**: 1350-1365. https://doi.org/10.1002/qj.843.

Lim, E. P., and I. Simmonds, 2002: Explosive cyclone development in the Southern Hemisphere and a comparison with Northern Hemisphere events. *Mon. Wea. Rev.*, **130**, 2188–2209. https://doi.org/10.1175/2010JCLI3437.1.

Lynott, R. E., & Cramer, O. P., 1966: Detailed Analysis of the 1962 Columbus Day Windstorm in Oregon and Washington. *Mon. Wea. Rev*., **94**(2), 105-117. https://doi.org/10.1175/1520-0493(1966)094<0105:DAOTCD>2.3.CO;2.

Manobianco, J., 1989: Explosive East Coast Cyclogenesis: Numerical Experimentation and Model-Based Diagnostics. *Mon. Wea. Rev.*, **117**(11), 2384-2405. https://doi.org/10.1175/15200493(1989)117<2384:EECCNE>2.0.CO;2.

Martin, J. E., & Marsili, N., 2002: Surface Cyclolysis in the North Pacific Ocean. Part II: Piecewise Potential Vorticity Diagnosis of a Rapid Cyclolysis Event. *Mon. Wea. Rev*., **130**(5), 1264-1281. https://doi.org/10.1175/1520-0493(2002)130<1264:SCITNP>2.0.CO;2.

Martin, J. E., 2014: Quasi-geostrophic diagnosis of the influence of vorticity advection on the development of upper level jet-front systems. *Q.J.R. Meteorol. Soc*., **140**: 2658-2671. https://doi.org/10.1002/qj.2333.

Minzner, R. A., 1977: The 1976 standard atmosphere and its relationship to earlier standards. *Reviews of geophysics*, **15**(3), 375-384. https://doi.org/10.1029/RG015i003p00375.

Monin, A.S. and A.M. Obukhov, 1954: Basic laws of turbulent mixing in the surface layer of the atmosphere. *Contrib. Geophys. Inst. Acad. Sci*., USSR, (**151**), 163–187 (in Russian).

Morgan, M. C., & Nielsen-Gammon, J. W., 1998: Using Tropopause Maps to Diagnose Midlatitude Weather Systems. *Mon. Wea. Rev*., **126**(10), 2555-2579. https://doi.org/10.1175/1520-0493(1998)126<2555:UTMTDM>2.0.CO;2.

Morgan, M. C., 1999: Using Piecewise Potential Vorticity Inversion to Diagnose Frontogenesis. Part I: A Partitioning of the Q Vector Applied to Diagnosing Surface Frontogenesis and Vertical Motion. *Mon. Wea. Rev*., **127**(12), 2796-2821. https://doi.org/10.1175/1520-0493(1999)127<2796:UPPVIT>2.0.CO;2.

Mullen, S. L., & Baumhefner, D. P., 1988: Sensitivity of Numerical Simulations of Explosive Oceanic

Cyclogenesis to Changes in Physical Parameterizations. *Mon. Wea. Rev*., **116** (11), 2289-2329. https://doi.org/10.1175/1520-0493(1988)116<2289:SONSOE>2.0.CO;2.

Odell, L., Knippertz, P., Pickering, S., Parkes, B. and Roberts, A., 2013: The *Braer* storm revisited. *Weather*, **68**: 105-111. https://doi.org/10.1002/wea.2097.

Pang, H., & Fu, G., 2017: Case Study of Potential Vorticity Tower in Three Explosive Cyclones over Eastern Asia. *Journal of the Atmospheric Sciences*, **74**(5), 1445-1454. https://doi.org/10.1175/JAS-D-15-0330.1.

Petterssen, S., & Smebye, S. J., 1971: On the development of extratropical cyclones. *Quarterly Journal of the Royal Meteorological Society*, **97**(414), 457-482. https://doi.org/10.1002/qj.49709741407.

Plant, R.S., Craig, G.C. and Gray, S.L., 2003: On a threefold classification of extratropical cyclogenesis. *Q.J.R. Meteorol.*

Soc., **129**: 2989-3012. https://doi.org/10.1256/qj.02.174.

Reed, R. J., & Albright, M. D., 1986: A Case Study of Explosive Cyclogenesis in the Eastern Pacific. *Mon. Wea. Rev*., **114**(12), 2297-2319. https://doi.org/10.1175/1520-0493(1986)114<2297:ACSOEC>2.0.CO;2.

————, Sammons, A. J., & Undén, P., 1988: The Role of Latent Heat Release in

Explosive Cyclogenesis: Three Examples Based on ECMWF Operational Forecasts. *Weather and Forecasting*, **3**(3), 217-229. https://doi.org/10.1175/1520-0434(1988)003<0217:TROLHR>2.0.CO;2.

————, M. T., & Kuo, Y., 1992: A Model-aided Study of the Origin and Evolution of the Anomalously High Potential

vorticity in the Inner Region of a Rapidly Deepening Marine Cyclone. *Mon. Wea. Rev.*, **120**(6), 893-913. https://doi.org/10.1175/1520-0493(1992)120<0893:AMASOT>2.0.CO;2.

Revell, M. J., & Gorman, R. M., 2003: The “Wahine storm”: Evaluation of a numerical forecast of a severe wind and wave event for the New Zealand coast. *New Zealand Journal of Marine and Freshwater Research*, **37**:2, 251-266. https://doi.org/10.1080/00288330.2003.9517163.

Rew, R. and G. Davis, 1990: NetCDF: an interface for scientific data access. *IEEE Computer Graphics and Applications*, vol. 10, no. 4, pp. 76-82. https://doi.org/10.1109/38.56302.

Roebber, P. J., 1984: Statistical analysis and updated climatology of explosive cyclones. *Mon. Wea. Rev.*, **112**, 1577-1589. https://doi.org/10.1175/1520-0493(1984)112<1577:SAAUCO>2.0.CO;2.

————, 1989: The Role of Surface Heat and Moisture Fluxes Associated with Large-Scale Ocean Current Meanders in Maritime Cyclogenesis. *Mon. Wea. Rev.*, **117**(8), 1676-1694. https://doi.org/10.1175/1520-0493(1989)117<1676:TROSHA>2.0.CO;2.

————, 1993: A Diagnostic Case Study of Self-Development as an Antecedent Conditioning Process in Explosive Cyclogenesis. *Mon. Wea. Rev.*, **121**(4), 976-1006. https://doi.org/10.1175/1520-0493(1993)121<0976:ADCSOS>2.0.CO;2.

Rossby C. G., 1939: Relation between variations in the intensity of the zonal circulation of the atmosphere and the displacements of the semi-permanent centers of action. *J. Mar. Res*., **2**(1), 38-55.

————, 1940: Planetary flow patterns in the atmosphere. *Quart. J. Roy. Met. Soc*., **66**, 68-87.

Rotunno, R., Skamarock, W. C., & Snyder, C., 1994: An analysis of frontogenesis in numerical simulations of baroclinic waves. *J. Atmos. Sci*., **51**(23), 3373-3398. https://doi.org/10.1175/1520-0469(1994)051<3373:AAOFIN>2.0.CO;2.

Sanders. F., and J. R. Gyakum, 1980: Synoptic-dynamic climatology of the 'bomb.' *Mon. Wea. Rev.*, **108**, 1589–1606. https://doi.org/10.1175/1520-0493(1980)108<1589:SDCOT>2.0.CO;2.

————, 1986a: Explosive cyclogenesis in the west-central North Atlantic Ocean, 1981–84. Part I: Composite structure and mean behavior. *Mon. Wea. Rev.*, **114**, 1781–1794. https://doi.org/10.1175/1520-0493(1986)114<1781:ECITWC>2.0.CO;2.

Skamarock, W. C., Klemp, J. B., Dudhia, J., Gill, D. O., Barker, D., Duda, M. G., … Powers, J. G., 2008: *A Description of the Advanced Research WRF Version 3* (No. NCAR/TN-475+STR). University Corporation for Atmospheric Research. http://dx.doi.org/10.5065/D68S4MVH.

————, Liu, Z., Berner, J., … Huang, X. -yu., 2019: A Description of the Advanced Research WRF Model Version 4 (No. NCAR/TN-556+STR). http://dx.doi.org/10.5065/1dfh-6p97.

Stoelinga, M. T., 1996: A Potential Vorticity-Based Study of the Role of Diabatic Heating and Friction in a Numerically Simulated Baroclinic Cyclone. *Mon. Wea. Rev.*, **124**(5), 849-874. https://doi.org/10.1175/1520-0493(1996)124<0849:APVBSO>2.0.CO;2.

Sutcliffe, R. C., 1939: Cyclonic and anticyclonic development. *Q.J.R. Meteorol. Soc.*, **65**(282), 518-524. https://doi.org/10.1002/qj.49706528208.

———— , 1947: A contribution to the problem of development. *Q.J.R. Meteorol. Soc.*, **73**(317-318), 370-383.

https://doi.org/10.1002/qj.49707331710.

———— and Forsdyke, A.G., 1950: The theory and use of upper air thickness patterns in forecasting. *Q.J.R. Meteorol. Soc.*, **76**: 189-217. https://doi.org/10.1002/qj.49707632809.

Tiedtke, M., 1989: A comprehensive mass flux scheme for cumulus parameterization in largescale models. *Mon. Wea. Rev.*, **117**, 17791800. https://doi.org/10.1175/1520-0493(1989)117<1779:ACMFSF>2.0.CO;2.

Thompson, G., P. R. Field, R. M. Rasmussen, and W. D. Hall, 2008: Explicit Forecasts of Winter Precipitation Using an Improved Bulk Microphysics Scheme. Part II: Implementation of a New Snow Parameterization. *Mon. Wea. Rev.*, **136**, 5095–5115. https://doi.org/10.1175/2008MWR2387.1.

Uccellini, L. W., D. Keyser, K. F. Brill, and C. H. Wash, 1985: The Presidents' Day cyclone of 18–19 February 1979: Influence of upstream trough amplification and associated tropopause folding on rapid cyclogenesis. *Mon. Wea. Rev.*, **113**, 962–988. https://doi.org/10.1175/1520-0493(1985)113<0962:TPDCOF>2.0.CO;2.

Wang, C., & Rogers, J. C., 2001: A Composite Study of Explosive Cyclogenesis in Different Sectors of the North Atlantic. Part I: Cyclone Structure and Evolution. *Mon. Wea. Rev.*, **129**(6), 1481-1499. https://doi.org/10.1175/1520-0493(2001)129<1481:ACSOEC>2.0.CO;2.

Wash, C. H., R. A. Hale, P. H. Dobos, and E. J. Wright, 1992: Study of explosive and nonexplosive cyclogenesis during FGGE. *Mon. Wea. Rev.*,**120**, 40–51. https://doi.org/10.1175/15200493(1992)120<0040:SOEANC>2.0.CO;2.

Yoshiike, S., and R. Kawamura, 2009: Influence of wintertime large-scale circulation on the explosively developing cyclones over the western North Pacific and their downstream effects. *J. Geophys. Res*., **114**, D13110, https://doi.org/10.1029/2009JD011820.

Zhang, S., G. Fu, C. Lu, and J. Liu, 2017: Characteristics of Explosive Cyclones over the Northern Pacific. *J. Appl. Meteor. Climatol.*, **56**, 3187–3210, https://doi.org/10.1175/JAMC-D-16-0330.1.